

*Nanoscale light-matter interactions  
in van der Waals materials*

Tom Vincent

Department of Physics  
Royal Holloway, University of London  
A thesis for the degree of Doctor of Philosophy

August 2022





## *Declaration of authorship*

I, Tom Vincent, hereby declare that this thesis and the work presented in it is entirely my own. Where I have consulted the work of others, this is always clearly stated.

Signed: TCW Vincent

Date: 16 August 2022



# *Abstract*

In this thesis, I study nanoscale light-matter interactions in two-dimensional (2d) and van der Waals (vdW) materials, with a particular focus on graphene and graphene-based heterostructures.

In part I, I begin by reviewing some key background information, with an overview of the physics of graphene and bilayer graphene (BLG) in chapter 1, and an overview of the wider family of 2d materials and vdW heterostructures in chapter 2.

Then in part II, I follow this with a review of the characterisation techniques used in the rest of this thesis, with a discussion of laser-coupled scanning probe microscopy (SPM) methods in chapter 3, and of optical spectroscopy in chapter 4.

Finally in part III, I present several original research chapters based on work I conducted during my PhD:

Chapter 5 demonstrates spatial mapping of nanoscale strains and doping in graphene heterostructures with Raman vector decomposition analysis, in which I reveal that variations in Raman spectra correlate with nanoscale features such as cracks, bubbles and wrinkles.

In chapter 6, I build upon this by investigating bubbles in boron nitride-encapsulated graphene with scanning near-field optical microscopy (SNOM), and reveal strongly absorbing subwavelength domains for infrared light, which relate to the complex strain configurations of the bubbles.

Chapter 7 focuses on a different vdW material indium selenide, and I use Raman and photoluminescence (PL) spectroscopy to probe strains induced by depositing the material on a patterned substrate.

Lastly, in chapter 8 I showcase different ways that data cluster analysis, a machine learning tool, can accelerate the identification and analysis of twisted bilayer graphene from Raman spectra.

The research presented here demonstrates that the combination of advanced microscopy and spectroscopy with modern computational techniques, such as vector decomposition and machine learning, can reveal a wealth of important material properties. With these techniques, I show that nanoscale features of vdW materials and heterostructures, such as fractures folds and bubbles, play a significant role in determining their optoelectronic properties, particularly via their local effects on strain and doping. This is fundamentally important for both the design and characterisation of 2d material-based optoelectronic devices.



# *Acknowledgements*

I couldn't have finished this PhD without my supervisor Olga, who has always made time for me despite her hectic schedule. Throughout my time at NPL, she has helped me to turn my ideas into experiments, my experiments into results, and my results into publications. As a junior researcher, it's often hard to judge whether your work is up to scratch. So it's made a huge difference having a supervisor who publicly supports both me and my science. Thank you so much for all of your help, Olga.

My friends and colleagues are the greatest resource I've had at NPL. I count myself lucky to have worked with such a wholly fantastic group of scientists. Whenever you've "imparted your knowledge", over coffee or jars, it has been an education. And without your cleanroom wizardry, experimental genius and excellent company I'd be nowhere. To Alessandro, Alex, Andrew, Chris, Christos, Craig, Cristina, Dave, Eli, Filipe, Gökhan, Héctor, Helen, Jess, Kat, Mayela, Míriam, Mitsos, Nate, Robb, Sasha, Sayanti, Seb, Sergiy, Sophie, Toby and Vish: thanks for making the lab worth coming to.

Special thanks go to my co-supervisor Vladimir, at Royal Holloway. It's tricky to stay in the loop when your workplace isn't your university, but Vladimir's help has made everything that much easier.

I've had the opportunity to collaborate with some excellent scientists and great people from all over the world. I'd particularly like to thank Matt Hamer, Dan Terry, Jessie Boland, Nila Balakrishnan, Roman Gorbachev and Irina Grigorieva, from the University of Manchester; Hyungoo Ji and Hiroki Ago, from Kyushu University; Zakhar Kudrinskyi and Amalia Patanè, from the University of Nottingham; Stephen Power, from Trinity College Dublin; and Jing Zhao and Antti-Pekka Jauho from the Technical University of Denmark.

I'd also like to thank Guillaume Froehlicher and Stéphane Berciaud for allowing me to show some of their data in chapters 4 and 5 of this thesis.

I've lived outside of London for my whole time at NPL. The thing that's kept me from moving closer is my friends and housemates in Guildford. Kris, Nat, Ross, Duffy, Alex and Charlotte, thanks for putting up with me. You're the best.

And finally, the biggest thank you goes to my family: Eddy, Alex, Mum and Dad. I couldn't have even started this PhD without your patience and support. I love you loads.



# Contents

	<i>Introduction</i>	11
	<i>I Background</i>	13
1	<i>Electronic and optoelectronic properties of graphene</i>	15
	1.1 <i>Single-layer graphene</i>	15
	1.1.1 <i>Band structure and transport properties of graphene</i>	16
	1.1.2 <i>Strain effects in graphene</i>	18
	1.1.3 <i>Light-matter interaction in graphene</i>	20
	1.1.4 <i>Graphene plasmonics</i>	22
	1.2 <i>Bilayer graphene</i>	25
	1.2.1 <i>Band structure of bilayer graphene</i>	25
	1.2.2 <i>Twisted bilayer graphene</i>	26
	1.3 <i>Conclusions</i>	28
2	<i>Van der Waals materials and heterostructures</i>	29
	2.1 <i>Van der Waals materials beyond graphene</i>	29
	2.1.1 <i>Hexagonal boron nitride</i>	29
	2.1.2 <i>Transition metal dichalcogenides</i>	31
	2.1.3 <i>Post-transition metal chalcogenides</i>	32
	2.1.4 <i>Other 2d and van der Waals materials</i>	33
	2.1.5 <i>Fabricating 2d materials</i>	33
	2.2 <i>Van der Waals heterostructures</i>	34
	2.2.1 <i>Hexagonal boron nitride encapsulation</i>	35
	2.2.2 <i>Bubble formation and self cleaning</i>	36
	2.2.3 <i>Fabricating van der Waals heterostructures</i>	37
	2.3 <i>Conclusions</i>	38

	<i>II</i>	<i>Characterising van der Waals materials</i>	39
3		<i>Laser-coupled scanning probe microscopy techniques</i>	41
	3.1	<i>Basics of atomic force microscopy</i>	41
	3.1.1	<i>Lock-in amplifiers</i>	43
	3.2	<i>Scanning near-field optical microscopy</i>	43
	3.2.1	<i>Near-field interaction principle</i>	44
	3.2.2	<i>Distinguishing near-field and far-field light</i>	45
	3.2.3	<i>Phase sensitive detection</i>	47
	3.3	<i>AFM infrared spectroscopy</i>	48
	3.4	<i>Conclusions</i>	49
4		<i>Optical spectroscopy of van der Waals materials</i>	51
	4.1	<i>Light matter interaction for optical spectroscopy</i>	51
	4.1.1	<i>Raman scattering</i>	51
	4.1.2	<i>Photoluminescence</i>	52
	4.2	<i>Optical spectroscopy in practice</i>	53
	4.3	<i>The Raman spectrum of graphene</i>	54
	4.3.1	<i>Graphene phonon dispersion</i>	54
	4.3.2	<i>Origin of the graphene Raman peaks</i>	55
	4.4	<i>Characterising graphene with Raman spectroscopy</i>	56
	4.4.1	<i>Number of layers</i>	56
	4.4.2	<i>Strain</i>	57
	4.4.3	<i>Doping</i>	58
	4.5	<i>Conclusions</i>	58
	<i>III</i>	<i>Original research</i>	59
5		<i>Imaging of graphene's strain and doping with Raman vector analysis</i>	61
	5.1	<i>Distinguishing strain and doping with Raman vector decomposition analysis</i>	61
	5.1.1	<i>Important considerations for strain-doping decomposition</i>	63
	5.2	<i>Identifying nanoscale structural features in graphene-hBN heterostructures</i>	65
	5.2.1	<i>Heterostructure A: exposed and hBN-capped graphene</i>	65
	5.2.2	<i>Heterostructure B: encapsulated graphene with bubbles</i>	68
	5.3	<i>Conclusions</i>	73

6	<i>Subwavelength infrared domains in graphene bubbles</i>	75
6.1	<i>Network of bubbles in encapsulated graphene</i>	77
6.2	<i>Nanoscale infrared domains within bubbles</i>	78
6.3	<i>Spectroscopic characteristics of the bubbles</i>	79
6.3.1	<i>Wavelength dependence of the domains across the mid-IR</i>	81
6.3.2	<i>Probing the chemical contents of bubbles with AFM-IR</i>	82
6.4	<i>Colocalised strain and doping mapping</i>	83
6.5	<i>Origin of the nanoscale domains</i>	86
6.6	<i>Conclusions</i>	89
7	<i>Probing strains in indium selenide with optical spectroscopy</i>	91
7.1	<i>The Raman spectrum of indium selenide</i>	92
7.2	<i>Sample A: indium selenide on pillars</i>	93
7.2.1	<i>Raman characterisation</i>	93
7.2.2	<i>Photoluminescence characterisation</i>	94
7.3	<i>Sample B: indium selenide on holes</i>	96
7.3.1	<i>Raman characterisation</i>	96
7.3.2	<i>Photoluminescence characterisation</i>	98
7.3.3	<i>Probing light-induced oxidation of indium selenide</i>	99
7.4	<i>Conclusions</i>	100
8	<i>Data cluster analysis of twisted bilayer graphene</i>	103
8.1	<i>Sample characteristics</i>	105
8.2	<i>Raman analysis</i>	106
8.2.1	<i>Region A</i>	106
8.2.2	<i>Region B</i>	108
8.3	<i>Mahalanobis normalisation</i>	108
8.4	<i>Gaussian mixture model</i>	109
8.5	<i>Classifying new data using a pretrained model</i>	111
8.6	<i>Application to full spectra</i>	113
8.7	<i>Conclusions</i>	116

<i>Conclusions and outlook</i>	119
<i>Dissemination</i>	121
<i>Publications</i>	121
<i>Presentations</i>	122
<i>Oral</i>	122
<i>Posters</i>	123
<i>Reference</i>	125
<i>List of abbreviations</i>	125
<i>List of symbols</i>	127
<i>List of figures</i>	131
<i>Appendices</i>	135
<i>Optical unit conversion charts</i>	135
<i>Supplementary data clustering figures</i>	137
<i>Bibliography</i>	139

# *Introduction*

The discovery of the two-dimensional (2d) material family promised to revolutionise nanotechnology. The excitement was kick-started when single layers of carbon atoms were first separated from graphite to form graphene [1]. In the following years, many other 2d materials were separated from their parent van der Waals (vdW) material and shown to be stable under ambient conditions.

These materials boast some outstanding properties. They are remarkably strong and flexible, so they are able to withstand significant in-plane stretching and out-of-plane bending without damage. Their atomic thinness results in an extremely high surface-area-to-volume ratio, which makes them very sensitive to their environment. And across the whole family, there is a wide range of individual material properties suited to many applications [2].

The potential for 2d material applications was boosted further with the rise of a new approach to fabrication. Individual 2d materials can be stacked on top of one another, like the layers of carbon in graphite, and will stick together due to vdW forces. The resultant stacks are called van der Waals heterostructures, and they allow different material properties to be combined in single devices [3].

This method of construction comes with huge benefits: 2d materials are atomically flat, which means they form almost ideal substrates for one another [4]; the vdW force that holds the layers together also squeezes away any trapped contamination, meaning vdW heterostructures spontaneously clean themselves [5]; and interaction between the layers means that they often have entirely new properties, which didn't exist in any of the constituent layers [6]. Thanks to these advantages and others, the introduction of vdW heterostructures helped to make predictions about the superior electronic properties of 2d materials a reality.

This year will mark the 18<sup>th</sup> anniversary of graphene's discovery and, accordingly, the field of 2d materials is approaching adulthood.

Graphene devices are now readily available, and can be acquired from commercial foundries instead of made one-by-one in a research lab. This enables research into applications to progress at a faster rate than ever. For instance, within the first few months of the Covid-19 pandemic in 2020, scientists had already demonstrated working prototypes of graphene-based coronavirus sensors [7]. Research into graphene plasmonics has led to devices that squeeze light into tiny spaces, and manipulate it electronically [8] These may become a new

frontier for computing technology once we reach the intrinsic density and speed limits of silicon.

And despite the maturity of the field there is still much more to discover about graphene and vdW materials. Indeed, it was only relatively recently that twisted bilayer graphene was unexpectedly revealed to be a superconductor [9], triggering a whole new wave of interest in the material.

As the focus of researchers gradually shifts from graphene to the wider family of 2d materials [2], we should expect that there will be many more groundbreaking discoveries in the coming years.

In this thesis, I study nanoscale light-matter interactions in vdW materials. It's important to understand how these materials respond to light for two main reasons. The first of these is that it enables a wide range of optical characterisation techniques, which reveal key details about the properties of a material. The second is that 2d materials have tremendous potential for manipulating light in optoelectronic devices. Light-matter interactions in 2d and vdW materials are therefore of fundamental importance for successful device design and fabrication.

I particularly focus on the nanoscale features of real-world devices and heterostructures which are often neglected. I show how features like bubbles, fractures, grain boundaries and wrinkles can alter the properties of 2d materials, by changing the local strain, charge doping or electronic dispersion. These features become significant when the sizes of devices are also pushed to smaller and smaller scales, and can even be exploited to create tailored properties. But I also demonstrate that many of the bulk properties of larger devices are actually emergent properties, stemming from the collective behaviour of nanoscale features.

To study these effects, I use a range of scanning probe microscopy (SPM) and optical microscopy techniques. I also explore how modern computational tools, including vector decomposition analysis and machine learning tools like data clustering, can help us to analyse the large, high-dimensional datasets acquired by these techniques.

In the following years, I hope that the methods and findings presented in this thesis will assist the development of scalable, optoelectronic 2d-material devices, with precise control of the nanoscale material properties.

**Part I**

**Background**



# 1

## *Electronic and optoelectronic properties of graphene*

As the first two-dimensional (2d) material to be isolated, graphene has been the focus of most of the research in the field. Its superlative properties have made it one of the most exciting new materials of the millennium. But beyond its promise for groundbreaking technological applications, it's also fascinating thanks to the compelling physics which governs its behaviour.

In this chapter I review the basic physics of graphene and its bilayer. I also introduce topics explored further in the rest of this thesis: strain effects, light-matter interactions, plasmonics, and twisted bilayer graphene.

### *1.1 Single-layer graphene*

Graphene, or single layer graphene (SLG), is formed of a one-atom-thick layer of carbon arranged in a honeycomb lattice, as shown in figure 1.1.

Atomic carbon has four valence electrons. In graphene, three of these form the  $sp^2$ -hybridised in-plane bonds, known as  $\sigma$  bonds. The remaining electrons form  $2p_z$  orbitals, perpendicular to the lat-

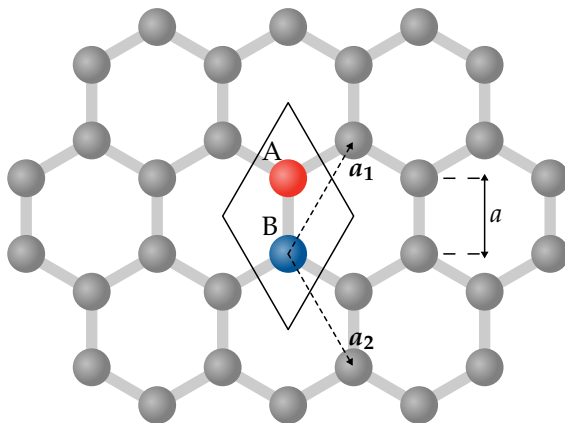


Figure 1.1: Graphene lattice structure. The diamond-shaped unit cell, and A and B lattice sites, are highlighted. The lattice vectors and carbon-carbon separation distance are shown by dashed and solid arrows respectively.

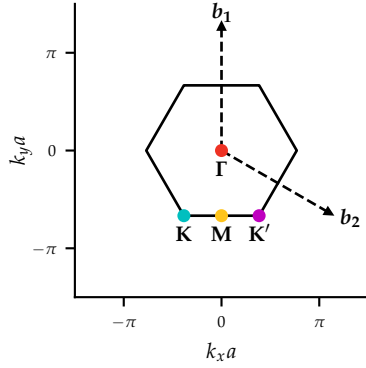


Figure 1.2: Graphene Brillouin zone. High-symmetry points are shown by circles (coloured to match figure 1.3), reciprocal lattice vectors are shown by dashed arrows.

tice. These orbitals make  $\pi$  bonds, and are responsible for most of the conduction behaviour in graphene.

The honeycomb lattice can be viewed as a triangular lattice with a basis of two atoms per unit cell, referred to as A and B. The lattice vectors can be written as

$$\mathbf{a}_1 = \frac{a}{2} \begin{pmatrix} \sqrt{3} \\ 3 \end{pmatrix}, \quad \mathbf{a}_2 = \frac{a}{2} \begin{pmatrix} \sqrt{3} \\ -3 \end{pmatrix}, \quad (1.1)$$

where  $a \approx 1.42 \text{ \AA}$  is the distance between neighbouring atoms [10]. Similarly, the reciprocal lattice vectors can be written as

$$\mathbf{b}_1 = \frac{2\pi}{3a} \begin{pmatrix} 0 \\ 2 \end{pmatrix}, \quad \mathbf{b}_2 = \frac{2\pi}{3a} \begin{pmatrix} \sqrt{3} \\ -1 \end{pmatrix}. \quad (1.2)$$

The Brillouin zone (BZ) of graphene is shown in figure 1.2. Some key high-symmetry points are labelled: the BZ centre,  $\Gamma$ ; the mid-point of the BZ edge,  $M$ ; and the two inequivalent BZ corners,  $\mathbf{K}$  and  $\mathbf{K}'$ .

The six-fold rotational symmetry of graphene means it's useful to define two terms for specific equivalent orientations in the lattice: *zigzag*, which can be represented by the horizontal direction in figure 1.1, and *armchair*, which can be represented by the vertical direction. These are named after the shapes formed by the atoms at edges oriented in each direction. Zigzag and armchair are at  $30^\circ$  to each other, and a rotation from either one by  $60^\circ$  will result in an equivalent orientation.

### 1.1.1 Band structure and transport properties of graphene

The  $\pi$ -electron band structure of graphene can be calculated using the tight-binding approach as

$$E(\mathbf{k}) = \pm \gamma_0 \sqrt{3 + f(\mathbf{k})} - \gamma'_0 f(\mathbf{k}), \quad (1.3)$$

$$f(\mathbf{k}) = 2 \cos(\sqrt{3}k_y a) + 4 \cos\left(\frac{\sqrt{3}}{2}k_y a\right) \cos\left(\frac{3}{2}k_x a\right),$$

where  $E$  is the energy of the band edges,  $\mathbf{k}$  is the wavevector, and  $\gamma_0$  and  $\gamma'_0$  are the nearest- and second-nearest-neighbour hopping energies respectively [10]. These hopping energies relate to the incentive for an electron to jump from one atom to another in the graphene lattice. The resulting band structure of graphene is shown in figure 1.3 (a).

Finite values of  $\gamma'_0$  break the electron-hole symmetry in graphene, leading to the asymmetry seen between the conduction and valence bands (shown in blue and red in figure 1.3). At low energies this can usually be neglected, and  $\gamma_0$  is sufficient to describe the electronic behaviour of graphene. I therefore neglect  $\gamma'_0$  for the rest of section 1.1.1.

The most salient features of the graphene band structure are the Dirac cones at the  $\mathbf{K}$  and  $\mathbf{K}'$  points, where the conduction and valence

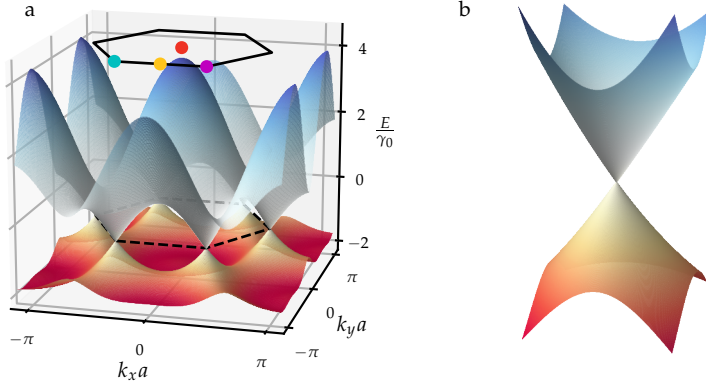


Figure 1.3: Band structure of graphene. (a) Full band structure, found from Equation 1.3 with  $\gamma'_0 = -0.2\gamma_0$ . High-symmetry points and the BZ edge are shown at the top, and coloured to match figure 1.2 (also shown with dashed lines at the Dirac point energy). (b) Zoom on a single Dirac cone at the  $\mathbf{K}$  point.

bands meet. A close-up of a single cone in figure 1.3 (b) shows that they meet at an infinitesimal point, known as the Dirac point. For this reason, graphene is termed a zero-bandgap semiconductor, or semimetal. In charge-neutral graphene the Fermi level,  $E_F$ , aligns with the Dirac point energy at  $E_F = 0$ , often referred to as the charge neutrality point (CNP).

The Dirac point carrier dispersion can be found by expanding the full band structure close to  $\mathbf{K}$  as

$$E(\mathbf{q}) = \pm \hbar v_F |\mathbf{q}| + \mathcal{O}\left(\frac{|\mathbf{q}|}{|\mathbf{K}|}\right)^2, \quad |\mathbf{q}| \ll |\mathbf{K}|, \quad (1.4)$$

where  $\mathbf{q} = \mathbf{k} - \mathbf{K}$  is the wavevector relative to the  $\mathbf{K}$  point,  $\hbar$  is the reduced Planck constant and  $v_F = 3a\gamma_0/(2\hbar)$  is the constant Fermi velocity of graphene [10]. It follows that the low-energy Fermi level in graphene can be related to the carrier density according to

$$E_F = \hbar v_F |\mathbf{k}_F| = \hbar v_F \operatorname{sgn}(n) \sqrt{\pi |n|}, \quad (1.5)$$

where  $\mathbf{k}_F$  is the Fermi wavevector, and positive and negative  $n$  correspond to electron and hole density.

The linear dependence of energy on wavevector leads to charge carriers with zero effective mass. This behaviour is markedly different to that of massive carriers in other materials, whose velocity depends on their energy, and is similar to the relativistic dispersions of massless particles such as photons.

The infinitesimal overlap of the conduction and valence bands leads to a vanishing density of states (DOS) at the Dirac point energy. Close to the Dirac point, the DOS per unit cell can be approximated as

$$\rho(E) = \frac{3\sqrt{3}a^2}{\pi v_F^2} |E|. \quad (1.6)$$

This leads to a resistance maximum for charge-neutral graphene [10].

The carrier density and Fermi level in graphene can be effectively controlled via the field effect [1]. This is usually achieved by placing the graphene on a thin dielectric spacer, then applying a bias between the graphene and a conducting material on the other side, in a process known as gating.

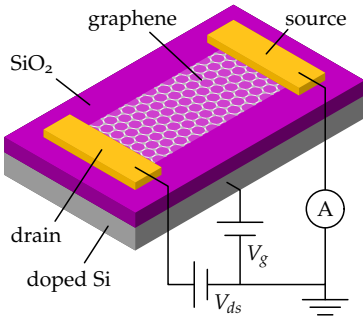


Figure 1.4: Simple graphene FET example.

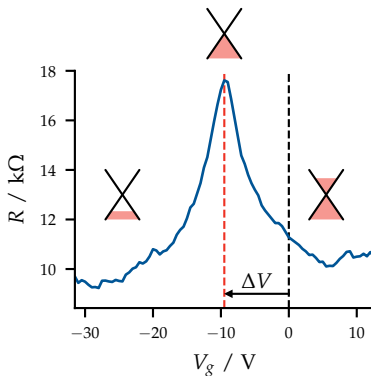


Figure 1.5: Example of an experimental transfer curve from a graphene FET. Dirac cone diagrams schematically show the filling of states in each regime. Dashed lines and arrow show the  $V_g$  offset needed to reach the CNP.

Figure 1.4 shows an example of a typical graphene field effect transistor (FET) on an oxidised Si wafer, with a graphene channel between source and drain electrical contacts, and a gate formed by the doped Si back of the wafer and thin oxide layer as dielectric. The Fermi level, and thus the resistance, of the channel can be altered by applying a gate voltage. In practice, there are many varying designs for graphene FETs, which often employ different dielectrics and combinations of top and bottom gates.

Figure 1.5 shows a transfer curve from a real graphene FET, with a clear resistance peak at the CNP. In this device, the CNP is not aligned with  $V_g = 0\text{V}$  due to an intrinsic charge imbalance in the graphene channel. This offset,  $\Delta V$ , is usually due to charge doping from materials in contact with the graphene, such as atmospheric gases or surface adsorbants [11]. Figure 1.5 shows that even for such devices, gating can be used to bring the graphene to the Dirac point.

If the thickness,  $d$ , and dielectric constant,  $\epsilon$ , of the spacer are known, the applied  $V_g$  can be converted directly to  $E_F$  by modelling the FET as a plate capacitor as

$$V_g - \Delta V = \frac{E_F}{e_q} + \frac{ne_q}{C_g}, \quad (1.7)$$

$$C_g = \frac{\epsilon_0 \epsilon}{d},$$

where  $e_q$  is the electron charge,  $C_g$  is the geometrical capacitance and  $\epsilon_0$  is the vacuum permittivity [12]. This equation is generally valid for any capacitor with a low DOS in one plate. The first term arises from quantum capacitance and is often negligible compared to the second. The second term arises from the classical gate capacitance and depends on carrier density,  $n$ , which is itself dependent on  $E_F$ . For SLG,  $n$  can be converted to  $E_F$  using equation 1.5.

### 1.1.2 Strain effects in graphene

Graphene's  $\sigma$  bonds give it remarkable in-plane strength, meaning it can withstand significant strains without damage. This, in combination with its superior flexibility, which arises from its atomic thinness, means its electronic and optoelectronic properties are especially susceptible to modification by strain. In recent years, this has led to a new field of engineering, which aims to create tailored devices in 2d materials by applying strain, and is referred to by some as straintronics [13].

In two dimensions, strains can be represented by the biaxial strain tensor, defined as

$$\epsilon_{bi} = \begin{pmatrix} \epsilon_{xx} & \epsilon_{xy} \\ \epsilon_{yx} & \epsilon_{yy} \end{pmatrix} \quad (\text{where } \epsilon_{xy} = \epsilon_{yx}), \quad (1.8)$$

whose components describe a linear vector transformation which locally maps the unstrained lattice to the strained lattice. This can vary spatially and is able to describe the full range of uniaxial, biaxial and mixed strain configurations.

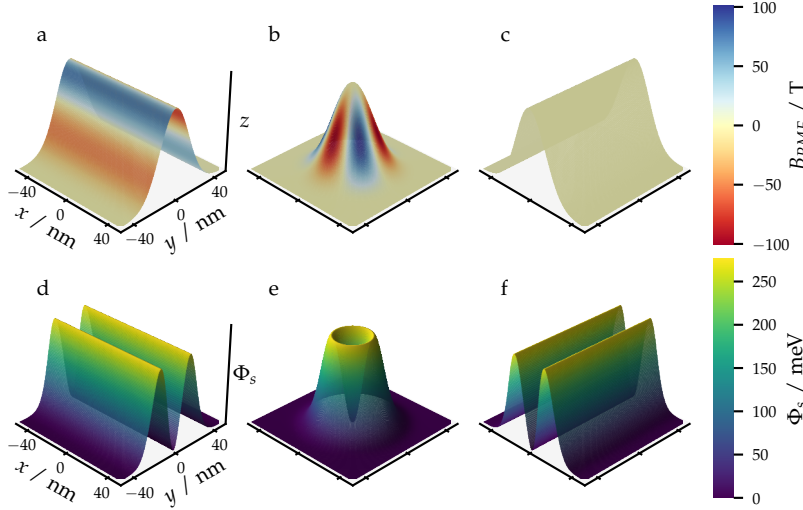


Figure 1.6: Pseudomagnetic fields and scalar potentials in strained graphene. (a-c) Topographic height profile of a zigzag-oriented fold (a), a bubble (b), and an armchair-oriented fold (c), coloured to show the resulting PMF, found from Equation 1.12. (d-f) Corresponding scalar potentials of the deformations, found from Equation 1.10. Height profiles are modelled as Gaussian functions of  $y$ , radius and  $x$ , with height 10 nm and width 20 nm.  $\epsilon_{bi}$  is calculated from the local displacement, neglecting any lateral shift.

For two neighbouring atoms, originally a distance  $a$  apart, strain in the lattice will alter their separation. We can denote the modified nearest-neighbour distance by  $a^{(\epsilon)}$ . This will induce a further modification to the nearest-neighbour hopping potential given by

$$\gamma_0^{(\epsilon)} = \gamma_0 e^{-\beta_\epsilon \left( \frac{a^{(\epsilon)}}{a} - 1 \right)}, \quad (1.9)$$

where  $\gamma_0^{(\epsilon)}$  is the modified hopping energy and  $\beta_\epsilon$  is a decay constant, empirically determined to be  $\sim 3$  [14].

From equation 1.3, we can see that this will result in a change to the electronic dispersion of graphene. In practice this change can be represented by new scalar and pseudovector<sup>1</sup> potential fields,  $\Phi_s$  and  $A_{PV}$ , added to the existing electronic potential landscape. These can be determined from the biaxial strain tensor by

$$\Phi_s = g_s (\epsilon_{xx} + \epsilon_{yy}), \quad (1.10)$$

where  $g_s$  is a coupling constant, and

$$A_{PV} = -\frac{\hbar\beta_\epsilon}{ae_q} \begin{pmatrix} \epsilon_{xx} - \epsilon_{yy} \\ -2\epsilon_{xy} \end{pmatrix}, \quad (1.11)$$

where the zigzag direction is oriented along the  $x$ -axis [14–16]. The value of  $g_s$  is disputed but often quoted as  $\sim 3$  eV [14]. It is also often convenient to analyse the pseudovector potential via its corresponding pseudomagnetic field (PMF), calculated as

$$B_{PMF} = \nabla \times A_{PV}. \quad (1.12)$$

Equation 1.11 reveals that the orientation of a strain to the lattice will have a strong effect on the resulting pseudovector potential and PMF. This is illustrated in figures 1.6 (a-c), which show the height profile and PMF calculated for a fold along the zigzag direction, a bubble, and a fold along the armchair direction. By comparison,

<sup>1</sup> Pseudovectors are identical to regular vectors except that their orientations are flipped when they undergo reflection. Many common physical parameters, including magnetic field and angular momentum, are described by pseudovectors, not vectors.

the scalar potentials shown in figures 1.6 (d-f) do not depend on the strain orientation.

A key feature of the pseudovector fields and PMFs is that their influence has opposite sign for electrons in the  $\mathbf{K}$  and  $\mathbf{K}'$  valleys, meaning they have been proposed as possible mechanisms for *valleytronic* devices, which could encode information into the valley polarisation [16–18].

The effects of nanoscale strains on graphene have been probed experimentally in several pivotal works.

For example one-dimensional (1d) folds, like those shown in figures 1.6 (a) and (c) have been used to fabricate devices, whose behaviour varies from that of a single electron transistor to that of an electronic Fabry-Perot cavity, depending on the fold orientation [19]. And in strained graphene nanobubbles, like the one shown in figure 1.6 (b), the strong effective fields cause electrons to move in quantized Landau-like orbitals, leading to discretisation of the DOS. These have been resolved via scanning tunnelling microscopy (STM) spectroscopy, with measured PMFs as high as 300 T reported [20].

### 1.1.3 Light-matter interaction in graphene

For charge-neutral graphene, the lack of a bandgap means that a wide range of photon energies,  $E_{ph}$ , resonantly excite electrons from the valence band edge to the conduction band edge. These interband transitions are the dominant absorption process for light across the near-infrared (IR), visible and ultraviolet regions of the electromagnetic spectrum, leading to a flat, universal absorption value of  $\pi\alpha_{fs} \approx 2.3\%$ , where  $\alpha_{fs}$  is the fine structure constant [21]. This regime is depicted in figure 1.7 (a).

For graphene doped away from the Dirac point, certain interband transitions are blocked due to the Pauli principle: electrons cannot be excited to filled states, or from empty states. This process, known as Pauli blocking [22], occurs for photons with  $E_{ph} < 2E_F$ , due to the symmetry between the conduction and valence bands. This is depicted in figure 1.7 (b). In this regime, light can still be absorbed via intraband transitions due to the free carriers in graphene. This yields a light response typical of metals, which can be described by the Drude model of conduction. It is typically the dominant absorption process for light in the terahertz region.

The degree of light-matter interaction can be quantified through the frequency-dependent optical conductivity,  $\sigma(\omega)$ , which relates the current density,  $J$ , to the light's electric field,<sup>2</sup>  $E$ , as

$$\begin{aligned} J(\omega) &= \sigma(\omega)E(\omega), \\ E(\omega) &= E_0 e^{-i\omega t}, \end{aligned} \quad (1.13)$$

where  $E_0$  is the field amplitude,  $t$  is time, and  $i$  is the imaginary unit.

The random phase approximation (RPA)<sup>3</sup> [22] can be used to calculate the optical conductivity, taking into account both inter- and

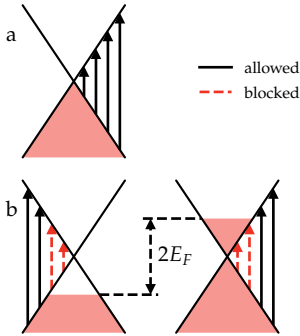


Figure 1.7: Interband optical transitions in charge-neutral (a) and doped (b) graphene.

<sup>2</sup> I use a capital E to represent both energy and electric field. Electric field (a vector quantity) will always be printed in bold to avoid ambiguity.

<sup>3</sup> In this thesis I discuss only the local RPA. For detail on the  $k$ -dependent non-local RPA see references [22, 23].

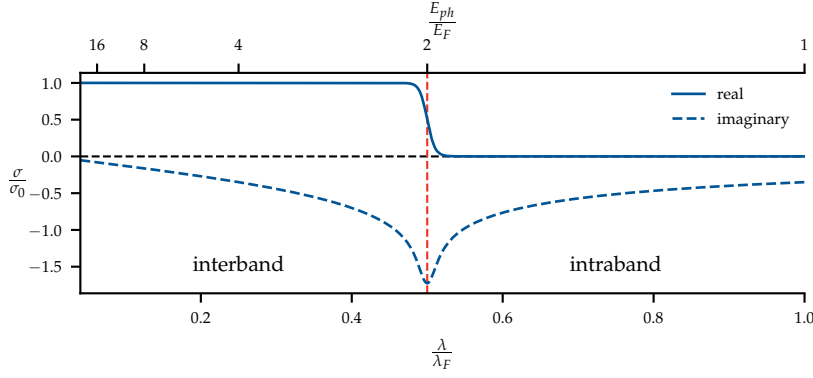


Figure 1.8: Graphene optical conductivity calculated with Equation 1.14, using  $E_F = 250$  meV,  $v_F = 10^6$  ms $^{-1}$ ,  $T = E_F/(100k_B)$  and  $\tau = 500$  fs. The vertical dashed line shows the Pauli transition.

intraband processes:

$$\sigma(\omega) = \frac{2e_q^2 T i}{\pi \hbar \left(\omega + \frac{i}{\tau}\right)} \ln \left[ 2 \cosh \left( \frac{E_F}{2k_B T} \right) \right] + \frac{e_q^2}{4\hbar} \left[ H\left(\frac{\omega}{2}\right) + \frac{4i\omega}{\pi} \int_0^\infty \frac{H(\omega') - H\left(\frac{\omega}{2}\right)}{\omega^2 - (2\omega')^2} d\omega' \right], \quad (1.14)$$

where  $\tau$  is the carrier relaxation time,  $T$  is the temperature,  $k_B$  is the Boltzmann constant and

$$H(\omega) = \frac{\sinh\left(\frac{\hbar\omega}{k_B T}\right)}{\cosh\left(\frac{E_F}{k_B T}\right) + \cosh\left(\frac{\hbar\omega}{k_B T}\right)}.$$

The first term in Equation 1.14 reduces to the Drude model as  $T \rightarrow 0$  and describes the contribution from intraband scattering. The second term describes the contribution from interband scattering. For  $E_{ph} \gg 2E_F$ , the equation tends to the universal conductivity value of graphene

$$\sigma_0 = \frac{\pi e_q^2}{2h}, \quad (1.15)$$

where  $h$  is the regular Planck constant.

Figure 1.8 shows the calculated optical conductivity as a function of wavelength,  $\lambda$ . For the sake of generality, I have shown  $\sigma$  in units of  $\sigma_0$ ,  $E_{ph}$  in units of  $E_F$  and  $\lambda$  in units of  $\lambda_F = E_F/(hc_0)$ , where  $\lambda_F$  is the wavelength of light with energy  $E_F$ , and  $c_0$  is the speed of light in vacuum. The regions either side of the Pauli transition are labelled according to which type of electronic transitions dominate the absorption characteristics: interband for the high-absorption regime on the left, and intraband for the Drude regime on the right.

The conductivity in figure 1.8 was calculated using a low temperature of  $T = E_F/(100k_B)$  to better show the transition between regimes. At higher temperatures the transition is broadened due to Fermi-Dirac statistics.

Figure 1.9 shows the real part of  $\sigma$  calculated at room temperature for a typical range of doping values in graphene devices. It shows the changing wavelength of the Pauli transition, at  $E_F/(2hc_0)$ , across

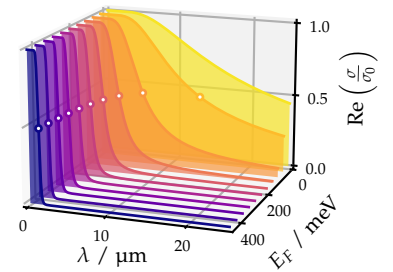
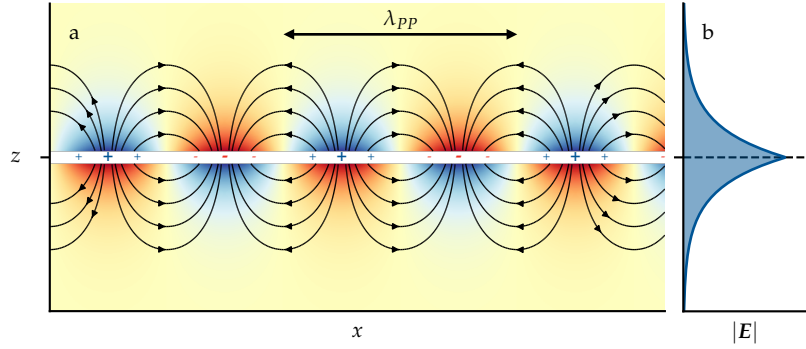


Figure 1.9: Doping dependence of graphene's optical conductivity. Real part of  $\sigma$  calculated with Equation 1.14, using  $v_F = 10^6$  ms $^{-1}$ ,  $T = 300$  K and  $\tau = 500$  fs. The white circles show the Pauli transition centre for each  $E_F$ .

Figure 1.10: Diagram of PPs in graphene. **(a)** A free-standing single layer of graphene at  $z = 0$  (white rectangle), with positive and negative charge density indicated by  $+$  and  $-$ . Colours show the  $z$ -component of the  $E$ -field and curved arrows indicate the field direction. **(b)** Magnitude of the  $E$ -field decays exponentially with distance from the graphene.



the IR region. This indicates that the optical response of graphene in the IR depends strongly on doping.

It is often useful to model graphene with a volumetric permittivity instead of a delta-function conductivity.<sup>4</sup> This can be found using

$$\epsilon = \epsilon_r + \frac{i\sigma(\omega)}{\epsilon_0\omega d}, \quad (1.16)$$

where  $\epsilon_r$  is the relative background dielectric function and  $d$  is the thickness of the graphene [24].

#### 1.1.4 Graphene plasmonics

One reason that graphene is a highly sought-after material for applications in the mid-IR is that it supports uniquely confined, long-lived and tunable plasmon polaritons (PPs) [22].

PPs are hybrid light-matter quasiparticles, formed of electromagnetic (EM) waves travelling parallel to the surface of a 2d conductor, strongly coupled to oscillations in the density of the mobile charge carriers. These charge density oscillations are called plasmons, and they can exist in bulk as well as 2d materials.

Figure 1.10 (a) shows a side-on schematic of a PP in SLG. Polarisation in the charge density of the graphene induce electric fields at the surface, which can in turn induce further electric polarisations to the material. For certain oscillation frequencies,  $\omega$ , this forms a propagating wave, with wavelength  $\lambda_{PP}$  and energy  $\hbar\omega$ .

The fields in a PP are evanescent, meaning they decay exponentially from the surface and do not propagate away from the material as shown in 1.10 (b). We refer to EM phenomena like these as *near-field* oscillations to distinguish them from regular *far-field* light, which does propagate away from the material.

On top of this surface confinement, PPs also have a remarkable degree of in-plane spatial confinement, which means that  $\lambda_{PP}$  is typically much shorter than the wavelength of a far-field EM wave with the same energy. This is a very attractive property for the field of nanophotonics, the science of manipulating light at much lower length scales than would usually be allowed by the diffraction limit.

Similar plasmonic quasiparticles called surface plasmon polaritons (SPPs) exist at the interfaces of bulk conductors. The practice

<sup>4</sup>For example, when modelling scanning near-field optical microscopy (SNOM) measurements of multilayer heterostructures, as described in section 3.2.1.

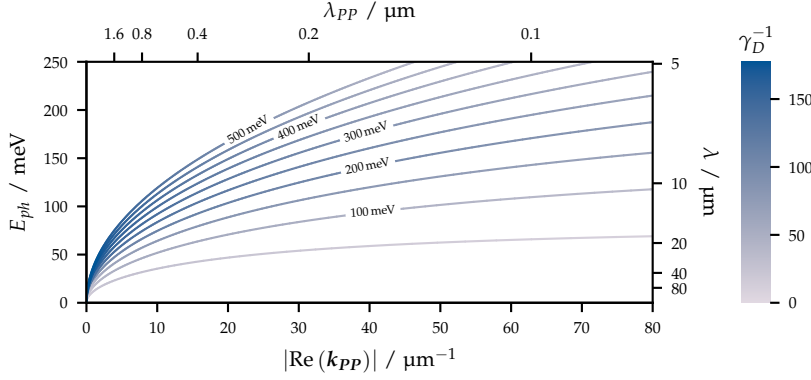


Figure 1.11: Dispersion of PPs in graphene calculated with equations 1.14 and 1.17, using  $\epsilon = 2$ ,  $v_F = 10^6 \text{ ms}^{-1}$ ,  $T = 0 \text{ K}$  and  $\tau = 500 \text{ fs}$ .

of exploiting PPs and SPPs for nanophotonics is often referred to as plasmonics. Efforts have historically focused on metals, particularly gold and silver, however these have been limited by losses in the materials, which mean that SPP excitations decay quickly over short length scales. A significant advantage presented by graphene is that its PPs are much more long-lived.

We can discuss this more quantitatively by referring to the complex PP wavevector, which describes the plasmonic dispersion. For graphene doped above the Pauli threshold,<sup>5</sup> this can be calculated from

$$k_{PP}(\omega) \approx i \frac{\epsilon_0 \epsilon(\omega)}{\sigma(\omega)} \omega \quad (1.17)$$

where  $\epsilon(\omega)$  is the sum of the frequency dependent permittivities of the materials above and below the graphene [25]. The real part of  $k_{PP}$  is related to the PP wavelength as

$$|\text{Re}(k_{PP})| = \frac{2\pi}{\lambda_{PP}}, \quad (1.18)$$

and the imaginary part relates to the lifetime of the oscillation. This is typically described using the inverse damping ratio, given by

$$\gamma_D^{-1} = \frac{|\text{Re}(k_{PP})|}{|\text{Im}(k_{PP})|}, \quad (1.19)$$

which gives the phase (number of oscillations times  $2\pi$ ) a PP can propagate before losses reduce its amplitude to  $e^{-1}$  times its starting value.

Inverse damping ratios for metal SPPs can be up to  $\sim 36$  [26], whereas values as high as 130 have been measured for hexagonal boron nitride (hBN)-encapsulated graphene PPs at cryogenic temperatures [26]. For lower mobility samples on less ideal substrates and at higher temperature, this will be reduced due to an increase in scattering-related losses.

A significant advantage presented by graphene is the electrical tunability of its plasmonic dispersion. I showed in section 1.1.3 that the optical conductivity of graphene,  $\sigma(\omega)$ , depends strongly on the Fermi level, which can be effectively tuned using the field effect. By

<sup>5</sup> Below this doping, interband transitions should dominate the light-matter interaction, meaning the optical conductivity deviates from Drude-type behaviour and we should not expect a significant contribution from PPs.

substituting equation 1.14 into 1.17, we can calculate the frequency dispersion of PPs at arbitrary doping.

Figure 1.11 shows the dispersion and inverse damping ratio calculated at a range of Fermi levels, for free-standing graphene. This shows that for a PP of a particular energy, its wavelength can be effectively controlled electrically by gating, a feature which has been exploited to great effect in subwavelength optical modulation devices [8]. It also shows that the highest inverse damping ratios, and therefore longest lasting PPs, exist at highest doping.

Another often-used figure of merit in plasmonics is the confinement factor, given by

$$\beta_{PP} = \frac{\lambda}{\lambda_{PP}} = \frac{|\text{Re}(k_{PP})|}{k}, \quad (1.20)$$

where  $\lambda$  and  $k$  are the wavelength and wavenumber of the corresponding far-field light with the same energy. For graphene this can be as high as 150 [23].

One reason for this is the 2d nature of graphene. In the case where the thickness of a metal is shorter than its skin depth, plasmons can couple to EM waves at both interfaces (as depicted in figure 1.10), which leads to stronger confinement of the electric fields. As graphene is only a single atom thick, it can be seen as the ultimate realisation of this effect [27].

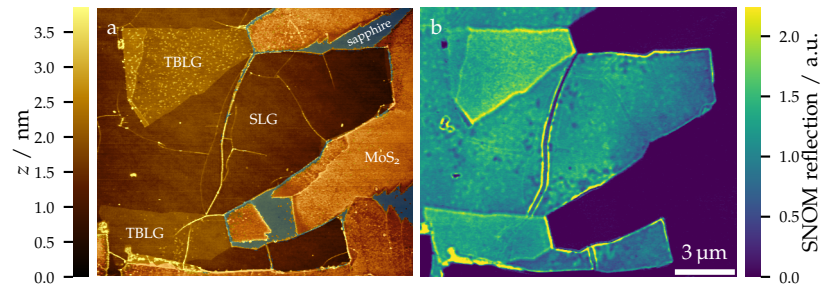
High  $\beta_{PP}$  values are key for nanophotonics, as they allow miniaturisation of devices, but they also present a problem when trying to couple far-field light into PPs. In any interaction, both energy and momentum must be conserved. This means that to excite a PP, the in-plane component of the far-field wavevector,  $k_{\parallel}$ , must be equal to  $\text{Re}(k_{PP})$ . But for any non-unity  $\beta_{PP}$  value, there is a momentum mismatch between the PP and the far-field light, which needs to be overcome.

A typical way to achieve this in graphene is to put nanoparticles or metal contacts in contact with the material. These act as antennas for the far-field light, and the small size or sharp aspect ratio provides the necessary momentum to overcome the mismatch.

A common technique to image plasmonic behaviour is SNOM,<sup>6</sup> which uses a laser focused on a sharp metal tip to both excite and detect PPs. Figure 1.12 is a SNOM image taken from a chemical vapour deposition (CVD) graphene sample. It shows typical bright

<sup>6</sup> For more details on this technique see section 3.2.

Figure 1.12: Example image of PPs in graphene. (a) Topography image showing the height of the sample as determined by atomic force microscopy (AFM) (see chapter 3). Other materials present are labelled: the sapphire substrate, MoS<sub>2</sub> (see section 2.1.2), and some TBLG (see section 1.2.2) formed by folds in the graphene. (b) SNOM reflection image showing the in-phase component of the near-field scattered light. PPs are visible as bright fringes around features in the graphene. The far-field excitation wavelength was 10  $\mu\text{m}$ .



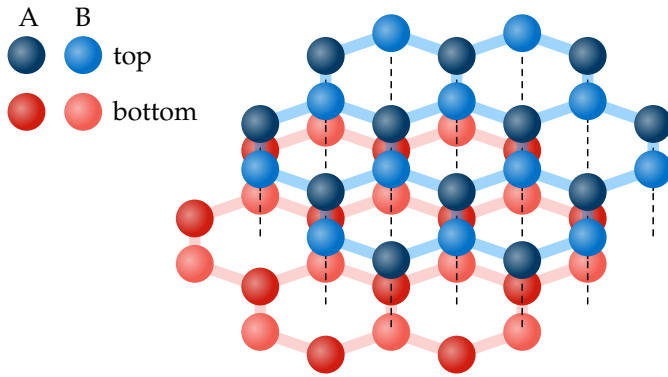
fringes around adsorbed nanoparticles, where PPs are excited, and edges, where PPs induced by the sharp tip are reflected back to form standing waves. The low mobility and high disorder in this sample means that PPs decay quickly, such that only one fringe is discernible in the standing waves.

## 1.2 Bilayer graphene

Bilayer graphene (BLG) is formed of two layers of graphene, stacked one atop the other. It has distinct properties from SLG, which make it an interesting material in its own right.

Figure 1.13 shows the structure of a common form of BLG, known as AB-stacked<sup>7</sup> or Bernal-stacked bilayer. In this configuration, both graphene layers have the same orientation, the A atoms of one layer are aligned above or below the B atoms of the other layer, and the remaining atoms are aligned with the gaps in the middle of hexagonal cells.

This is the most energetically favourable alignment for the two layers, and it is the typical form for BLG which has been mechanically exfoliated from bulk graphite. Other possible alignments are referred to as twisted bilayer graphene (TBLG), which will be discussed in 1.2.2. In the rest of thesis, when I refer to BLG it will generally mean Bernal-stacked bilayer.



<sup>7</sup>This name derives, not from the A and B atoms in the graphene unit cell, but from the labels given to alignments of hexagonal close-packed structures in crystallography.

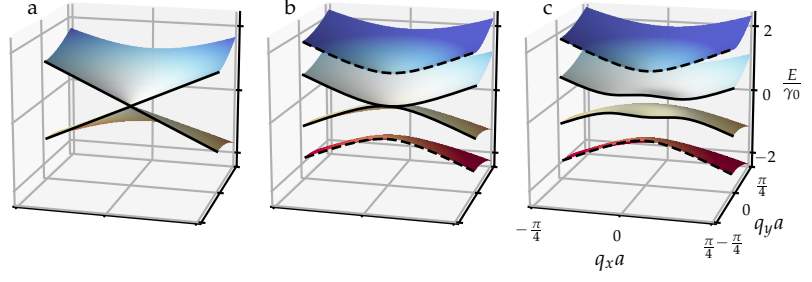
Figure 1.13: Bernal-stacked bilayer graphene. Vertical alignments between the top and bottom layers are shown by dashed lines.

### 1.2.1 Band structure of bilayer graphene

In a tight binding approach, electronic coupling between the two layers of BLG means that additional hopping parameters, accounting for electrons moving between atoms in the top and bottom layers, must be considered. In this thesis I shall only consider the potential associated with an electron hopping to or from its immediate vertical neighbour,  $\gamma_1$  [10].

The  $\mathbf{K}$ -point dispersion for SLG and BLG are shown in figures 1.14 (a) and (b). Accounting only for hopping potentials  $\gamma_0$  and  $\gamma_1$ ,

Figure 1.14: Bilayer graphene  $\mathbf{K}$ -point band structure. (a) SLG Dirac cone, shown for comparison. (b) BLG band structure, calculated from equation 1.21, using  $\gamma_1 = \gamma_0$ . (c) BLG band structure in an electric field, calculated from equation 1.22, using  $\gamma_1 = \gamma_0$  and  $\Delta E_F = 2\gamma_0/3$ .



the BLG band structure can be approximated by

$$E(\mathbf{q}) = \pm \sqrt{v_F^2 |\mathbf{q}|^2 + \frac{\gamma_1^2}{2}} \pm \sqrt{\gamma_0^2 v_F^2 |\mathbf{q}|^2 + \frac{\gamma_1^4}{4}}. \quad (1.21)$$

This results in a pair of bands which touch at an infinitesimal point at charge neutrality, as for SLG, but with parabolic, rather than linear dispersion (marked with solid lines) as well as an additional pair of bands, which are displaced in energy by  $\pm\gamma_1/2$  (marked with dashed lines).

If bilayer graphene is placed in a vertically oriented electric field, a difference in Fermi level,  $\Delta E_F$ , will be induced between the layers by the field effect. This will modify the electronic dispersion to

$$E(\mathbf{q}) = \pm \sqrt{\frac{\Delta E_F^2}{4} + v_F^2 |\mathbf{q}|^2 + \frac{\gamma_1^2}{2}} \pm \sqrt{(\gamma_0^2 + \Delta E_F^2) v_F^2 |\mathbf{q}|^2 + \frac{\gamma_1^4}{4}}. \quad (1.22)$$

As shown in figure 1.14 (c), this results in the formation of a bandgap, and a transition from a semimetal to a semiconductor [10]. This is an important result, as it shows that the bandgap of BLG can be effectively controlled in devices by electrical gating.

### 1.2.2 Twisted bilayer graphene

When the top and bottom BLG layers are rotated relative to each other, a material called twisted bilayer graphene (TBLG) is formed. The properties of TBLG depend strongly on the twist angle,  $\theta_t$ , and specific angles lead to a diverse range of exotic and unexpected behaviours including superconductivity [9], correlated insulator phases [28] and ferromagnetism [29].

This tunability arises from the moiré pattern which is introduced by non-zero twist angles. These are composed of alternating regions of in- and out-of-phase alignment between the constituent lattices. Figure 1.15 shows moiré patterns for three different twist angles with the periodicity indicated by arrows. Small twist angles lead to large moiré periods, which shrink with increasing  $\theta_t$  up to the maximum misalignment at  $30^\circ$ , after which further twisting actually reduces the misalignment because of the 6-fold rotational symmetry of graphene.

Moiré patterns therefore introduce a twist-dependent superlattice potential, which interacts with the existing graphene lattice and leads

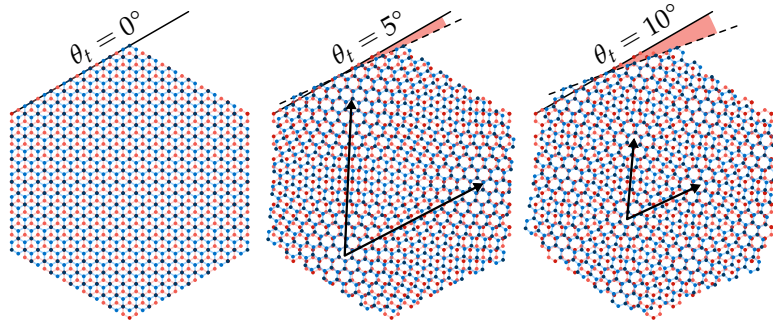


Figure 1.15: Moiré patterns in TBG. Arrows indicate the moiré period for the non-zero twist angles.

to modification of the electronic dispersion. A qualitative description of a mechanism for these changes at small angles is presented in figure 1.16.

To begin with, it is easiest to think of the top and bottom layers as independent sheets of SLG, with no electronic coupling. A rotation in real space also appears as a rotation by the same angle in reciprocal space. This means that the BZs associated with each layer will be rotated relative to each other by  $\theta_t$ , as depicted in figure 1.16 (a). This causes an offset to the  $\mathbf{K}$  and  $\mathbf{K}'$  points and therefore pairs of overlapping Dirac cones, as shown by the cross-section in figure 1.16 (b). If we now consider the effects of the electronic coupling of the top and bottom layers, the result is a hybridisation of the individual band structures, where band edge intersections are replaced with avoided crossings [28].

At different twist angles, these intersections will appear at different energies and  $k$ -space positions, which results in a complicated formation of new bands. At certain low twist angles, termed *magic angles*, these bands are extremely flat, which leads to a vanishing Fermi velocity and leads TBG to behave as either a superconductor or correlated insulator [9, 28].

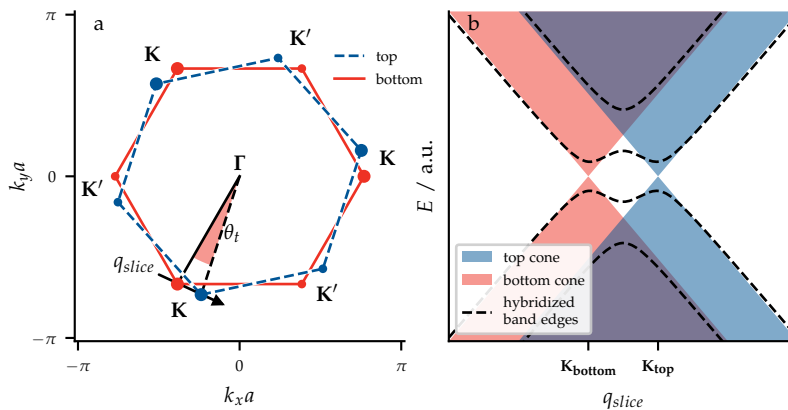


Figure 1.16: Qualitative description of TBG twist dependence. (a) BZ of TBG. (b) Cross-section of the  $\mathbf{K}$ -point band structure of TBG taken from the location indicated in (a).

### 1.3 *Conclusions*

In this chapter I presented a brief overview of some of the most important physics governing the behaviour of graphene. I have shown that, despite its simple structure, it boasts a wide range of exciting properties which make it attractive for electronic and optoelectronic applications. In the rest of this thesis, I will study these in detail, as well as the properties of other van der Waals materials and heterostructures, which are introduced in the following chapter.

## 2

# *Van der Waals materials and heterostructures*

The family of two-dimensional (2d) materials is rich and diverse, but some of the most exciting materials are still often overshadowed by graphene, their more famous cousin. This is likely to change, as more and more research is published on the exotic properties of non-graphene 2d materials.

Most of these of these materials have a bulk form similar to graphite, in which the atoms lie in covalently bonded sheets held together by van der Waals (vdW) forces. For this reason they are often referred to as vdW materials, a term which includes their bulk form, as well as their few- and monolayer forms. Much of the groundbreaking work today focuses on the varied effects of layering different 2d materials into stacks called, vdW heterostructures.

In this chapter I give an overview of the properties of some of the most common vdW materials today, including a discussion of some of the different methods to produce them. I also cover the properties of vdW heterostructures, with a section on bubble formation and self-cleaning behaviour which will be important later in this thesis.

### *2.1 Van der Waals materials beyond graphene*

#### *2.1.1 Hexagonal boron nitride*

Monolayer hexagonal boron nitride (hBN) is structurally very similar to graphene [30], as shown by the diagram in figure 2.1. It also has a planar hexagonal structure with a two-atom basis, but with the A and B carbon atoms replaced with boron and nitrogen atoms.

However unlike the pure covalent bonds in graphene, the boron and nitrogen atoms in hBN form polar covalent bonds, which mean that hBN is effectively an insulator with a wide indirect bandgap of  $\sim 6$  eV [4].

It is often used in its few-layer or bulk form. By far, the most common use for hBN is as an insulating substrate and capping layer for graphene and other 2d materials, which is discussed in detail in section 2.2.1. But it also has some interesting properties of its own.

Many materials are birefringent, which means that their refractive

Figure 2.1: Hexagonal boron nitride lattice structure. The structure is depicted in top-down, and two side-on projections.

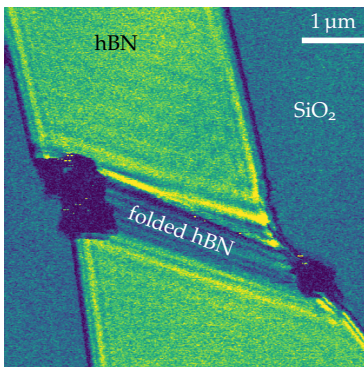
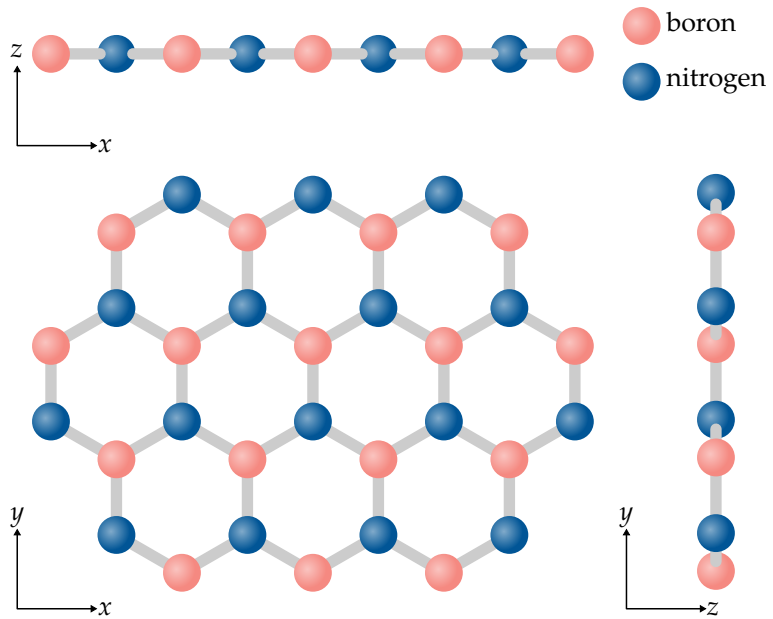


Figure 2.2: Example image of hyperbolic phonon polaritons (HPhPs) in hBN. SNOM third-harmonic amplitude scan, captured at  $1550\text{ cm}^{-1}$ .

<sup>1</sup> Quasiparticles associated with vibrations in a crystal lattice.

<sup>2</sup> For more details on this technique see section 3.2.

index is different along different crystal axes, however hBN has a specific kind of birefringence known as optical hyperbolicity [31]. This means that not just the magnitude, but also the sign, of the refractive index is different, which results in an extreme anisotropy of the dispersion of light through the material. These materials can be used for applications like diffraction-beating hyperlenses [32, 33].

There are two kinds of optical hyperbolicity, referred to as types I and II, which vary according to whether only one or two axes have a negative real part of the refractive index. hBN features both of these in different frequency bands, called the upper and lower reststrahlen bands, which occur for light of wavelengths around  $6.2\text{-}7.3$  and  $12.1\text{-}13.2\text{ }\mu\text{m}$  [31]. For both bands the anisotropy is between the in- and out-of-plane directions of the crystal.

One consequence of the hyperbolicity is that in the reststrahlen bands, phonons<sup>1</sup> in the hBN can couple strongly to infrared (IR) light to form a combined light-matter oscillation called a phonon polariton [34, 35]. These are similar to the graphene plasmon polaritons (PPs) discussed in section 1.1.4, but the charge polarisation is associated with the vibration of bound charges, rather than with oscillations in the density of free carriers. As these occur in the bands where hBN is hyperbolic, they are often referred to as HPhPs.

An example of a scanning near-field optical microscopy (SNOM),<sup>2</sup> image showing HPhPs in the upper reststrahlen band of hBN, reflecting from the edges of a flake and launched from a fold is shown in figure 2.2.

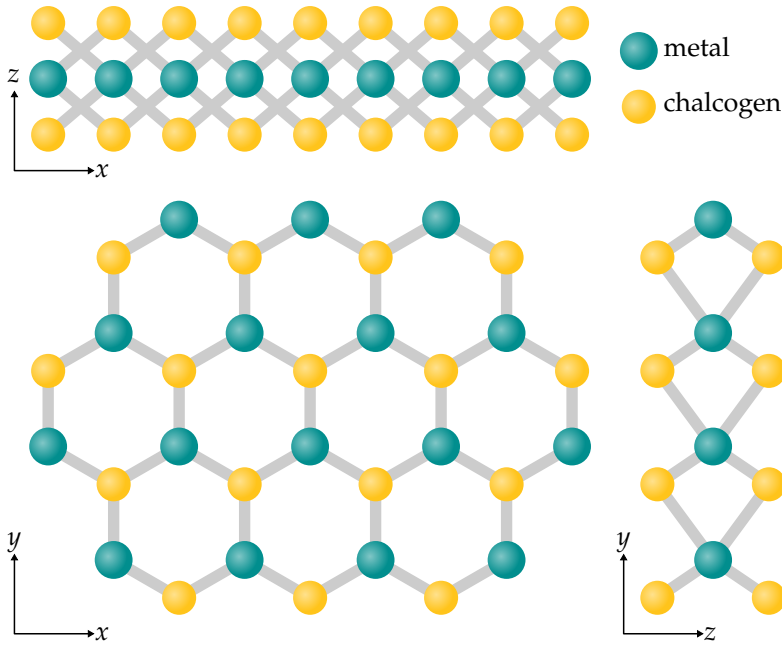


Figure 2.3: transition metal dichalcogenide (TMD) lattice structure. The 2H phase is depicted in top-down, and two side-on projections. The label “metal” here refers specifically to the transition metals.

### 2.1.2 Transition metal dichalcogenides

TMDs are a group of 2d layered materials with the chemical formula  $\text{MX}_2$ , where M represents a transition metal atom, commonly W or Mo, and X represents a chalcogen atom, S, Se or Te [2].

There are multiple stable phases for TMD atomic configurations, but they are typically studied in their 2H phase, which is shown in figure 2.3. Unlike graphene and hBN, a monolayer of a TMD consists of three separate atomic layers, with the metal atoms sandwiched between two layers of chalcogen atoms. For this reason figure 2.3 shows both top-down and side-on views of the lattice. The top-down view shows that despite the displaced chalcogen atoms, the in-plane structure is still hexagonal in form.

TMDs are semiconductors, which lends them much more promise for optoelectronic applications than the gapless graphene. Particularly so because when they are thinned down from bulk to monolayer, they undergo a transition from an indirect to a direct bandgap at the  $\mathbf{K}$  and  $\mathbf{K}'$  points [36]. This can be shown experimentally by an extreme enhancement of the photoluminescence (PL)<sup>3</sup> emitted by the monolayer compared to bilayer, when they are excited by light with energy above their bandgap [37].

This PL results from quasiparticles called excitons, composed of a coulombically bound conduction band electron and valence band hole. These are created when a photon promotes an electron above the bandgap, and their recombination leads to light emission at the difference between the bandgap and exciton binding energies. Compared to bulk semiconductors, 2d TMDs have very weak dielectric screening and high spatial confinement of charge carriers. This leads to very high binding energies, meaning TMD excitons persist, even

<sup>3</sup> For more detail on this technique see section 4.1.2.

at room temperature, which makes them exciting candidates for a range of applications including light detection and emission, as well as spin- and valleytronic devices [2].

### 2.1.3 Post-transition metal chalcogenides

Post-transition metal chalcogenides (PTMCs), also called III-VI compounds, are a group of 2d layered materials composed of group-III atoms, typically In or Ga, and chalcogen atoms. These can have different stoichiometries, AX or  $A_2X_3$ , where A represents a group-III atom and X represents a chalcogen atom, and can exist in multiple phases for each stoichiometry [38].

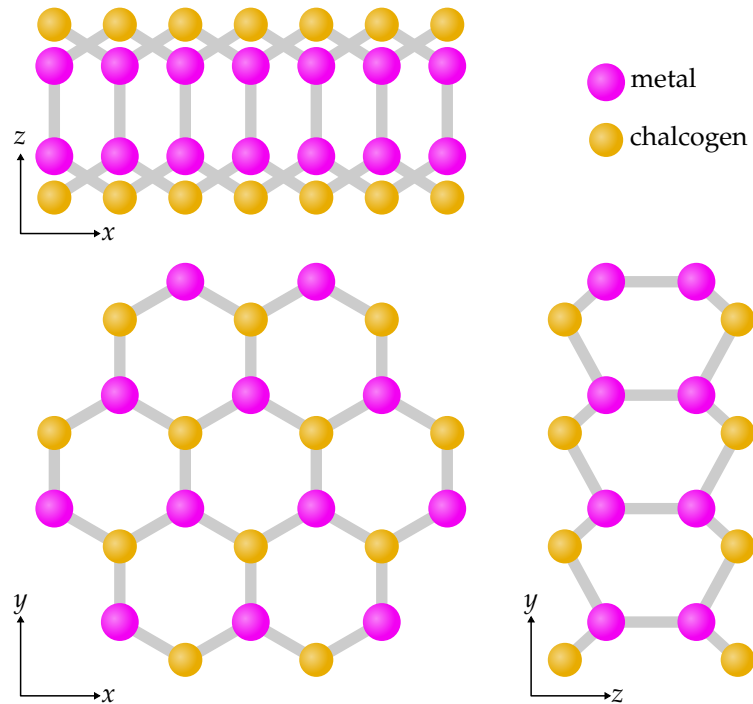
Figure 2.4 shows the structure of AX PTMCs in their  $\gamma$  phase. This is similar to that of the 2H-TMDs, except instead of a 3-atomic-layer structure, there are four layers, with a bilayer of group-III atoms sandwiched between the chalcogens.<sup>4</sup> Once again, the top-down view of the structure shows the in-plane structure is hexagonal [2].

Indium selenide compounds are the most studied of the PTMCs, and they have shown some distinct properties from those of many other 2d materials. Like the TMDs, InSe is a semiconductor, but conversely to TMDs it has a direct bandgap in its bulk form which becomes indirect when it is thinned down to monolayer [39]. The bandgap energy also increases significantly with fewer layers [40]. On top of this, InSe has also shown much higher values of electron mobility than TMDs [41], as well as an anomalously low thermal conductivity [42].

The properties of  $\gamma$ -phase InSe are studied in chapter 7.

<sup>4</sup> For  $A_2X_3$  compounds, which I haven't shown here, there are typically five layers, which alternate XAXAX.

Figure 2.4: PTMC lattice structure. The  $\gamma$  phase, with AX stoichiometry, is depicted in top-down, and two side-on projections. The label "metal" here refers specifically to the group-III metals.



#### 2.1.4 Other 2d and van der Waals materials

So far, I have introduced some of the most commonly studied materials of today, with a particular focus on those materials used in my own research. But the modern family of 2d materials is far vaster than I could cover in a single chapter, and is expanding every day.

On top of the conducting, semiconducting and insulating behaviour I've already introduced, many other desirable material properties have now been demonstrated in 2d materials, including magnetism [43, 44], piezoelectricity [19], ferroelectricity [45] and even superconductivity [9, 46].

For a comprehensive review of non-graphene 2d materials, you can read our paper *Opportunities in electrically tunable 2D materials beyond graphene: Recent progress and future outlook* in the journal *Applied Physics Reviews* (see [Dissemination](#)).

#### 2.1.5 Fabricating 2d materials

There are many ways to produce vdW materials, which vary in terms of their yield, purity, defect density and number of layers of the samples produced [47]. In this section I'll give a brief overview of two of the most common techniques today, restricting the discussion to the techniques which produced samples used in this thesis.

*Mechanical exfoliation* Also referred to as the Scotch tape method, this is the first method by which any 2d materials were isolated [1].

It involves repeatedly pressing a bulk vdW crystal between two pieces of adhesive tape, then pulling them apart. As this happens the bulk crystal remains stuck to the adhesive, so it cleaves along the weak vdW planes. After several iterations, the tape will have a high coverage of few layer crystals and it can be pressed against a desired substrate. Finally, when the tape is peeled back, vdW forces mean that the few layer crystals cleave once more, leaving a high coverage of few- and monolayer crystals behind.

An advantage of this technique is the low defect density and high purity of the crystals produced, which means it is still typically the method of choice for producing high-mobility samples for electronics and optoelectronics research [9, 11]. However a significant drawback is that the method is non-deterministic, meaning lots of time must be spent inspecting the substrate to search for crystals of the desired thickness. This means it is not easily scalable, so it is more suited to research than to mass production.

*Chemical vapour deposition* This is a growth technique which can produce a range of 2d material samples and heterostructures [48].

There is wide variation in how chemical vapour deposition (CVD) is performed but in all methods, a substrate is placed in a reaction chamber with a controlled environment consisting of one or more volatile precursor gases. These precursors react to form thin films of a desired material on the growth substrate, so they must have

the correct elemental makeup. Different substrates are successful for growing different materials, often chosen so that they both catalyse the reactions and have a well-matched crystal structure to promote epitaxial growth. Examples of typical combinations of precursors and substrates include  $\text{CH}_4$  for graphene growth on Cu [49–51], and  $\text{WO}_3$  and S for  $\text{WS}_2$  growth on Sapphire [52, 53].

CVD has a number of advantages. Multiple stages of growth can be performed sequentially, and it is possible to use 2d materials themselves as growth substrates for others. This means that CVD can be used to directly grow 2d-material heterostructures, both vertically [54–57] (see section 2.2), and in-plane [58]. On top of that, CVD has a high yield and can achieve full substrate coverage, making it attractive for commercial applications.

However there are downsides too. Typically CVD samples have a higher defect density than mechanically exfoliated ones, and they are often highly polycrystalline, meaning their carrier mobilities are limited by scattering. Additionally, the best growth substrate is not always an ideal substrate for real applications, and it is often tricky to transfer the materials without incurring damage or adding contamination.

## 2.2 *Van der Waals heterostructures*

In the section above, I discussed the unique and exciting properties of individual 2d and vdW materials. VdW heterostructures further expand the horizons of what is possible in two dimensions, by stacking different vdW layers to create brand-new materials with an even wider range of controllable properties [3].

Layers in these structures are glued together with the same vdW forces that hold bulk crystals together. We can use this concept to build fully 2d devices, which take advantage of the varied range of exotic properties available, and retain the benefits of 2d materials. For example, a field effect transistor (FET) with a high on-off ratio and exceptionally high carrier mobility can be made using a semi-conducting TMD as a channel; conductive graphene for the source and drain electrodes; and insulating hBN as a substrate and gate dielectric [59].

But the advantages of vdW heterostructures are not just from the combination of different material properties. When two materials are layered together, the resulting stack often has entirely new properties, which didn't belong to either constituent layer [3].

For one example, stacks of two different monolayer TMDs support long-lived interlayer excitons, formed when an electron or hole in a regular exciton tunnels from one material to the other [60–63]. As another, graphene PPs and hBN HPhPs can hybridise in heterostructures of the two materials, leading to altered polaritonic dispersion [23, 64]. Additionally, moiré periods which result from layering two materials with a different lattice constant add a superlattice potential,<sup>5</sup> which modifies the electronic dispersion and can result in

<sup>5</sup>This is similar to the mechanism which governs twisted bilayer graphene (TBLG), discussed in section 1.2.2.

the appearance of exotic behaviour such as the Hofstadter butterfly and fractal quantum hall effect [11, 65, 66].

### 2.2.1 Hexagonal boron nitride encapsulation

One of the foremost advances to come from the introduction of vdW heterostructures was the practice of encapsulating 2d materials with hBN. This was first demonstrated for graphene, and removed two significant barriers to the electronic performance of graphene devices.

The first of these barriers I will discuss is the charge puddling that occurs in graphene when it is placed on an imperfect substrate. The de facto standard substrate before hBN encapsulation was  $\text{SiO}_2$ , but this suffers from a rough surface<sup>6</sup> and charged surface states, which lead to small charge puddles to the graphene,  $\sim 20$  nm in size [67]. This leads to a short electronic scattering length and a corresponding limit to the carrier mobility [4].

By contrast, hBN has an atomically flat surface, it is expected to be free from dangling bonds and charged impurities, and, as boron and nitrogen neighbour carbon in the periodic table of elements, the lattice constant of hBN is only slightly larger than that of graphene, with a mismatch of  $\sim 1.8\%$  [30].

This makes it an ideal substrate for graphene devices. Indeed, for graphene on hBN, the size of the charge puddles is increased to  $\sim 800$  nm [67]. This leads to a much longer scattering length and an exceptionally high carrier mobility [11, 68].

The second barrier overcome by encapsulation is environmental doping. As for all 2d materials, the high surface-to-volume ratio of graphene means that its properties are incredibly sensitive to any molecules which come into contact with it. Atmospheric contaminants which adsorb onto the graphene's surface therefore dope the material in an uncontrollable way. A second capping layer of hBN covering the graphene means that the active surface is protected from the environment making devices significantly more stable [11].

Though I have used the example of encapsulated graphene, the benefits of hBN encapsulation described above are equally applicable to almost any other 2d material. However, the final advantage of the encapsulation I will discuss is particularly relevant to graphene: 1d edge contacts.

A particularly difficult aspect in fabricating 2d material devices is making electrical contact to the materials. If a device is limited by an overly high contact resistance, any benefits given by superior electronic quality of the active materials will be rendered irrelevant.

One way to contact graphene is by depositing metal onto its surface as depicted in figure 2.5 (a). However as graphene has no surface bonding sites, there is no orbital hybridisation between the graphene and metal, which leads to high contact resistances.

Another approach is shown in 2.5 (b). An encapsulated graphene heterostructure is etched to expose the 1d edge of the graphene, then metal is deposited over this edge, typically a mixture of Au and Pd

<sup>6</sup>This adds an inhomogeneous strain field to the graphene. See section 1.1.2, for why this presents an issue.

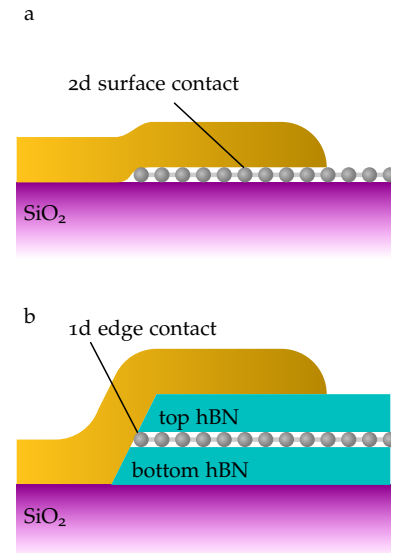


Figure 2.5: Contacting encapsulated graphene. (a) A 2d surface contact, with metal deposited over graphene. (b) A one-dimensional (1d) edge contact, with metal deposited over an etched encapsulated graphene heterostructure.

<sup>7</sup>For non-graphene 2d materials, this approach is not so effective. The typical way to make low resistance contacts to them in encapsulated heterostructures is by layering them with graphene, which acts as an electrode, then making a 1d contact to the encapsulated graphene [59].

with a Cr adhesion layer. In this case, graphene's dangling  $\sigma$  bonds are free to hybridise with the orbitals of the Cr, which leads to very low contact resistance [69].<sup>7</sup>

### 2.2.2 Bubble formation and self cleaning

A crucial feature of vdW heterostructures is their self-cleaning behaviour.

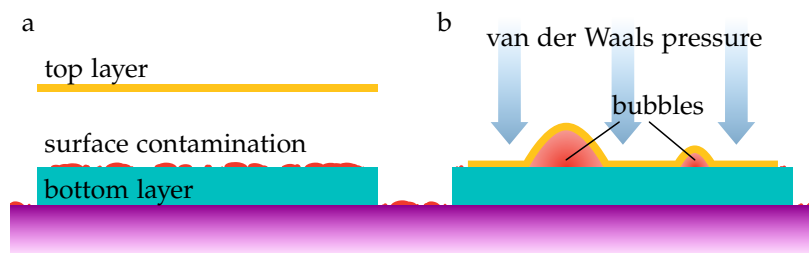
All materials which are exposed to the atmosphere are covered in a thin layer of loosely bound surface contamination, typically composed of adsorbed water and short-chain hydrocarbons [5], as shown in figure 2.6 (a). This could present a problem when stacking 2d materials: if there is a coating of contamination sandwiched in between the layers of our stack, then the idea of a vdW heterostructure with only a perfect, atomically clean vdW gap between materials will no longer be valid.

But thankfully, when two 2d material are stacked, the vdW forces between them combine with the elastic potential of the material to exert a pressure on the trapped contamination. The competing forces act to squeeze the contamination into isolated pockets, minimising the potential energy and promoting bubble formation. Between the bubbles, the interfaces in the vdW heterostructure are indeed atomically clean [3, 5, 70]. This process is shown in figure 2.6 (b).

Without this self-cleaning behaviour, vdW heterostructures would not be able to function as well as they do. Once the bubbles have formed, the sample can be rendered even cleaner by squeezing the bubbles with an atomic force microscopy (AFM) tip, forcing them to the edge of the active region [71, 72].

The bubbles which are formed are interesting to study in their own right, as they introduce highly localised strains to 2d materials. As I discussed for graphene in section 1.1.2, this alters the electronic properties of the material, which can lead to some remarkable results. A key demonstration of this for non-graphene 2d materials is that nanoscale bubbles in TMD heterostructures act as highly localised PL emitters thanks to strain-induced exciton funnelling [73].

Figure 2.6: Self cleaning in vdW heterostructures. (a) All materials in ambient conditions are coated with a thin layer of surface contamination. (b) When the materials in a vdW heterostructure are layered together, vdW pressure promotes bubble formation, leaving atomically clean interfaces elsewhere.



### 2.2.3 Fabricating van der Waals heterostructures

There are a number of ways to prepare vdW heterostructures, which vary in terms of their speed, difficulty, and the cleanliness of the resulting samples [74]. In this section I'll describe an example of one method of transfer, which is similar to the one used to create the encapsulated graphene sample in chapter 6.

Figure 2.7 shows diagrams of the steps used, numbered 1 to 6. I describe each step in detail below:

1. Using mechanical exfoliation (see section 2.1.5), hBN is deposited onto a  $\text{SiO}_2$  substrate which has been spin coated with two layers of polymer. The first layer is (poly)vinyl acetate (PVA), which is soluble in water, and the second is (poly)methyl methacrylate (PMMA), which is not.
2. The substrate is inspected and a flake of hBN of the desired size and thickness to be a capping layer is identified. A line is cut through the polymers, to define a circular membrane centred on the chosen flake. Water is carefully dripped around this hole (ensuring none covers the top of the membrane), which is drawn under the PMMA by capillary action, dissolving the PVA and releasing the membrane.
3. The membrane is picked up, inverted and affixed to a micromanipulator under a microscope with a long working distance objective. The micromanipulator can move the sample precisely in  $x$ ,  $y$  and  $z$  directions, relative to the microscope stage, which can also be moved,<sup>8</sup> and the microscope can focus through the translucent membrane to see the alignment of the hBN capping layer with a sample on the stage underneath.
4. A suitable flake is identified from graphene exfoliated onto  $\text{SiO}_2$ .
5. Using the micromanipulator, the hBN capping layer on the membrane is lowered onto the graphene. The goal is now to lift the

<sup>8</sup> The stage can be moved in  $x$ ,  $y$  and  $z$ , and often rotated too, which is useful for preparing twisted vdW heterostructures [75]

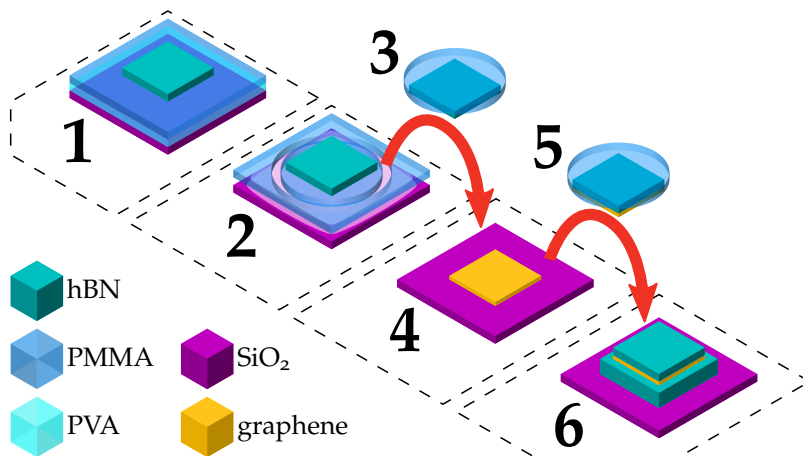


Figure 2.7: Transfer of 2d materials. An example showing the steps involved in preparing encapsulated graphene. Detailed descriptions of steps labelled 1 to 6 are given in the text.

graphene using the vdW forces between it and the hBN. Whether the graphene sticks to the hBN or stays on the SiO<sub>2</sub> depends on a number of factors which can be experimented with, including the speed that the membrane is lifted and the temperature of the substrate.

6. A suitable flake to act as a substrate for the graphene and hBN capping layer, which are now both held on the membrane, is identified from hBN exfoliated onto SiO<sub>2</sub>. The membrane is once again lowered onto the target flake, but this time, it is lifted to leave the whole hBN-graphene-hBN stack on the substrate.<sup>9</sup>

<sup>9</sup> Alternatively, the entire membrane can be left on the substrate and cleaned away with solvents. This relies on the hBN encapsulation to protect the graphene from contamination, but will still leave contamination on the hBN surface.

Though I used the example of encapsulated graphene, this technique can be applied to create stacks of any arbitrary 2d materials, where the vdW force from each layer is used to pick up the next. One advantage of this method is that, if every stage of the transfer goes smoothly, then only the top layer of the heterostructure, usually hBN, will have contacted the polymer membrane, which significantly reduces the amount of contamination.

### 2.3 Conclusions

In this chapter, I introduced the wider family of non-graphene 2d and vdW materials, and vdW heterostructures. I also reviewed some of the fabrication techniques used to create them and incorporate them into devices.

This concludes part I of this thesis, which described the important physical background of the materials I studied. In part II, I will move on to discuss the measurement techniques which I used to carry out my research.

**Part II**

**Characterising  
van der Waals materials**



## 3

# *Laser-coupled scanning probe microscopy techniques*

The most interesting features of two-dimensional (2d) materials exist on the nanoscale, far below the diffraction limit of conventional optical microscopy. Such tiny features need specialised microscopy techniques to be resolved. Since its invention in the 1980s [76, 77], scientists have used scanning probe microscopy (SPM) to image materials with sub-nanometre resolution. Today, it has expanded to encompass a whole family of related techniques, which can be used to probe a diverse range of nanoscale material properties.

SPM techniques which combine atomic force microscopy (AFM) with laser illumination, such as scanning near-field optical microscopy (SNOM), are particularly powerful for studying sub-diffraction light-matter interaction. In this chapter, I explain the basic principles of AFM, before going into further detail on some of the AFM-derived techniques used in the rest of this thesis.

### *3.1 Basics of atomic force microscopy*

An AFM produces high-resolution images by sensing a sample's surface with a mechanical probe.

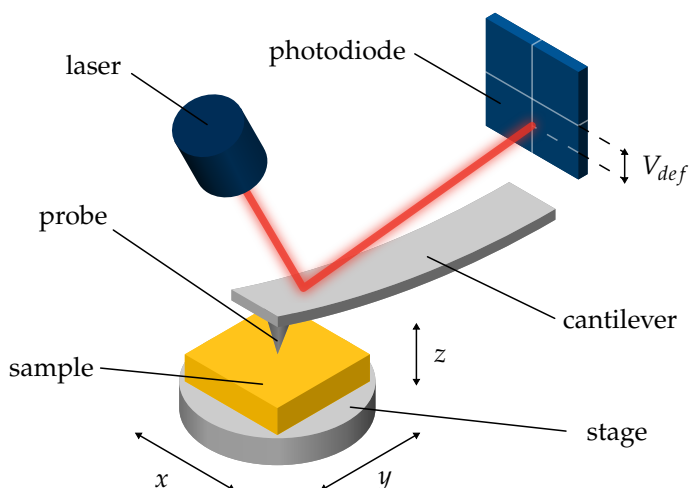
Figure 3.1 shows a schematic of a typical experimental setup. At the heart of the microscope is the AFM tip, which consists of a flexible cantilever, usually  $\sim 100 \mu\text{m}$  in length, with a sharp probe at its end. The size of the probe's apex governs the microscope's lateral resolution, which is typically  $\sim 20 \text{ nm}$ , but may be even smaller.

When the tip is moved close to a sample, forces between the probe and the sample's surface cause the cantilever to bend, or deflect. Many different forces, including van der Waals forces and Pauli repulsion, contribute to the net probe-sample force, and different forces dominate at different distances. This means the probe may experience either attractive or repulsive forces, depending on its height.

The deflection is measured by reflecting a laser from the back of the cantilever onto a four-quadrant photodiode. Any bending of the tip shifts the position of the laser spot on the photodiode, which leads to a change in the voltage it measures,  $V_{def}$ .

The sample rests on a stage, whose position relative to the tip

Figure 3.1: Diagram of an AFM setup, showing an AFM tip with a measured deflection, and a sample on a movable stage (not to scale).



<sup>1</sup> Depending on the specific instrument used, the actuators may move either the stage or tip.

<sup>2</sup> A PID is a control system that attempts to maintain an input variable (for example  $V_{def}$ ) at a specified value, or setpoint, by adjusting a second variable (for example tip height). It is so called because it makes corrections based on proportional, time-integrated and time-derivative terms to return to the setpoint quickly without inducing feedback oscillations.

can be adjusted with great precision by piezoelectric actuators.<sup>1</sup> A topography map is collected by monitoring  $V_{def}$ , and using a proportional, integral, derivative controller (PID)<sup>2</sup> to adjust the stage height to maintain a constant probe-sample separation. The stage can then be rastered laterally, and the adjustment needed to compensate for the varying sample height can be recorded as the topography image. The  $z$ -resolution of an AFM is usually sub-nanometre, meaning it can resolve steps as small as single atomic layers.

Most AFM techniques are based on one of two operation modes, which differ in how the PID responds to  $V_{def}$ :

*Contact mode* In which the probe is kept in permanent contact with the surface, so that the probe-sample force is always repulsive and an decrease in tip height leads to an increase in  $V_{def}$ . The PID works to maintain a constant *value* of  $V_{def}$ . This mode is simple in operation, but probe-sample forces are high, which means it may be unsuitable for delicate samples.

*Tapping mode* In which the tip is kept at a short distance from the sample (usually  $< 100$  nm) and an additional piezoelectric actuator is used to vibrate the cantilever close to its resonant frequency.  $V_{def}$  then becomes an oscillating signal, whose amplitude is damped by probe-sample forces when the tip moves closer to the sample. The PID works to maintain a constant *amplitude* of  $V_{def}$ . As this mode has little to no probe-sample contact, the forces exerted are much smaller, meaning sample damage is much less likely.

In modern AFMs, there are many more parameters which can be monitored to maintain a constant height, including the frequency or phase of an oscillating tip, or the peak force between tip and sample. However most of these modes are derived from the two presented above, which are sufficient to understand the AFM-derived techniques presented in the rest of this chapter.

### 3.1.1 Lock-in amplifiers

For many AFM-derived techniques, we need to isolate components with a known frequency and phase from a noisy signal. To achieve this, we use a lock-in amplifier [78].

These work by multiplying an input signal by a sinusoidal reference signal with frequency  $\omega_{ref}$  and phase  $\phi_{ref}$ . Equation 3.1 shows that this results in a DC offset for input signals of frequency  $\omega_{ref}$ , which is suppressed for all other frequencies.

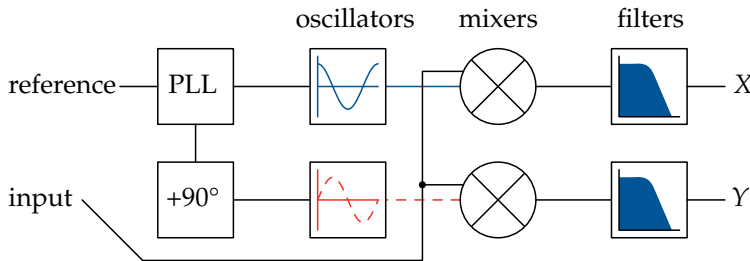
$$\int_{-\infty}^{\infty} \cos(\omega_{ref}t - \phi_{ref}) A \cos(\omega t - \phi) dt = \begin{cases} \frac{A}{2} \cos(\phi_{ref} - \phi), & \omega = \omega_{ref} \\ 0, & \omega \neq \omega_{ref} \end{cases} \quad (3.1)$$

Here  $t$  represents time, and  $A$ ,  $\omega$  and  $\phi$  represent the amplitude, frequency and phase of an arbitrary sinusoidal function.

In practice this multiplication can be achieved using frequency mixing circuits, then the DC offset can be recovered by low-pass filtering, a process called demodulation. To demodulate an input with an external oscillating reference signal, an internal reference oscillator is often synced to the external signal by a phase-locked loop (PLL).<sup>3</sup> In modern lock-ins, these steps are often performed digitally.

A two-phase lock-in exploits the phase sensitivity of the DC offset by demodulating the input at two orthogonal reference phases,  $\phi_{ref}$  and  $\phi_{ref} + 90^\circ$ . This returns both the in- and out-of-phase components at  $\omega_{ref}$ , referred to as  $X$  and  $Y$ . These can be converted to polar coordinates to yield the amplitude and phase difference between the input and reference signals.

Figure 3.2 shows a schematic of a two-phase lock-in amplifier.



<sup>3</sup> A circuit which tracks the phase, and therefore frequency, of a signal which may fluctuate in frequency or amplitude.

Figure 3.2: Lock-in amplifier operation principle. Two oscillators of orthogonal phase are synced to a reference signal by a PLL. These are multiplied by the input signal then low-pass filtered to yield the  $X$  and  $Y$  components at the reference frequency.

## 3.2 Scanning near-field optical microscopy

I showed above how AFM can be used to image the shape of samples at scales much smaller than the optical diffraction limit. But optical microscopy can be used to reveal much more about a sample than just its shape. SNOM combines AFM with laser illumination to beat the diffraction limit and bring the power of optical microscopy to the nanoscale [79].

<sup>4</sup>In practice, there are two kinds of SNOM, referred to as *aperture* and *scattering* SNOM. In this thesis I only use and discuss the scattering type.

<sup>5</sup>See section 1.1.4 for further detail on this.

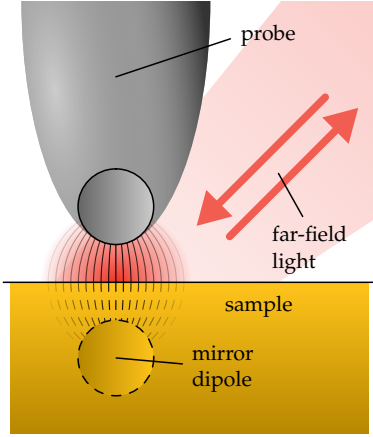


Figure 3.3: Near-field-sample interaction. Light is focused on an AFM probe, which excites a near field at its surface. The near-field interaction with a sample surface can be modelled by considering the end of the probe as a sphere, and considering its electrostatic interaction with a fictional mirror dipole.

### 3.2.1 Near-field interaction principle

The principle at the heart of SNOM is that a focused beam of light is shone onto a metallised AFM probe,<sup>4</sup> as shown in figure 3.3. This excites an evanescent near field at the metal surface, which is highly concentrated and decays exponentially with distance. This field is strongly enhanced by plasmonic resonances in the tip's metal surface,<sup>5</sup> and can be further enhanced still by the lightning rod effect, in which the length of the probe is aligned with the electric field polarisation of the incident light, so acts as an efficient antenna [79].

Crucially, the spatial extent of this field is typically much, much smaller than the wavelength of the incident light, meaning it can be used to image materials far below the diffraction limit. At the probe apex, the size of the near field is mainly governed by the probe's radius of curvature,  $r_p$ , meaning the technique has a comparable resolution to regular AFM. The imaging works because as the probe is brought close to a sample, the near field is modified when it interacts with the surface and scatters light back into the far field, which can then be detected along with the diffraction limited far field light [79].

A simple way to model this interaction, referred to as the point dipole model (PDM), is by assuming that the primary contribution to the scattering comes from the apex of the probe, which we can model as a sphere with radius  $r_p$ , dielectric function  $\epsilon_p$ , and polarisability

$$\alpha_p = 4\pi r_p^3 \frac{\epsilon_p - 1}{\epsilon_p + 2}. \quad (3.2)$$

We can also assume, thanks to the lightning rod effect, that this sphere can only be polarised in the  $z$  direction. An incident electric field,  $E_i$ , will induce a  $z$ -oriented dipole in the sphere, and we can simplify our model further by replacing our sphere with just a point dipole located at its centre.

If we then model the sample as a semi-infinite slab at  $z < 0$ , with dielectric function  $\epsilon_s$ , and electrostatic reflection coefficient

$$\beta_r = \frac{\epsilon_s - 1}{\epsilon_s + 1}, \quad (3.3)$$

(assuming the tip sits in vacuum) we can model the resultant near field caused by the tip-sample interaction as the electric field between the probe dipole discussed above and a mirror image dipole inside the sample with polarisability  $\alpha_p \beta_r$  [79]. This is shown in figure 3.3.

This leads to a system of electrostatic equations which when solved, yield an effective polarisability for the entire probe-sample near-field system,

$$\alpha_{eff} = \frac{\alpha_p (1 + \beta_r)}{1 - \frac{\alpha_p \beta_r}{16\pi(r_p+z)^3}}, \quad (3.4)$$

where  $z$  refers to the tip-sample separation [79].

For a point dipole, the scattered electric field,  $E_s$ , relates to the incident field and polarisability,  $\alpha$ , as

$$E_s \propto \alpha E_i, \quad (3.5)$$

which, when combined with equation 3.4, shows that the scattered light from SNOM contains a wealth of information about the dielectric properties of a material.

Since  $\epsilon$ ,  $\alpha$  and  $\beta_r$  are usually complex functions of light frequency  $\omega$ , it follows that  $E_s$  will also be a complex number given by

$$E_s = se^{i\phi}, \quad (3.6)$$

where  $s$  and  $\phi$  describe the amplitude and phase changes of the scattered light compared to the incident light. I discuss how we can perform phase-sensitive measurements in section 3.2.3

The PDM described above gives a simple, qualitative explanation of the contrast measured in SNOM experiments, but it fails to quantitatively reproduce features such as the measured spectral positions of polariton resonances [80]. For quantitative modelling, a more recent technique called the finite dipole model (FDM) is often used, which, instead of considering a point dipole in the apex of the spheroid, considers a dipole whose constituent positive and negative charges are located at opposite ends [80–82].<sup>6</sup>

The FDM can be extended to describe multilayered structures as well as semi-infinite substrates as discussed above [81]. This is important for 2d materials and heterostructures, which necessarily have finite thickness. To do this we must consider the effective Fresnel reflection coefficient for the uppermost surface of the structure. For a three-layer structure (a finite layer, sandwiched between a semi-infinite substrate and superstrate) this is given by

$$\beta_{ML}(k_{\parallel}) = \frac{\beta_{01} + \beta_{12}e^{-2k_{\parallel}d_1}}{1 + \beta_{01}\beta_{12}e^{-2k_{\parallel}d_1}}, \quad (3.7)$$

where  $k_{\parallel}$  is the in-plane component of the wavevector,<sup>7</sup>  $d_i$  is the thickness of the  $i^{\text{th}}$  layer, and

$$\beta_{ij} = \frac{\epsilon_j - \epsilon_i}{\epsilon_j + \epsilon_i} \quad (3.8)$$

is the reflection coefficient between layers  $i$  and  $j$ , with dielectric functions  $\epsilon_i$  and  $\epsilon_j$ .<sup>8</sup> For structures with a greater number of layers, equation 3.7 can be recursively substituted as an expression for  $\beta_{12}$  [82].

The semi-infinite PDM is sufficient to explain the operation of SNOM, and will be used for the rest of this chapter.

### 3.2.2 Distinguishing near-field and far-field light

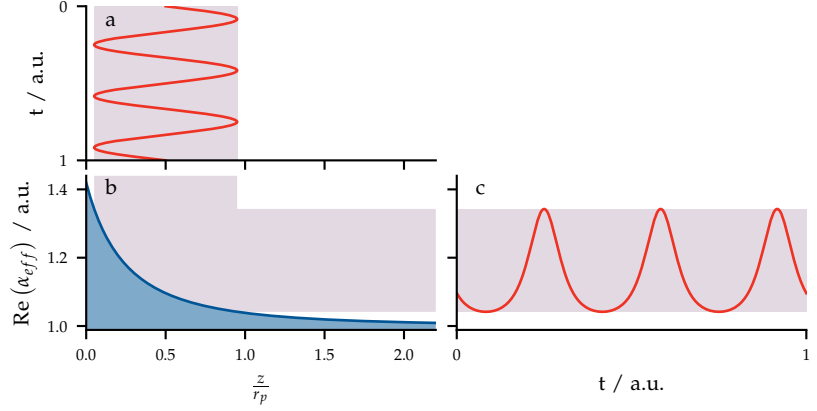
The backscattered light in a SNOM measurement is recorded using a high-speed sensor, typically a mercury cadmium telluride detector (MCT) for infrared (IR) SNOM. But one difficulty is that light scattered from the near field is typically only a tiny fraction of the total backscattered light. This means that the diffraction-limited far field swamps our desired signal, the near-field scattering from the AFM tip.

<sup>6</sup> The full description of the FDM is beyond the scope of this thesis. See reference [80] for the derivation and description of this model.

<sup>7</sup> As the FDM uses the quasi-static approximation, the  $k_{\parallel}$  dependence must be accounted for by integration over all  $k_{\parallel}$ , in combination with a coupling weight function [82].

<sup>8</sup> See section 1.1.3 for details on how to convert between conductivity and volumetric permittivity for graphene.

Figure 3.4: Origin of the high harmonics in the near field. **(a)** A sinusoidal oscillation of the probe height, interacts with **(b)** the non-linear  $z$ -dependence of  $\alpha_{eff}$ , leading to **(c)** a non-sinusoidal  $\alpha_{eff}$  signal. The dependence shown in (b) is calculated from equation 3.4, using  $\epsilon_p = -10 + 2i$ ,  $\epsilon_s = 15$  and  $r_p = 10$  nm.



To surmount this, the AFM in SNOM is typically operated in tapping mode, so that the near field is moved relative to the sample at a frequency  $\omega_0$ . This results in a modulation of the effective polarisability, and therefore the detected near-field signal. This can then be extracted from the total signal by using a lock-in amplifier to demodulate at  $\omega_0$ , using the tip's deflection as a reference signal.

However, even by demodulating at  $\omega_0$  there will still be some residual far-field signal left in the measurement, because of reflections from parts of the tip other than the probe apex. This can be attenuated further by relying on the non-linear  $z$ -dependence of the effective polarisability, which is shown in equation 3.4.

If we assume that the height modulation of the tip is sinusoidal, as shown in figure 3.4 (a), then we can expect any far-field reflections from the tip to also be primarily sinusoidal. But the nonlinear  $z$ -dependence shown in figure 3.4 (b), means that the time-dependent  $\alpha_{eff}$  signal will be periodic, but not sinusoidal, as shown in figure 3.4 (c). Equation 3.5 shows that the near-field component of the total signal measured will have this same waveform.

Like any periodic waveform, the scattered light can then be described by a Fourier series,

$$E_s = \sum_{n=0}^{\infty} s_n e^{i(n\omega_0 t - \phi_n)}, \quad (3.9)$$

where  $s_n$  and  $\phi_n$  are the amplitude and phase of the  $n^{\text{th}}$  harmonic of the fundamental mode at  $\omega_0$ , and the term at  $n = 0$  describes any direct current (DC) offset.

For a pure sinusoidal signal any term with  $n > 1$  will be zero, but any deviation from a pure sinusoid will add higher harmonics. This shows that if we demodulate at higher harmonics,  $n\omega_0$  instead of  $\omega_0$ , then the measured signal will have a greater proportion of the highly non-linear near-field signal [79].

The downside to high-harmonic demodulation is that the signal level is reduced, meaning a worse signal-to-noise ratio (SNR). In practice, it is common to use harmonics between 2 and 4 choosing the highest value that gives acceptable SNR.

### 3.2.3 Phase sensitive detection

There are several schemes for achieving phase sensitivity in SNOM measurements, most of which rely on Michelson interferometers like the one shown in figure 3.5. These can be used to selectively amplify a single phase, while suppressing others.

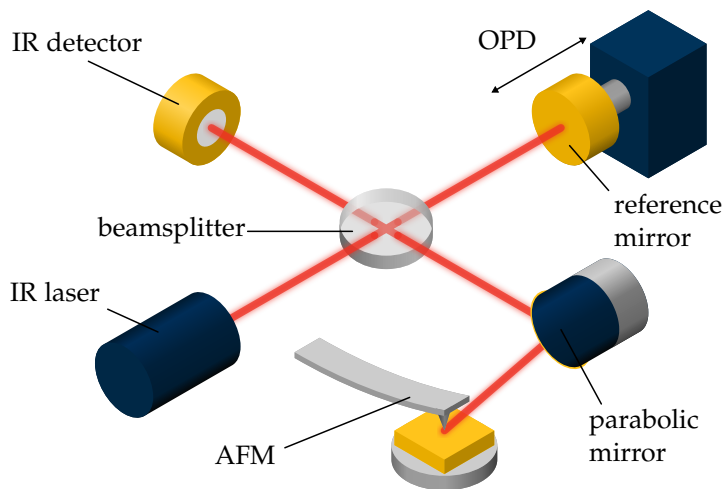
In a Michelson interferometer, a beamsplitter diverts the monochromatic laser beam along two paths, by reflecting a fraction of the light and transmitting the rest. One portion goes to the sample, where it is focused on the tip as shown in figure 3.5. Scattered light from the sample then travels back along the same path until it reaches the beamsplitter once more. The second portion goes through the reference arm of the interferometer, which ends in a flat reference mirror that also reflects the light back to the beamsplitter.

At the beamsplitter, a portion of both beams will be sent on to the detector, but as they have travelled different distances in the sample and reference arms, they may now have different phases. This causes either constructive or destructive interference, depending on their phase difference. The reference mirror can then be moved, which changes the optical path distance (OPD) between the two beams, and therefore the phase which is eventually detected. A linear change to the OPD<sup>9</sup> will result in a sinusoidal variation of the measured intensity as the beams move through constructive and destructive interference.

Typically in SNOM, we choose the phase of the near-field light scattered from a reference material, often a reflective metal like gold, as our reference phase, which we define to be zero. A complex SNOM scattering signal demodulated at the  $n^{\text{th}}$  harmonic can be described by

$$E_n = \text{Re}(E_n) + \text{Im}(E_n) i = s_n e^{i\phi_n}. \quad (3.10)$$

We can then measure the real, or in-phase, component by positioning our tip over the reference material and tuning the OPD to



<sup>9</sup>The change in the OPD is actually twice as large as the translation of the reference mirror, because the reference mirror affects both the reflected and incident path lengths together.

Figure 3.5: Michelson interferometer for phase-sensitive SNOM. The length of the reference arm can be changed by moving the reference mirror to amplify light of a single, chosen phase.

maximise the signal, meaning constructive interference. Similarly, we can measure the imaginary, or out-of-phase, component by changing the OPD from this position by  $\lambda/4$ , where  $\lambda$  is the wavelength of the light, which leads to destructive interference [79].

From these quantities we can then retrieve the  $n^{\text{th}}$ -harmonic amplitude and phase using the identities

$$s_n = \sqrt{\text{Re}(E_n)^2 + \text{Im}(E_n)^2} \quad (3.11)$$

and

$$\phi_n = \text{atan2}(\text{Im}(E_n), \text{Re}(E_n)). \quad (3.12)$$

There is a slight complication to the above picture, which is that there is typically a background added to  $E_n$  which results from the interference of the near-field scattered light with the far-field scattered light from the sample [83]. This light essentially adds in a third, uncontrolled beam path to the Michelson interferometer, which means that there is still some residual signal even with the OPD at  $\lambda/4$  away from the maximum. To remove this contribution, the reference arm can be completely blocked, leaving only the unwanted extra interferometric term, which can then be subtracted from the measured data.

Putting all of the above together, we can make a full complex near-field image by capturing three consecutive scans:<sup>10</sup> one with the OPD set to capture the real information, one with the OPD set to capture the imaginary information, and one with the reference arm blocked to capture the unwanted background.

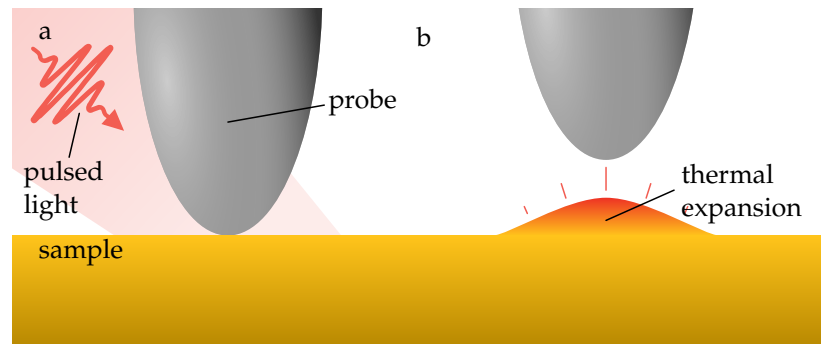
<sup>10</sup> A more efficient detection scheme exists which can reduce this to a single pass, by oscillating the reference mirror and using a lock-in amplifier, to capture amplitude and phase, and reject the unwanted background simultaneously [84]. However this is not possible on every microscope, and the three-pass technique was used in this thesis.

### 3.3 AFM infrared spectroscopy

Atomic force microscope infrared spectroscopy (AFM-IR) is a laser-coupled AFM technique that uses similar hardware to SNOM but operates on a different principle. It gives diffraction-beating measurements of IR absorption which are comparable to far-field Fourier transform infrared (FTIR) [85, 86].

In most AFM-IR modes a pulsed laser beam with light of frequency  $\omega$  is focused onto a sample immediately below an AFM tip in contact mode, as shown in figure 3.6 (a). If the sample has a

Figure 3.6: Principle of AFM-IR. (a) Pulsed light is focused on a sample beneath an AFM tip. (b) If the sample absorbs the light it heats up and expands, imparting an impulse to the tip proportional to the absorption.



vibrational mode that resonates at  $\omega$ , then it can absorb the light. The light energy is then converted to thermal energy in the sample, which leads to a thermal expansion.

This means that after every pulse of light the sample will expand below the AFM tip, giving it an upwards kick which can be detected in the AFM deflection signal, as shown in figure 3.6 (b). Crucially, the amplitude of this impulse is directly proportional to the magnitude of the absorption at  $\omega$ , which means it can be treated as a nanoscale analogue to other absorption techniques like FTIR [85, 86].

Different molecules have different vibrational resonances in the IR, which means absorption spectra can be used to distinguish different chemical species. In AFM-IR, a spectrum can be recorded by keeping the AFM tip in a fixed position and tuning the frequency of the excitation light, while measuring the amplitude of the impulses of the deflection signal. Alternatively an image can be captured, by keeping a fixed light frequency and making an AFM scan while monitoring the same signal. Together these can enable nanoscale chemical identification with a resolution of  $\sim 20$  nm, which is significantly lower than the diffraction limited FTIR [85, 86].

There are numerous ways to perform this technique, but the mode used in this thesis is called resonance enhanced AFM-IR. In this mode, a quantum cascade laser (QCL) excitation source is pulsed at a contact resonance frequency of the tip and sample,<sup>11</sup> which leads to a strong enhancement of the amplitude of the deflection signal [86].

In general, AFM-IR is not ideal for measuring van der Waals (vdW) materials, which tend to give very low signal levels because of their high thermal conductivity and low out-of-plane thermal expansion coefficients. However their absorption can be detected indirectly, if they are in thermal contact with a material which does give good AFM-IR signal such as (poly)methyl methacrylate (PMMA) [87]. The technique can also be useful to probe contaminants which may alter the behaviour of vdW materials [88].

<sup>11</sup> This is a resonance associated with the nanomechanical probe-sample interaction, which is typically different to the free-space cantilever resonance frequency.

### 3.4 Conclusions

In this chapter I have described some of the SPM-based techniques which I used to carry out the research in the later chapters of this thesis. I focused here on laser-coupled AFM techniques, however I hope that the examples discussed convey a sense of the versatility of SPM for characterising nanoscale material properties. In practice, there are many more such techniques than I could include in a single chapter, which can reveal a wealth of information on other nanomechanical [89], electronic [90] and optoelectronic [91] properties of 2d and vdW materials.

In the following chapter I will introduce a pair of common spectroscopic techniques, Raman and photoluminescence spectroscopy, which give complementary measurements to the AFM techniques described in this chapter.



## 4

# *Optical spectroscopy of van der Waals materials*

Optical spectroscopy techniques have proved to be valuable tools for characterising van der Waals (vdW) materials. In particular, Raman and photoluminescence (PL) spectroscopy are relied on heavily because they are non-destructive measurements which can reveal a wealth of information about the mechanical, electronic and optoelectronic properties of materials.

In this chapter I begin with a discussion of the physics that underpins Raman and PL, then I describe how we can implement the techniques practically to use in experiments. I finish with a detailed look at the Raman features of graphene, which will be referred to frequently in the rest of this thesis.

### *4.1 Light matter interaction for optical spectroscopy*

When light shines on a material, a photon with energy  $E_{ph}$  may interact with an electron. If there is an allowed electronic state at its starting energy plus  $E_{ph}$ , then the photon can be absorbed and the electron's energy will be raised.

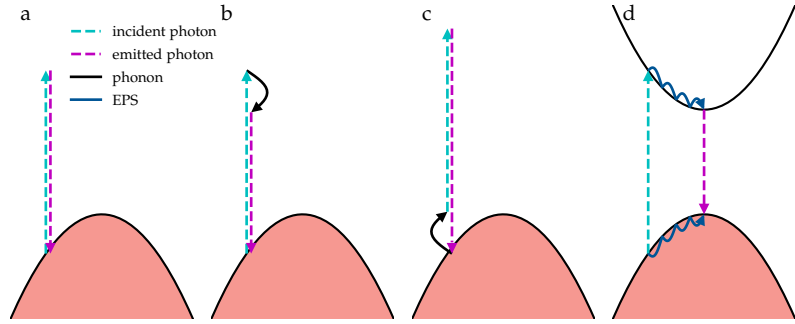
However often that state is forbidden, for example if it falls in the material's bandgap. In that case the photon can be virtually absorbed, and the electron put into a virtual excited state, which, as it is forbidden, must have a very short lifetime.

Typically this state then decays and the excess energy means another photon with energy  $E_{ph}$  is emitted. This process, depicted in figure 4.1 (a) is referred to as Rayleigh scattering and has limited spectroscopic use [92]. However it is a helpful concept from which to understand some of the more useful scattering processes, which I describe below.

#### *4.1.1 Raman scattering*

In the short time that an electron is in a virtual state, there is a finite probability that it may transfer some of its excess energy by creating an optical phonon of energy  $E_{\omega}$  in the material. This means that when the virtual state decays, the energy of the photon it emits will

Figure 4.1: Light-matter interaction processes for optical spectroscopy. **(a)** Rayleigh scattering: an electron is put into a virtual state by an incident photon, which decays by emitting another photon of the same energy. **(b)** Stokes scattering: an electron is put into a virtual state by an incident photon, loses energy by creating a phonon, then decays emitting a photon with lower energy. **(c)** Anti-Stokes scattering: an electron is put into a virtual state by an incident photon combined with a phonon in the material, which decays emitting a photon with a higher energy. **(d)** Photoluminescence: an electron is excited from the valence to the conduction band leaving a hole. These then relax to the band minimum and maximum via electron-phonon scattering (EPS) then recombine, emitting a photon with energy equal to the bandgap.



be slightly lower than the energy of the incident photon. The difference in energy between the two photons, referred to as the Stokes shift, will be equal to  $E_\omega$ .<sup>1</sup> This process, called Stokes scattering, is one of the two mechanisms for Raman scattering [93] and it is depicted in 4.1 (b).

By measuring the Stokes shift we can probe the spectrum of allowed phonons, which can be used as a signature to identify particular materials, but can also reveal information including a material's strain and electronic state [94].

The other Raman process is known as anti-Stokes scattering, which is depicted in 4.1 (c). In this process an electron is put into a virtual state by an incident photon combined with a phonon which already existed in the material, so the energy of the virtual state is  $E_{ph} + E_\omega$ . This decays by emitting a photon with a higher energy than the incident photon. This difference in energy is called the anti-Stokes shift and is once again equal to the energy of the involved phonon [93].

For spectroscopy, anti-Stokes Raman is generally more complicated than Stokes, because it depends on the spectrum of phonons which already exist in the material. This is typically determined by the lattice temperature and biased towards low energies, meaning anti-Stokes Raman can be used for nanoscale thermometry [95].

I discussed above the common case where the incident photon cannot excite an electron into an allowed state, so the electron is put into a short-lived virtual state. However Raman scattering can also occur with excitations to allowed states, for example in a transition between band edges. In this case, known as resonant Raman, the efficiency of the Raman process is significantly enhanced [92].

#### 4.1.2 Photoluminescence

In PL an incident photon has enough energy to excite a valence band electron in a semiconducting material to the conduction band, leaving behind a hole. These are then able to relax via electron-phonon scattering (EPS) processes, the electron to the conduction band minimum, and the hole to the valence band maximum. After this they can recombine, by the electron decaying across the bandgap to fill the hole, and releasing its excess energy in the form of a photon with the same energy as the bandgap,  $E_g$  [93]. This process is shown

<sup>1</sup>For historical reasons, there is some confusion between the units and the symbol used for phonon energies and Raman shifts. We normally describe these in terms of their associated wavenumber, in units of  $\text{cm}^{-1}$ , but we use the symbol  $\omega$ , which is more typically used for angular frequency, which has units of  $\text{rad s}^{-1}$ . In this thesis I shall stick to this convention for consistency with existing literature.

in figure 4.1 (d).

The efficiency of PL is substantially reduced if the material has an indirect bandgap, that is, if the conduction band minimum is not directly over the valence band maximum. This is because after relaxing via EPS, there will still be a momentum mismatch between the electron and hole which would need to be overcome for them to recombine.

In some cases, the excitation may form a quasiparticle called an exciton, a Coulombically bound electron-hole pair [96]. In this case, the large number of electrons surrounding the hole somewhat screen its positive charge, meaning the electron is less attracted to the hole and consequently, the bound electron and hole have a lower energy than if they were unbound. This difference in energy is called the exciton binding energy,  $E_b$ , and when the electron and hole recombine, they emit light of energy  $E_g - E_b$ .

There are typically multiple simultaneous processes involved in a PL measurement, which can involve bandgap recombination as well as recombination of multiple different excitonic species, all of which may have different characteristic energies.

#### 4.2 Optical spectroscopy in practice

Raman and PL operate on quite different physical principles, but to collect Raman and PL spectra, the measurement approach is essentially the same. In both cases, the goal is to introduce light of one energy to our sample, then inspect the different energies of light that are scattered back. Figure 4.2 shows experimental apparatus that can achieve this for both Raman and PL.

In this setup, monochromatic light from a laser is focused onto the surface of a sample through a microscope objective. This interacts with the materials in the sample via the processes described above, meaning a spectrum of light composed of different energies is scattered back along the same path as the incident light.

A beamsplitter then directs some of this light through a notch filter towards the detection apparatus. The purpose of the notch filter is

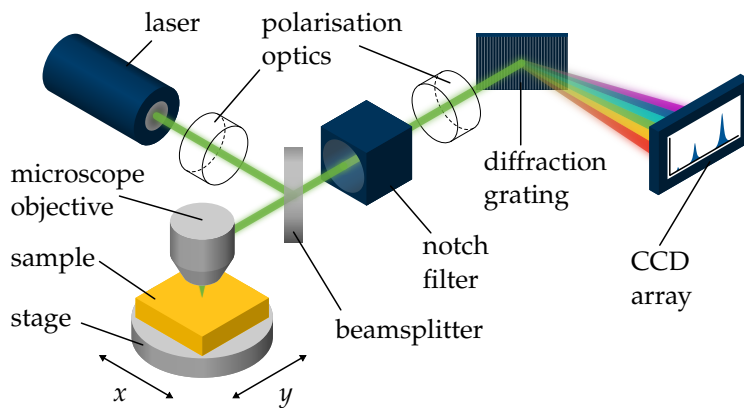


Figure 4.2: Optical spectroscopy apparatus schematic. This could be used for both Raman and PL. The polarisation optics are variable and can be removed entirely.

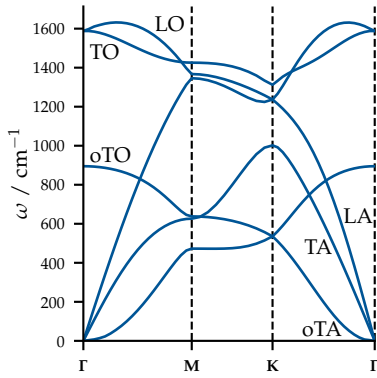


Figure 4.3: Graphene ab-initio-calculated phonon dispersions. Labels are assigned to each phonon branch according to reference [93]. Dispersion data was taken from reference [97].

<sup>2</sup> In fact, it's common to have unwanted contributions from PL in a Raman experiment and vice versa. Figure A.3 is a chart which converts between the different units used for Raman and PL to help identify spectroscopic features in such cases.

<sup>3</sup> The 2D peak is named because it is the overtone of the D peak. In this thesis I distinguish between two-dimensional (2d) and the Raman peak (2D) by using a lowercase and capital D.

<sup>4</sup> See figure 1.2 for the locations of these points.

<sup>5</sup> To refer to these phonons I will combine the abbreviations given here in brackets, for example LA for longitudinal acoustic, or oTO for out-of-plane transverse optical.

to remove the Rayleigh scattered light at the laser frequency, which is typically much more intense than the contribution from Raman scattering and PL and would otherwise saturate the detector.

The final stage is a spectrometer, which consists of a dispersive element, to separate out the different frequencies of light, and a detector array, to record the light intensity at each frequency. Here this is represented by a diffraction grating and a charge-coupled device (CCD).

A movable stage, combined with a high-resolution microscope objective means that hyperspectral datacubes can be collected, by rastering the stage so that a grid of spectra can be taken from a target area. To extract useful information from these large datasets, it is common to fit Lorentzian or Gaussian peaks to the spectral features.

The apparatus can also be augmented with the addition of polarisation optics, which can enable polarisation dependent Raman and PL measurements.

In practice the only difference between a Raman and PL experiment is the range of energies studied, which can be adjusted by changing the density of lines or angle of the diffraction grating.<sup>2</sup> As phonon energies are typically in the mid-infrared (IR), and therefore much lower than the visible laser energy, Raman peaks are usually quite close to the laser energy, compared to PL peaks.

### 4.3 The Raman spectrum of graphene

Raman spectroscopy is especially powerful for characterising graphene. By inspecting the Raman spectrum we can reveal details including the number of layers, defect density, strain and doping [92]. But as graphene has relatively few Raman features, its analysis can be complicated.

In this section I will discuss the origin and behaviour of the most important components of the graphene Raman spectrum, the G, D and 2D peaks.<sup>3</sup>

#### 4.3.1 Graphene phonon dispersion

To understand the graphene Raman spectrum, it is first helpful to study the dispersion of allowed phonons. This is shown between high-symmetry points in the Brillouin zone (BZ)<sup>4</sup> in figure 4.3.

Graphene has three acoustic (A) and three optical (O) phonon branches, and it is only the optical phonons which play a part in Raman scattering. Additionally two of these branches are out-of-plane transverse (oT) modes, which are much softer than the in-plane longitudinal (L) and transverse (T) modes [92, 93].<sup>5</sup>

First-order Raman processes, which involve only a single phonon, must arise from phonons at the  $\Gamma$  point at the centre of the BZ, which have no associated momentum transfer. This is known as the fundamental Raman selection rule, which stems from momentum conservation [93].

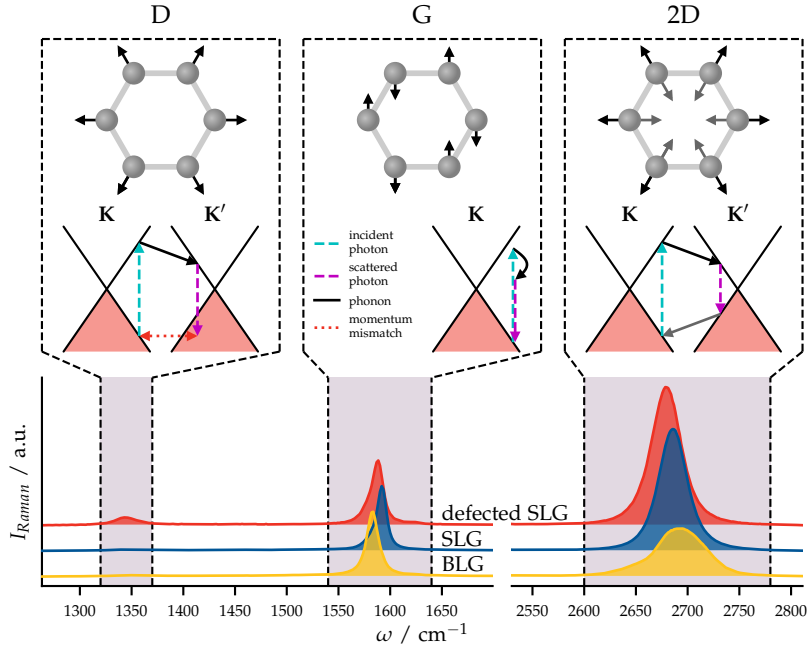


Figure 4.4: The Raman peaks of graphene. Bottom: Example Raman spectra from defected and pristine SLG, and BLG, normalised to the height of the G peak. Top: Annotations showing the real- and  $k$ -space processes that result in the D, G and 2D peaks. Note: the spectra shown are averages from a small area, so are slightly broadened.

#### 4.3.2 Origin of the graphene Raman peaks

Figure 4.4 shows the Raman spectra from single layer graphene (SLG), defected SLG and bilayer graphene (BLG). The most important graphene Raman peaks are the D, G and 2D peaks. These have been highlighted and linked to boxes which show the associated real-space atom displacements for a single unit cell (top), and the  $k$ -space electronic transitions relative to the  $\mathbf{K}$ -point band structure (bottom).

I discuss the physical origin of each peak below:

*The G peak* This peak at  $\sim 1580 \text{ cm}^{-1}$  stems from the degenerate TO and LO phonons at the  $\Gamma$  point, which can be labelled  $E_{2g}$  according to group theory nomenclature [92, 93]. The central box in figure 4.4 shows the real- and  $k$ -space processes associated with the G peak [92].

As the G peak arises from a  $\Gamma$ -point phonon, there is no associated momentum transfer, so the excited electron relaxes back to the same point in  $k$ -space. This means the G peak comes from a first-order Raman process involving a single phonon.

*The D peak* This peak at  $\sim 1345 \text{ cm}^{-1}$  stems from the TO phonon at the  $\mathbf{K}$  point [92, 93]. The leftmost box in figure 4.4 shows the real- and  $k$ -space processes associated with the D peak [92].

As the D peak arises from a  $\mathbf{K}$ -point phonon, there is a momentum mismatch between the initial and final states, shown by a red double-headed arrow. As  $\mathbf{K} + \mathbf{K} = \mathbf{K}'$ , we can call this an intravalley process. The fundamental Raman selection rule therefore forbids this process for graphene, unless there is some external factor which provides the necessary momentum to satisfy conservation.

Scattering from lattice defects serves this function, which means that the D peak is absent in pristine graphene but activated for defected graphene. The height of the D peak is therefore a reliable indicator of the defect density in graphene [92, 93]. As an example, in the spectra at the bottom of figure 4.4 only the defected graphene shows a significant D peak.

*The 2D peak* This peak at  $\sim 2790 \text{ cm}^{-1}$  also stems from the TO phonon at the  $\mathbf{K}$  point, but it is activated via a different route than the D peak [92, 93]. The rightmost box in figure 4.4 shows the real- and  $k$ -space processes associated with the 2D peak [92].

Like the D peak, this is a finite-momentum, intravalley process. However in this case, the momentum conservation is satisfied by the creation of a second phonon, which has the same energy and magnitude of momentum but is opposite in direction. As this process involves two phonons it is a second-order Raman process, sometimes called a double-resonance process. The virtual excited state loses the energy of the TO phonon two times, so the corresponding Raman shift is therefore twice that of the D peak.

The double-resonance process satisfies the fundamental Raman selection rule with no need for defect scattering. So unlike the D peak, the 2D peak is present in both defected and pristine graphene.

#### 4.4 Characterising graphene with Raman spectroscopy

In this section I will discuss the effects of various factors on the Raman spectrum of graphene, and how they can be exploited for characterisation. I will use the symbols  $I_p$ ,  $\omega_p$  and  $\Gamma_p$  to represent the height, Raman shift and full width at half maximum (FWHM) of a peak, where  $p$  is a stand in for the peak in question.

##### 4.4.1 Number of layers

One of the most useful features of Raman spectroscopy for graphene is the ability to identify the number of layers in a sample.

The height ratio between the 2D and G peaks,  $I_{2D}/I_G$ , and the FWHM of the 2D peak,  $\Gamma_{2D}$ , are typical quantities used to probe this. A hallmark of SLG is a symmetrical 2D peak with  $\Gamma_{2D} \sim 30 \text{ cm}^{-1}$  and  $I_{2D}/I_G \gtrsim 2$ . By comparison the 2D peak of Bernal-stacked BLG is shorter and broader with  $\Gamma_{2D} \sim 50 \text{ cm}^{-1}$  and  $I_{2D}/I_G \sim 1$  [98, 99], as shown in figure 4.4. However, these values can depend significantly on the substrate under the graphene [100, 101]. For SLG the 2D peak can be fit best by a single Lorentzian, while for BLG the best fit is found from a sum of four Lorentzians [98, 99].

For twisted bilayer graphene (TBLG) there is a complicated dependence of the Raman spectra on the twist angle between the layers, caused by the addition of a moiré superlattice [102–105].<sup>6</sup>

<sup>6</sup> See section 1.2.2 for more detail on TBLG.

#### 4.4.2 Strain

The phonon frequencies in a material are sensitive to the lattice constant, which means that they change when the material is strained. Raman spectroscopy can therefore be used to probe strains, via the shifting positions of the corresponding Raman peaks.

As shown in equation 1.8 of chapter 1, strains in graphene can be described by the biaxial strain tensor,

$$\varepsilon_{bi} = \begin{pmatrix} \varepsilon_{xx} & \varepsilon_{xy} \\ \varepsilon_{yx} & \varepsilon_{yy} \end{pmatrix} \quad (\text{where } \varepsilon_{xy} = \varepsilon_{yx}). \quad (4.1)$$

To discuss the effects of strain on graphene's Raman spectrum, it is helpful to split this further into two components. The first of these is the hydrostatic strain,

$$\varepsilon_{hs} = \varepsilon_{xx} + \varepsilon_{yy}, \quad (4.2)$$

which relates to the change in area of a unit cell, and is independent of any distortion in the shape. The second component is shear strain,

$$\varepsilon_s = \sqrt{(\varepsilon_{xx} - \varepsilon_{yy})^2 + 4\varepsilon_{xy}^2}, \quad (4.3)$$

which describes an anisotropic deformation to the lattice, and is independent of any change in the area.

The shift in the frequency of a phonon or Raman peak with strain can be quantified by a Grüneisen parameter [106–108],

$$\gamma = -\frac{1}{\omega} \frac{\partial \omega}{\partial \varepsilon_{hs}}. \quad (4.4)$$

This may also be defined relative to a uniaxial strain in one direction, for example  $\varepsilon_{xx}$ , however the value of  $\gamma$  will then depend on the orientation of the applied strain to the lattice [106, 108].

The shifting of the G and 2D peaks with strain is illustrated in figure 4.5.

On top of the  $\varepsilon_{hs}$ -dependent shifting of phonon frequencies, there is also a  $\varepsilon_s$ -dependent splitting of the phonons about their centre frequency, which arises from an anisotropic lattice constant. This can be quantified for a particular phonon or Raman peak using the shear deformation potential,

$$\beta = \pm \frac{1}{2\omega} \frac{\partial \omega}{\partial \varepsilon_s}. \quad (4.5)$$

This peak splitting has been observed for both G and 2D peaks in graphene [106, 108–112].

As the splitting arises due to anisotropy, the phonon vibrations corresponding to each component must have different orientations. This means that linearly polarised input light may bias the detected Raman signal towards either the upshifted or downshifted peak, depending on the orientation of the  $E$ -field to the vibration and lattice. Polarisation dependent Raman can therefore be used to determine the crystallographic orientation of strained graphene [108, 109, 113].

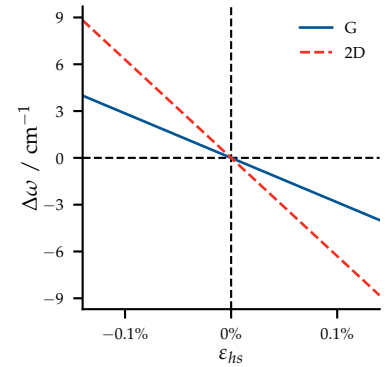


Figure 4.5: Strain-dependent G and 2D peak shifts. Calculated according to reference [108], using a G-peak Grüneisen parameter of  $\gamma_G = 1.8$ , an unstrained G-peak position of  $\omega_G = 1583 \text{ cm}^{-1}$  and  $\Delta\omega_{2D}/\Delta\omega_G = 2.21$ .

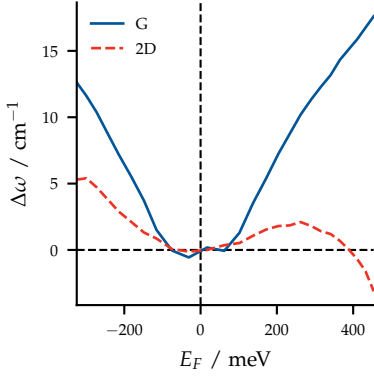


Figure 4.6: Doping-dependent G and 2D peak shifts. Acquired from field effect transistor (FET) measurements in reference [114]. Data used with the kind permission of Guillaume Froehlicher and Stéphane Berciaud.

<sup>7</sup> The  $k$ -space surface dividing allowed states below the Fermi level from forbidden states.

<sup>8</sup> See section 1.1.3 for more detail on Pauli blocking.

Alternatively if this polarisation dependence is unwanted, it can be removed by adding a quarter-wave plate to the incident beam path to induce circular polarisation [94, 108].

#### 4.4.3 Doping

Electron-phonon interactions mean that the frequencies of Raman peaks also depend on the level of doping in a material [93].

In graphene this behaviour is strongly influenced by the presence of Kohn anomalies at the  $\Gamma$  and  $\mathbf{K}$  points [92, 115, 116], which can be seen in figure 4.3. Kohn anomalies are sharp kinks in the phonon dispersion for particular wavevectors, which are caused by an abrupt reduction in the screening of lattice vibrations by electrons. The wavevectors at which these occur are those that connect points on the Fermi surface,<sup>7</sup> which means that they can be altered by changing the Fermi level [92].

The positions of graphene's G and 2D peaks can therefore be effectively controlled by doping via the electric field effect [12, 114, 116–118]. The Fermi level dependence of this shifting is illustrated in figure 4.6.

On top of its change in frequency, the intensity of the G peak can be also increased by doping thanks to Pauli blocking,<sup>8</sup> which prevents certain electronic transitions taking place [92].

### 4.5 Conclusions

In this chapter I showed how optical spectroscopy with visible excitation, particularly Raman and PL, is a versatile characterisation method that can reveal information on the electronic state, strain, and crystal structure. By combining spectroscopy with the scanning probe microscopy (SPM) techniques introduced in the previous chapter, we have a powerful suite of tools for studying the nanoscale properties of two-dimensional (2d) materials.

This concludes part II, which described the measurement techniques I used to characterise the 2d and vdW materials studied in this thesis. In part III, I will present a series of chapters based on my own original research which build upon the topics introduced in parts I and II.

## **Part III**

# **Original research**



## 5

# *Imaging of graphene's strain and doping with Raman vector analysis*

In this chapter, I present my research based on a scheme of Raman vector analysis, which allows simultaneous quantitative measurements of strain and doping in graphene. I combined the existing method with high resolution Raman mapping and demonstrated its diagnostic power by imaging two graphene-hexagonal boron nitride (hBN) heterostructures. I was able to show that the scatter of Raman peaks around their centre frequency, which has been reported in previous works, is actually an emergent property of nanoscale features which strain and dope the graphene, including fractures, folds, bubbles and wrinkles.

This is one of the first pieces of work I completed during my PhD and it informed the direction of much of my following research. Later chapters on the effects of strains caused by nanoscale features in two-dimensional (2d) materials are a logical continuation of the work started here. Much of the work in this chapter was published in the paper *Probing the nanoscale origin of strain and doping in graphene-hBN heterostructures* in the journal *2D Materials* (see [Dissemination](#)).

I'm particularly grateful to Eli Castañón and Vish Panchal for fabricating the samples studied in this chapter, to Stephen Power and Antti-Pekka Jauho for fitting our results to their simulations of strained graphene, and also to Guillaume Froehlicher and Stéphane Berciaud for allowing me to use their data in this thesis.

### *5.1 Distinguishing strain and doping with Raman vector decomposition analysis*

To make functional graphene nanodevices feasible, it is important to understand the nanoscale strain and doping variations in real-world graphene samples. Many fabrication processes, such as deposition on a substrate [119, 120], assembly into van der Waals (vdW) heterostructures [121] and thermal annealing [122], are known to induce graphene strain variations. These can alter carrier mobility [119], band structure [110] and optoelectronic properties [123].

The sensitivity of graphene's physical properties to strain opens up the possibility of using deliberately induced strain as a method of

controlling various parameters in graphene devices [13, 124]. For example, it has been shown that non-uniform strain can induce strong pseudomagnetic fields (PMFs) greater than 300 T [20], which may in turn provide a platform to manipulate the sublattice [17, 125, 126] and valley [126, 127] degrees of freedom.<sup>1</sup>

<sup>1</sup> See section 1.1.2 for more detail on strain effects in graphene.

In section 4.4, I showed how both strain and doping induce a frequency shift to single layer graphene (SLG)'s G and 2D Raman peaks, which suggests that Raman spectroscopy can be a useful tool to measure both quantities. But in practice this is complicated by the fact that strain and doping variations typically coexist in the same sample. This means that peak shifts from both strain and doping will be present simultaneously, so the contribution from either one is difficult to determine.

To separate these contributions we can use a vector decomposition analysis scheme, which was first proposed by Lee et al. in 2012 [128]. The principle behind this scheme is shown in figure 5.1, which shows the expected shifts of the G and 2D peaks, induced in charge neutral, unstrained SLG by changing its strain,  $\varepsilon$ , or doping,  $n$ .<sup>2</sup>

<sup>2</sup> This shows the same trends represented in figures 4.5 and 4.6, but  $\Delta\omega_G$  and  $\Delta\omega_{2D}$  are shown in relation to each other, rather than as functions of strain or doping.

The key relation shown by this figure is that, for both strain and p-type doping, the G and 2D shifts are approximately proportional, so the displacement in the  $\Delta\omega_G$ - $\Delta\omega_{2D}$  space approximates a straight line with an associated gradient.

This means we can define a pair of unit vectors

$$\hat{\varepsilon} = \begin{pmatrix} \hat{\varepsilon}_G \\ \hat{\varepsilon}_{2D} \end{pmatrix}, \quad \hat{n} = \begin{pmatrix} \hat{n}_G \\ \hat{n}_{2D} \end{pmatrix}, \quad (5.1)$$

which have the same gradients as the strain and doping induced peak shifts. We can then transform our peak shifts into the basis defined by these unit vectors as

$$\begin{pmatrix} \hat{\varepsilon}_G & \hat{n}_G \\ \hat{\varepsilon}_{2D} & \hat{n}_{2D} \end{pmatrix}^{-1} \begin{pmatrix} \Delta\omega_G \\ \Delta\omega_{2D} \end{pmatrix} = \begin{pmatrix} v_\varepsilon \\ v_n \end{pmatrix}, \quad (5.2)$$

where  $v_\varepsilon$  and  $v_n$  relate to the proportion of the peak shift due to strain or doping. Then finally the components of the peak shifts due solely to strain and solely to doping can be recovered according to

$$\begin{pmatrix} \Delta\omega_G \\ \Delta\omega_{2D} \end{pmatrix}_\varepsilon = v_\varepsilon \hat{\varepsilon}, \quad \begin{pmatrix} \Delta\omega_G \\ \Delta\omega_{2D} \end{pmatrix}_n = v_n \hat{n}. \quad (5.3)$$

Once the separated peak shifts have been obtained, it is simple to convert from peak shift to strain by using a Grünesen parameter, as described in equation 4.4. In this thesis I use the G peak Grünesen parameter  $\gamma_G = 1.8$ . I also use a value of 2.21 for the gradient associated to strain changes. Both of these are valid for pure hydrostatic strain,  $\varepsilon_{hs}$  [108].

Likewise, we can convert peak shift to doping using an empirical reference function. I use the relation

$$E_F = - \left( 1.8 \times 10^{-2} \text{ eV cm} \right) \Delta\omega_G - \left( 8.3 \times 10^{-2} \text{ eV} \right), \quad (5.4)$$

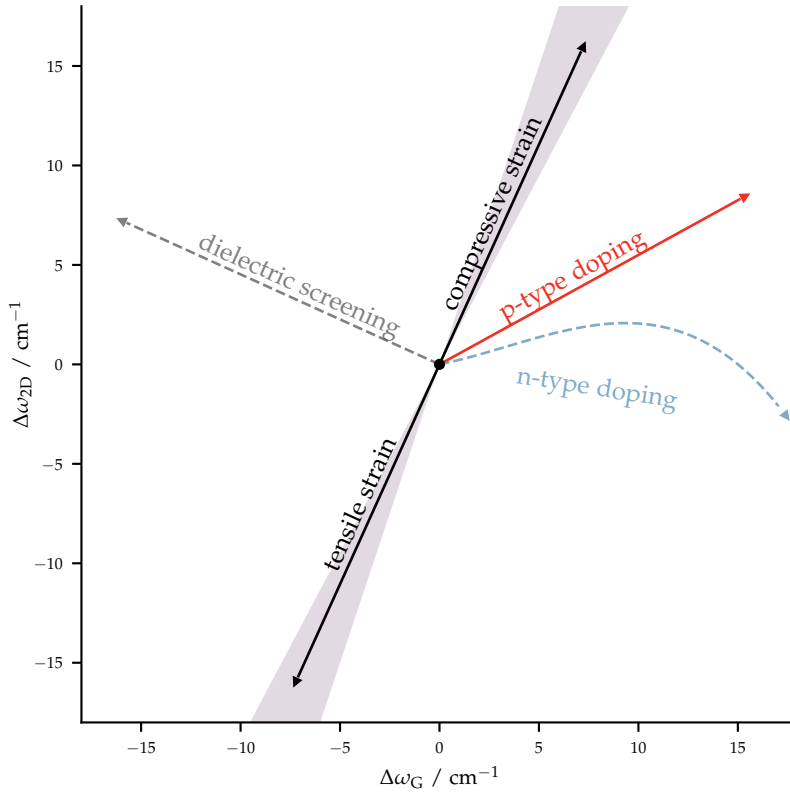


Figure 5.1: Strain and doping induced peak shifting. The black arrows show the gradient associated with pure hydrostatic strain, and the grey region represents the range of gradients realised for different types of strain. The red arrow shows the gradient for p-type doping [108]. The dashed lines for dielectric screening and n-type doping are approximate and based on references [101, 114]. They are not included in the vector decomposition analysis.

which is calibrated from field effect transistor (FET) measurements and valid for hole doped SLG [114]. This can be further converted to hole concentration,  $n_h$ , using equation 1.5. I use a gradient of 0.55 for changes due to doping [108].

The full quantitative vector analysis scheme is shown in figure 5.2. From this we can gain a more intuitive visual understanding of the process.

The vector decomposition can be thought of as superimposing a new pair of axes onto our  $\Delta\omega_G$ - $\Delta\omega_{2D}$  space, which are parallel to  $\hat{e}$  and  $\hat{n}$ . The scaling on these axes is defined by the Grüneisen parameter and equation 5.4. Then for an arbitrary peak shift,  $(\Delta\omega_G, \Delta\omega_{2D})$ , from unstrained, charge-neutral graphene, at  $\Delta\omega_G = \Delta\omega_{2D} = 0$ , we can read the value of strain or doping from the corresponding axis.

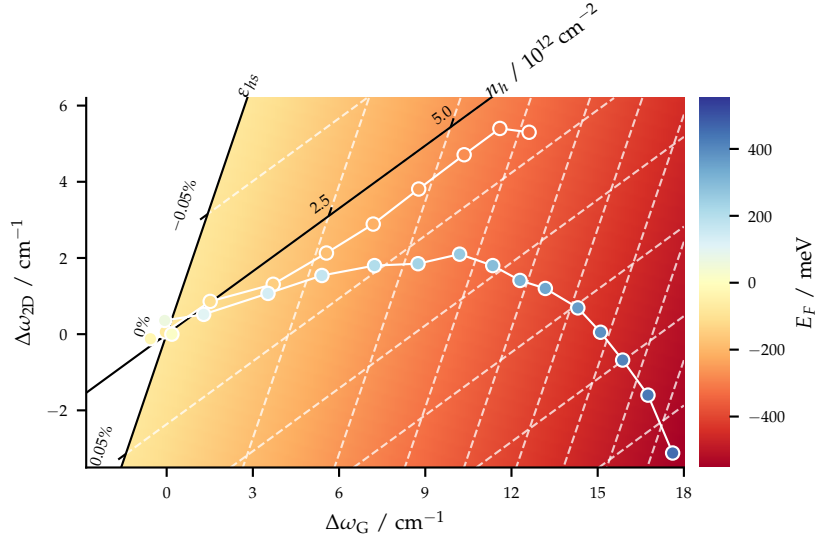
### 5.1.1 Important considerations for strain-doping decomposition

This analysis is powerful tool which has been used to characterise a wide range of graphene samples [101, 108, 128–133], but, as the model relies on a certain set of assumptions, care must be taken in how it is applied.

The primary consideration, which has been mentioned above, is that the model is only applicable to p-type graphene. To show why this is the case, a set of measurements of peak positions from a graphene FET have been added to figure 5.2, using data from reference [114].<sup>3</sup> These measurements include both p-type and n-type

<sup>3</sup> This is the same data that is shown in figure 4.6.

Figure 5.2: Strain-doping decomposition. Vector decomposition is shown as a pair of superimposed axes defining a new basis, from which hole doping and hydrostatic strain can be read. FET measurements of peak positions from reference [114] are added as points connected with solid white lines, and coloured to show the corresponding Fermi level. Agreement with the vector decomposition is good for p-type graphene but fails for n-type. Data used with the kind permission of Guillaume Froehlicher and Stéphane Berciaud.



graphene (coloured red and blue according to their  $E_F$ ), which shows that for n-type graphene the direction of the G peak shift reverses and the trajectory in  $\Delta\omega_G$ - $\Delta\omega_{2D}$  space becomes non-linear. This makes linear vector decomposition impossible for electron-doped graphene. Fortunately we can usually assume that exposed graphene in ambient conditions is primarily hole doped, as shown by a range of charge transport and Raman measurements [114, 118, 134].

We must also ensure that our graphene is relatively free from defects, as an increase in defect density has also been shown to induce peak shifts [92, 128].

Another consideration is the configuration of the strain that we measure. Biaxial and uniaxial strains lead to different values measured for the gradient of  $\hat{\epsilon}$ , which also varies with the orientation of uniaxial strain to the lattice [106–108, 111, 128, 135, 136]. The range of different gradients is shown by the grey area in figure 5.1. If the gradient of  $\hat{\epsilon}$  is chosen poorly, such that it doesn't match the dominant species of strain, it can lead to large errors in the measured doping.

To remove this ambiguity, I use a refinement to the vector decomposition scheme which was proposed by Mueller et al. in 2017 [108].<sup>4</sup> Circularly polarised excitation light is used to minimise the difference in intensity between any split peaks induced by shear strain. Without this, more uniaxial strains would lead to an asymmetry in the lineshape, which would bias the values of peak position returned by fitting single peaks to the data. This means it is possible to separate the effects of hydrostatic strain, which induces a peak shift, and shear strain, which induces a symmetric splitting or broadening. The gradient associated with pure hydrostatic strain can then be used for any graphene sample, regardless of its strain configuration.

A final consideration with this analysis concerns the frequency of the point at  $\Delta\omega_G = \Delta\omega_{2D} = 0$ . Without knowing the actual values of  $\omega_G$  and  $\omega_{2D}$  at this nominally unstrained, undoped point, only

<sup>4</sup>The discussion of strain effects on graphene's Raman peaks in section 4.4.2 may be helpful to understand this refinement.

relative shifts in strain and doping can be determined.

For graphene on  $\text{SiO}_2$  with an excitation wavelength of  $\lambda = 532 \text{ nm}$ , this has been determined as  $(\omega_G, \omega_{2D}) = (1583, 2678) \text{ cm}^{-1}$  [108]. However this position will change with different laser wavelengths, as both G and 2D peaks are strongly dispersive [92].<sup>5</sup>

The position can also move somewhat for graphene in different environments and on different substrates thanks to dielectric screening, which can add a small unquantified offset [101, 137]. This is illustrated with a dashed arrow in figure 5.1.

<sup>5</sup>This is due to the Kohn anomalies discussed in section 4.4.3, and means their Raman shift depends on the energy of the excitation photons.

## 5.2 Identifying nanoscale structural features in graphene-hBN heterostructures

In the rest of this chapter, I show results from applying the method described above to study two graphene-hBN heterostructures:

*Heterostructure A* A SLG sample on  $\text{SiO}_2$  which is partially covered by a flake of multilayer hBN, and features a range of interesting nanoscale defects.

*Heterostructure B* An hBN-encapsulated SLG sample, where inter-layer contamination has led to the formation of bubbles during fabrication.

### 5.2.1 Heterostructure A: exposed and hBN-capped graphene

Heterostructure A is shown in the optical image in figure 5.3. It consists of a sheet of SLG,  $\sim 70 \mu\text{m}$  in size, partially covered by exfoliated hBN of  $\sim 20 \text{ nm}$  in thickness and with lateral dimensions of  $\sim 50 \times 30 \mu\text{m}$ .

The AFM scans shown in figure 5.4 reveal one-dimensional (1d) features on both the graphene and the hBN-covered graphene. These

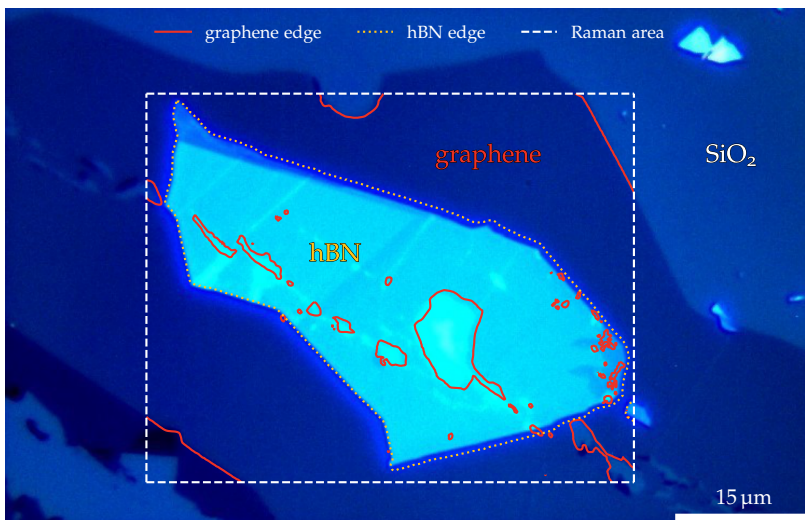


Figure 5.3: Heterostructure A optical image. Outlines showing the graphene and hBN edges are determined from the heights of the graphene 2D peak and hBN peak, shown in figure 5.6. The graphene has several holes in it beneath the hBN. The white dashed rectangle shows the area of the atomic force microscopy (AFM) and Raman scans in the rest of section 5.2.1.

Figure 5.4: Heterostructure A AFM images. (a) A scan of the entire heterostructure. The white dotted square shows the location of the scan in (b). (b) A higher resolution scan of the region indicated in (a) showing a crack and a fold. The white arrows show the location and thickness of the line profiles shown in figure 5.5.

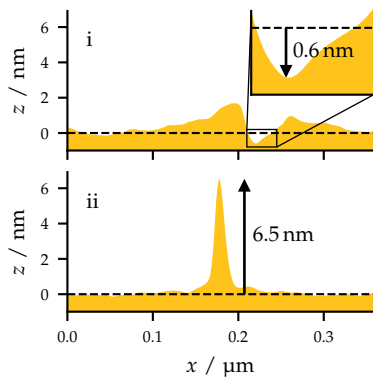
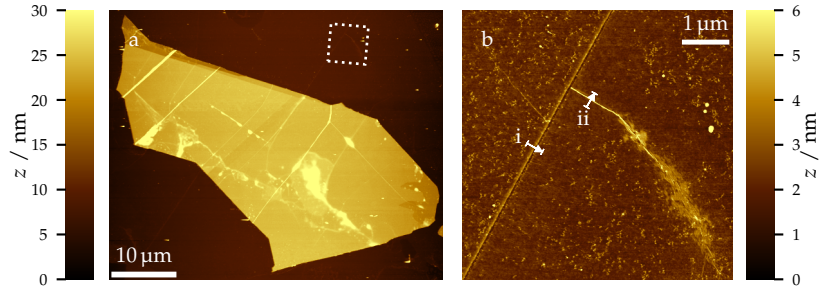


Figure 5.5: Line profiles taken across a fracture and a fold. (i) Line profile across a fracture. Inset image is a zoomed in region to better show the depth. (ii) Line profile across a fold. The locations of (i) and (ii) are indicated in figure 5.4 (b).

<sup>6</sup>The hBN peak is very close in frequency to the D peak, so these peaks were fitted together. To prevent crosstalk between the fits to each peak, the frequencies were held fixed at 1343.2 and 1366.8  $\text{cm}^{-1}$ .

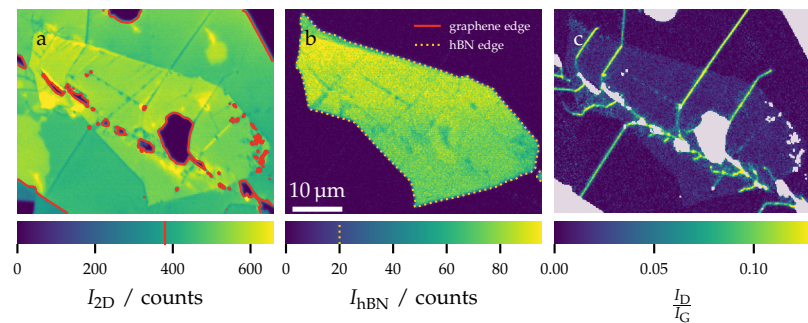
appear to be a mixture of small fractures and folds, which most likely occurred during the exfoliation or stacking of the heterostructure materials. Figure 5.4 (b) shows a close-up of a fracture and a fold, taken from the area indicated in figure 5.4 (a). Whereas the fracture has homogeneous width along the whole length, the fold starts tightly compacted where it contacts the fracture but spreads out as it gets further away.

Detailed line profiles taken from the features in figure 5.4 (b) are plotted in figure 5.5. The bottom of the fracture in figure 5.5 (i) is  $\sim 0.6$  nm lower than the average level of the graphene. This is consistent with AFM measurements of the thickness of monolayer graphene prepared in ambient conditions.

A Raman datacube was collected from the heterostructure, and single Lorentzians were fitted to the graphene 2D, G and D peaks, as well as the characteristic hBN peak at  $\sim 1367$   $\text{cm}^{-1}$ . This arises from an  $E_{2g}$  phonon [138], but I shall refer to it simply as the hBN peak.<sup>6</sup> The fitted intensities of the 2D and hBN peaks were then used to determine points corresponding to graphene and hBN areas as shown in figures 5.6 (a) and (b), and figure 5.3.

Figure 5.6 (c) shows a map of the D to G peak intensity ratio,  $I_D/I_G$ , which is used as an indicator of lattice defect density in graphene. The near-zero values on most of the flake indicate a very low defect density [92]. The areas previously identified as fractures show a high defect density, which gives further evidence that the assignment was correct. Some features, which are seen on top of the hBN in the AFM, correlate to fractures in the graphene, which propagate from the hBN covered area to the area of bare graphene.

Figure 5.6: Heterostructure A Raman intensities. (a) 2D peak intensity, red lines indicate the threshold intensity above which the sample was identified as containing graphene. (b) hBN peak intensity, yellow dotted lines indicate the threshold intensity above which the sample was identified as containing hBN. (c) D to G peak intensity ratio. Grey areas correspond to regions with no graphene.



To better verify the thickness and quality of the graphene, I show histograms of the 2D to G peak intensity ratio,  $I_{2D}/I_G$ , and the width of the 2D peak,  $\Gamma_{2D}$ , in figure 5.7. Both parameters are altered by the presence of hBN on top of graphene, so the bare graphene on SiO<sub>2</sub> and hBN-covered graphene are plotted separately.

For the bare graphene, the values of  $I_{2D}/I_G$  are clustered at  $\sim 2.2$ , and the values of  $\Gamma_{2D}$  at  $\sim 27 \text{ cm}^{-1}$ , which are typical values for SLG on SiO<sub>2</sub> [128]. We can assume that the part of the same graphene flake that is covered by hBN is of the same intrinsic quality.

A scatter plot showing the distribution of  $\omega_G$  and  $\omega_{2D}$  across heterostructure A is shown in figure 5.8. The axes showing the vector decomposition scheme described above are added for clarity (as in figure 5.2).

By colouring the points corresponding to bare graphene and hBN-covered graphene differently, it is clear that the presence of the hBN divides the scatter plot into two main populations: the hBN covered points are shifted in the direction corresponding to more compressive strain and decreased doping. Within both separate populations, there are well defined clusters spread out parallel to the hydrostatic strain direction and less-well defined clusters aligned with the doping direction. This indicates that there is a spread of values of both strain and doping in the heterostructure, but that most of the variation in Raman shift is caused by the strain.

A map of the hydrostatic strain, calculated for each pixel in the Raman map, is shown in figure 5.9 (a).

The graphene beneath the hBN is significantly more compressively strained, at  $\sim -0.1\%$  strain, than the uncovered graphene, which shows tensile strain, at  $\sim 0.5\%$ . This is to be expected, as during fabrication the heterostructure was stacked at a high temperature and then allowed to cool to ambient temperature according to the method described in reference [139]. The different thermal expansion coefficients of hBN and graphene cause them to contract differently, effectively putting a strain on both materials [122].

At the most prominent fractures, the strain is relaxed to nearly zero, which, again, is to be expected, as fracturing is a mechanism

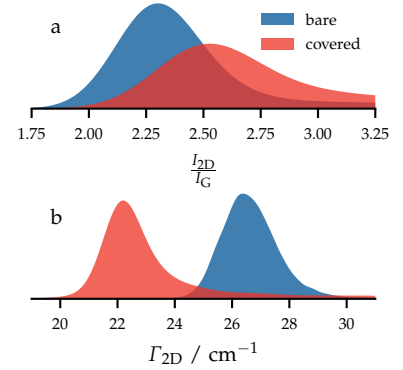


Figure 5.7: Key Raman indicators for bare and hBN-covered graphene. (a) 2D to G peak ratio. (b) 2D peak width. Histograms shown are Gaussian kernel density estimates.

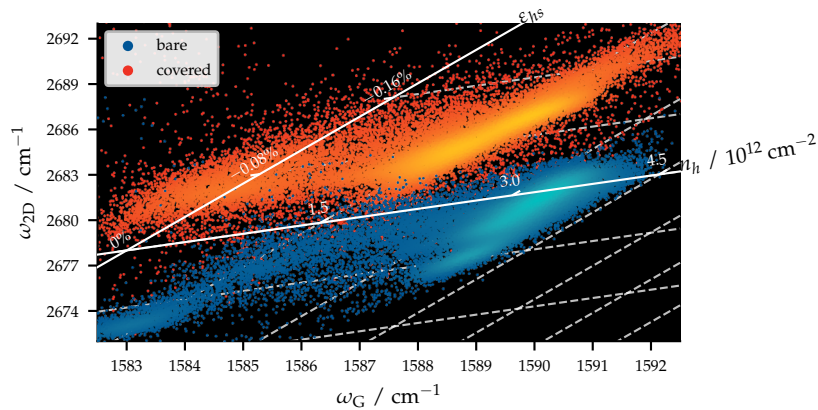
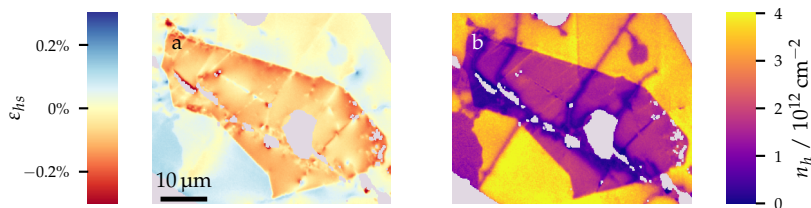


Figure 5.8:  $\omega_G$ - $\omega_{2D}$  scatter plot for bare and hBN-covered graphene. White superimposed axes can be used to read the corresponding values of hydrostatic strain and hole doping for each spectrum. Points are lightened according to their local density in the  $\omega_G$ - $\omega_{2D}$  space, so that the distribution can still be seen clearly even when points overlap.

Figure 5.9: Spatial maps of strain and doping in bare and hBN-covered graphene. **(a)** Hydrostatic strain distribution. **(b)** Hole concentration distribution. Grey areas correspond to regions with no graphene.



that takes a system from a state of high strain to a relaxed state.

At the upper right edge of the graphene, there is a region with less tensile strain than the rest of the bare graphene. The close proximity to the large fracture is likely to cause relaxation of a significant area of the graphene flake nearby.

On the other hand, at the graphene fold (shown in figure 5.4 (b)) and the area of graphene spreading out from the fold, there is a higher degree of tensile strain than in the surrounding area of graphene. It should be noted that while the area of high tensile strain is directly localised at the fold, its shape does not coincide with the fold. In other words, it protrudes significantly wider than the topological dimensions of the fold.

It is interesting to note that many of the physical features of the sample appear clearly by their effect on the strain, whereas they are comparatively subtle in the AFM.

Figure 5.9 (b) shows the corresponding map for the hole concentration of heterostructure A. The average doping of graphene protected by the hBN layer is  $\sim 1 \times 10^{12} \text{ cm}^{-2}$ , which is significantly lower than the  $\sim 3 \times 10^{12} \text{ cm}^{-2}$  value for the exposed graphene. This clearly demonstrates the protective properties of the hBN layer, which shields the underlying graphene from environmental adsorbates, the primary source of external charge carriers in exfoliated graphene [134].

A decrease in carrier concentration is observed both at folds and fractures in graphene, and also at those areas where a fold spreads out into the surrounding graphene. Interestingly, this reduction is seen both in hBN-covered graphene and bare graphene, indicating that in this case the effect is not related to the environmental doping.

At both folds and fractures, we can expect a certain degree of delamination of the graphene from the substrate. Having ruled out our environmental effects, it is therefore likely that the lower doping at these features is due to a reduction of charge transfer from  $\text{SiO}_2$  to graphene.

### 5.2.2 Heterostructure B: encapsulated graphene with bubbles

Heterostructure B is shown in the annotated optical image in figure 5.10. It consists of a sheet of SLG sandwiched between two flakes of hBN, both of  $\sim 20 \text{ nm}$  in thickness.

During the transfer process, bubbles were introduced between the layers, most likely due to stacking at an insufficiently high temperature [139]. Many of these bubbles are large enough to be clearly

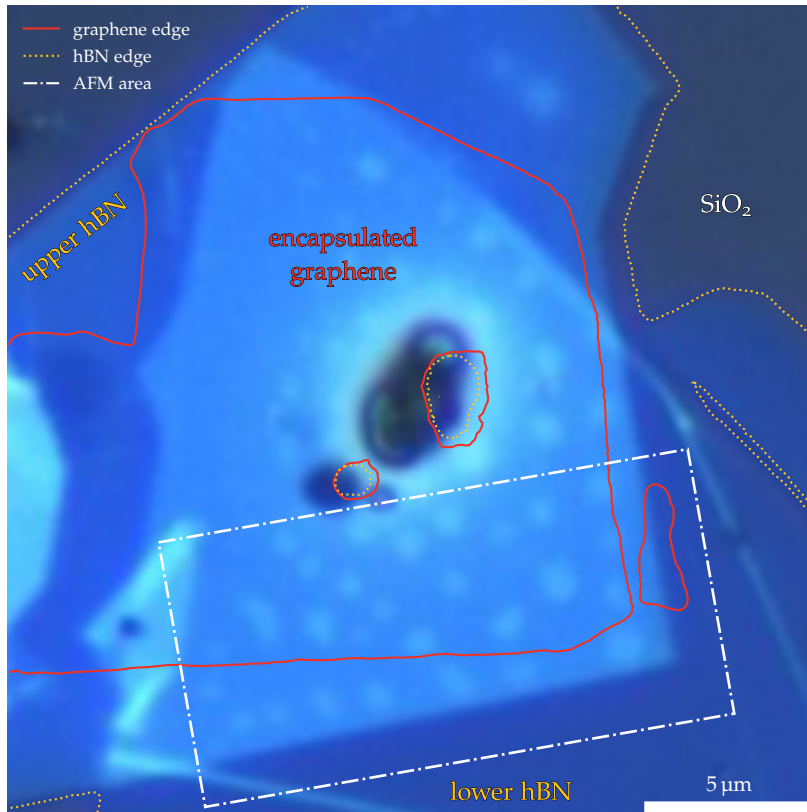


Figure 5.10: Heterostructure B optical image. Outlines showing the graphene and hBN edges are determined from the heights of the graphene 2D peak and hBN peak, shown in figure 5.12. The dark spots in the centre of the heterostructure are surface contamination.

observed both optically and via AFM, as shown in figure 5.11, even through the  $\sim 20$  nm-thick hBN on the top of the heterostructure.

As for heterostructure A, a Raman datacube was collected from the heterostructure, and Lorentzians were fitted to the graphene and hBN peaks. The fitted intensities of the 2D and hBN peaks were then used to determine points corresponding to graphene and hBN areas as shown in figures 5.12 (a) and (b), and figure 5.10.

The map of the D to G peak intensity ratio ratio in figure 5.12 (c) shows a low average defect density. However, there are high  $I_D/I_G$  values at the edge of the graphene sheet inside the hBN, which is to be expected, and there are 1d features, which spread from the upper right of the flake where graphene is exposed to the air (as shown in figure 5.10). These features can be attributed to fractures introduced during the stacking of the heterostructure. Interestingly they are not visible in either the optical or AFM images.

In general, the bubbles are not visible in the defect map, which indicates that the bubbles do not damage the graphene lattice via excessive strain. Though there are some bubbles in the lower right of the heterostructure which show high defect density. These defects were introduced by mistake in previous Raman measurements, by using a laser power which was too high, so are not an intrinsic property of the sample.

The graphene and hBN to the left of the Raman scanned area is not fully encapsulated and is complicated by folds in the hBN, as can

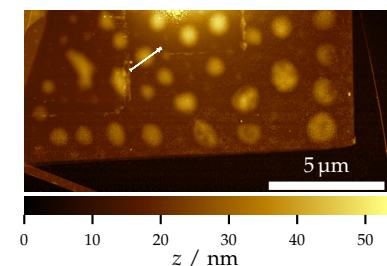


Figure 5.11: Heterostructure B AFM image, taken from the area indicated in figure 5.10. The white arrow shows the location and thickness of the line profile shown in figure 5.16. The contamination shown in figure 5.10 meant that an image of the whole heterostructure couldn't be captured.

Figure 5.12: Heterostructure B Raman intensities. **(a)** 2D peak intensity, red lines indicate the threshold intensity above which the sample was identified as containing graphene. **(b)** hBN peak intensity, yellow dotted lines indicate the threshold intensity above which the sample was identified as containing hBN. **(c)** D to G peak intensity ratio. Grey areas correspond to regions with no graphene.

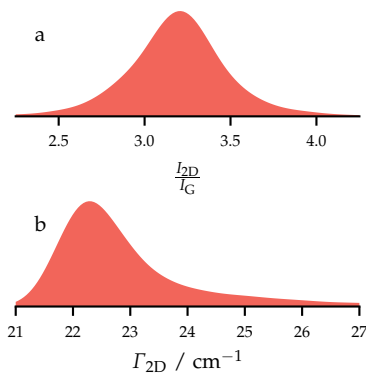
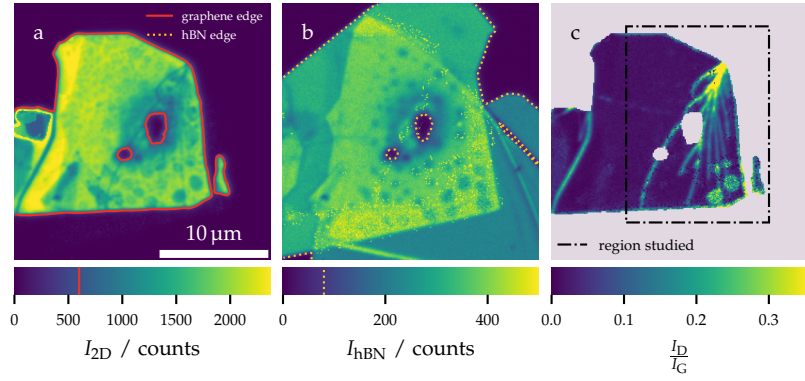


Figure 5.13: Key Raman indicators for encapsulated graphene. **(a)** 2D to G peak ratio. **(b)** 2D peak width. Histograms shown are Gaussian kernel density estimates.

be seen in figures 5.12 (a) and (b), and figure 5.10. For this reason I will limit the area of the scan focused on in the rest of this section to the smaller region indicated in figure 5.12 (c). Only a very small portion of the remaining graphene is not fully encapsulated (at the top-right and bottom-right extremes of the graphene area).

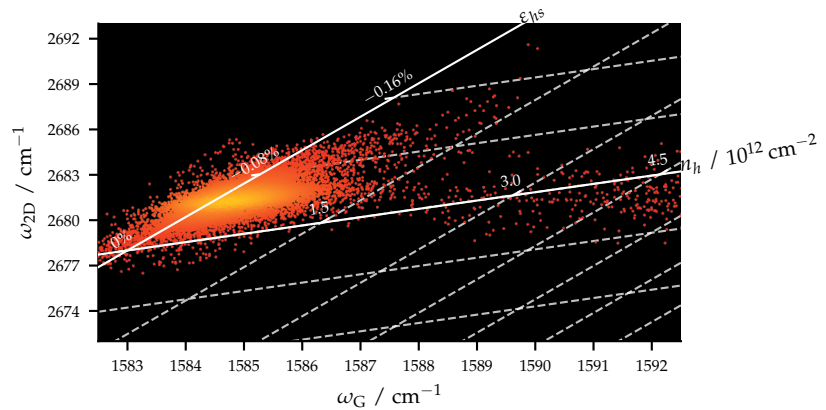
The histograms in figure 5.13 show values of  $I_{2D}/I_G$  and  $\Gamma_{2D}$  clustered at  $\sim 3.2$  and  $\sim 22.5 \text{ cm}^{-1}$  from the graphene in this region. These are typical values for good-quality hBN-encapsulated SLG [101].

A scatter plot showing the distribution of  $\omega_G$  and  $\omega_{2D}$  across heterostructure B is shown in figure 5.14. Once again, the axes showing the vector decomposition scheme described above are added for clarity (as in figure 5.2).

The points on the scatter plot are much more densely packed than they were for heterostructure A, implying a smaller overall variation in both doping and strain. This is a reflection of the fact that the majority of the graphene flake is fully encapsulated, as well as the smaller size of the area under inspection.

The average carrier concentration is close to zero, indicating that graphene is close to charge neutrality as would be theoretically expected for fully encapsulated graphene, as hBN shields graphene from environmental adsorbates and substrate doping [11, 30, 68, 140]. We also observe the scatter in  $\omega_G$  of  $\sim \pm 1 \text{ cm}^{-1}$  reported by

Figure 5.14:  $\omega_G$ - $\omega_{2D}$  scatter plot for encapsulated graphene. White superimposed axes can be used to read the corresponding values of hydrostatic strain and hole doping for each spectrum. Points are lightened according to their local density in the  $\omega_G$ - $\omega_{2D}$  space, so that the distribution can still be seen clearly even when points overlap.



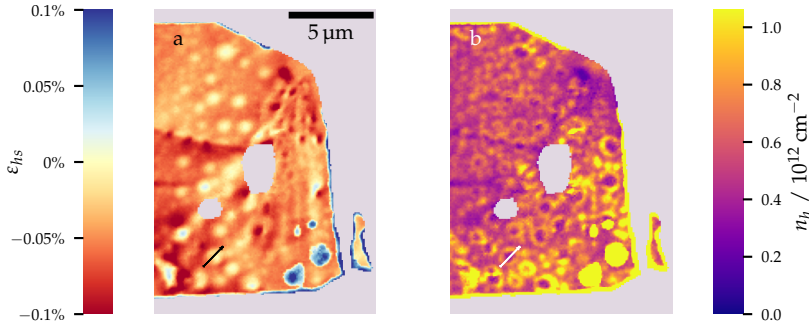


Figure 5.15: Spatial maps of strain and doping in encapsulated graphene. **(a)** Hydrostatic strain distribution. **(b)** Hole concentration distribution. Grey areas correspond to regions with no graphene. The black and white arrows show the location and thickness of the line profiles shown in figure 5.16.

previous works [108, 128].<sup>7</sup>

The map of the hydrostatic strain across the heterostructure is presented in figure 5.15 (a).

The native strain in the encapsulated graphene is slightly more compressive compared to freestanding graphene, with the strain varying from around  $-0.06$  to  $-0.03$  %.

Within the bubbles, the graphene becomes nearly strain-free or slightly tensile strained. The damaged bubbles in the lower right part of the heterostructure show a tensile strain of  $\sim 0.06$  %, though the high defect density there means the vector decomposition analysis may be less reliable. In all cases, the peak value of the tensile strain is at the centre of the bubbles, which is to be expected for bubbles in 2d materials [70, 136].

At the 1d features shown in the defect density map in figure 5.12 (c), there may be a small relaxation of the compressive strain, however the strain variations that correlate to bubbles make this difficult to judge. At the edges of the graphene flake, there is a higher tensile strain of  $\sim 0.06$  %, except for the small area of graphene in the top right corner, which is exposed to the air and only in contact with the lower of the two hBN flakes. It is interesting to note that there are a relatively large number of small bubbles clear from the strain map that are not visible in either the optical image or AFM.

The map of the hole doping is presented in figure 5.15 (b).

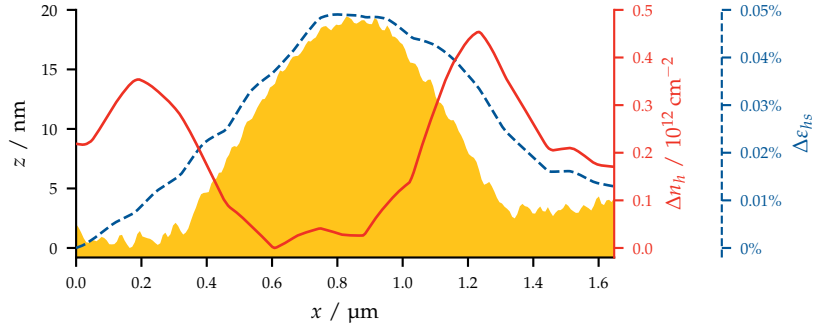
As shown in figure 5.14, the encapsulated graphene is close to charge neutrality. However, the spatially resolved doping image shows that rather than being random, the scatter in the peak positions is correlated to nanoscale features of the heterostructure. The ability to resolve such features clearly demonstrates the capability of the confocal Raman method to probe carrier concentration variation over nanoscale domains.

The bubbles have a clear effect on the carrier concentration, however the profile of the charge distribution across a bubble in this sample looks very different to that for strain. The charge distribution shows a crater like shape with rings of positive charge forming along the bubble edge.

Line profiles, taken across a bubble in the strain and doping maps together with an AFM height profile, are shown in figure 5.16. Unlike

<sup>7</sup> It is interesting that some points are returned on the left of the strain axis, which should supposedly be unpopulated, as shown by figure 5.2. This is most likely due to a small offset of the origin point caused by dielectric screening, as discussed in section 5.1.1.

Figure 5.16: Line profiles taken across a bubble. The filled area shows the height determined by AFM. The red solid line and blue dashed lines show the hole concentration and the hydrostatic strain, determined by Raman. The location of the profile in the heterostructure is indicated in figures 5.11 and 5.15.



the strain, which peaks at the centre of the bubble, where the AFM also shows the greatest height, the charge concentration is greatest on the sides and edges of the bubble. It is important to note that bubbles in graphene are buried under the  $\sim 20$  nm-thick top layer of hBN, which masks the exact topography of the bubbles as measured by AFM.

It is worth considering the possible mechanisms that can lead to such charge density fluctuations in the bubble structures.

It has been shown that nanoscale bubbles can induce PMFs in graphene [20], which can lead to the emergence of pseudo-Landau levels and cause charge density variations within the bubbles [15, 141–143]. However, fitting the height and strain profiles of the bubbles in this work to simple membrane models [143, 144] suggests that the resulting PMFs are too weak ( $\sim 10$  mT) to induce the strong spatial fluctuations seen in the experiment.<sup>8</sup>

In the absence of pseudomagnetic effects, a sharp interface at the edge of the bubble can induce electronic standing waves within the bubble [15, 143], similar to a quantum corral [145]. Certain modes in such systems exhibit ring like features [146], but a wider range of modes with different features, including central peaks, should occur for bubbles of different sizes, whereas the experimental system studied here only shows ring type features. Furthermore, the Fermi wavelengths required for such long-range oscillations are inconsistent with density fluctuations of  $\sim 1 \times 10^{12} \text{ cm}^{-2}$  in the experimental system.

Sharp interfaces can also give rise to significant localised states in their own right [15, 143] due to discontinuities in the strain profile, but the bubbles in this system do not present sharp enough interfaces when approximated using the membrane model. Furthermore, no discontinuities are noticed in the strain profiles near the bubble edges in figure 5.16.

A work by Huang et al. reported qualitatively similar features in Raman on graphene bubbles [147], which they attribute to optical standing waves forming inside the bubbles at certain heights. However, the bubbles studied in that work are on the order of hundreds of nanometres high and several microns in radius, much larger than those studied in this work, which I measure from AFM to be

<sup>8</sup>I'm grateful to Stephen Power and Antti-Pekka Jauho for this analysis.

$(18 \pm 3)$  nm in height and  $(600 \pm 100)$  nm in radius. It is therefore unlikely that the doping variations we see are due to the same mechanism.

Increased reactivity is predicted when graphene is strained [148], and a consequent charge transfer between graphene and various adsorbants could lead to charge density fluctuations. However, the increase in charge density in our case does not coincide with the maximum strain, and there are no defect signatures in the Raman data.

Ruling out these possibilities, the charge density features could be caused by modulation of the graphene-hBN interaction near the cavity edge, possibly due to varying interlayer separation [149] or edge potentials at hBN edges [150].

### 5.3 Conclusions

In this chapter, I showed how vector decomposition analysis of Raman spectra allows us to separately probe the mechanical strain and charge doping of graphene heterostructures. In turn this can reveal important details about the structure and quality of the materials. The two heterostructures investigated allowed us to study three types of graphene: bare graphene on SiO<sub>2</sub>, hBN covered graphene, and fully hBN-encapsulated graphene.

As both the bare and hBN covered graphene were in heterostructure A, I was able to directly probe the effects of the capping layer on the material properties. I observed an increased compressive strain, caused by thermal contraction of the hBN after it was stacked at high temperature [122, 139], and a decrease in carrier density, caused by protection from environmental adsorbates [11]. However a doping reduction at fractures and folds, attributed to delamination from the substrate, was observed for both bare and covered graphene. This shows that even after protecting the graphene from the atmosphere, there may still be a sizeable contribution to the graphene charge disorder arising from varied interaction with the SiO<sub>2</sub>.

As only fully encapsulated graphene was probed in heterostructure B, the variations in strain and doping were much less significant than in heterostructure A. This is to be expected, as the graphene was protected from charge disorder from both the atmosphere and the substrate. The variations that remained were dominated by the high density of interlayer bubbles in the heterostructure. The strain profile of the bubbles was as expected, with the centres of bubbles more tensile strained than the edges. By contrast, the doping profile of the bubbles was marked by interesting ring-shaped features, which were difficult to explain, but may arise from varying interlayer spacing between the graphene and hBN.

The foremost advancement presented in this work was the combination of the vector decomposition analysis with high-resolution confocal Raman, to enable spatially resolved, quantitative imaging of nanoscale strain and doping. Previous works using the same ana-

lysis model focused primarily on analysing the average properties of samples by looking at the distributions of points in  $\omega_G$ - $\omega_{2D}$  scatter plots, and they reported a scatter in  $\omega_G$  of  $\sim \pm 1 \text{ cm}^{-1}$  [108, 128]. But with spatial mapping, and comparison with colocalised AFM, I showed that this scatter is not random, but results from variations in strain and doping arising from nanoscale features of the samples, such as cracks, folds, wrinkles and bubbles.

If strain engineering of 2d materials is to become viable, we will need a thorough understanding of the role played by features like these in determining the strain and doping of graphene-based devices and heterostructures. The method demonstrated here provides a purely optical, non-invasive tool for probing arbitrary strains and doping in graphene at the nanoscale. It can reveal variations in physical parameters that are not accessible by methods like AFM or optical microscopy alone, so could form a crucial diagnostic tool for quality control of graphene-based nanodevices.

## 6

# *Subwavelength infrared domains within graphene bubbles*

In chapter 5 I demonstrated a method for imaging graphene's strain and doping using vector decomposition analysis of Raman datacubes. I also showed that interlayer bubbles in hexagonal boron nitride (hBN)-encapsulated graphene introduce nanoscale strain and doping variations, which can be successfully imaged using the technique.

In this chapter, I build upon that work by measuring interlayer bubbles in another, less disordered, encapsulated graphene heterostructure. I use scanning near-field optical microscopy (SNOM) to show that bubbles with complicated shapes contain strongly absorbing, subwavelength domains for infrared (IR) light. Comparing these results with Raman strain and doping maps, as well as atomic force microscopy (AFM) and atomic force microscope infrared spectroscopy (AFM-IR) measurements, I conclude that the domains we see are influenced by strain in the graphene. This result has key consequences for the design of strain-modulated, graphene-based optoelectronic devices in the IR.

Much of the work in this chapter has been published in the paper *Strongly Absorbing Nanoscale Infrared Domains within Strained Bubbles at hBN-Graphene Interfaces* in the journal ACS Applied Materials & Interfaces (see [Dissemination](#)). I'm very grateful to our collaborators at the University of Manchester, particularly to Matt Hamer, who fabricated the heterostructure studied in this chapter.

The unique optoelectronic properties of graphene and hBN make them ideally suited for a variety of IR applications [27, 151]. In graphene, coupled oscillations of light and free charge carriers called plasmon polaritons (PPs) have wavelengths many orders of magnitude smaller than the diffraction limit, long lifetimes and exceptional electronic tunability via gating [22, 152, 153].

Similarly in hBN, coupled oscillations of optical phonons and light called hyperbolic phonon polaritons (HPhPs) have short wavelengths and long lifetimes, as well as negative phase velocities [34, 35, 154, 155]. When the two materials are layered together in van der Waals (vdW) heterostructures they support hybrid phonon-plasmon polaritons [64], as well as even longer polariton lifetimes [23] and moiré

modulated polariton dispersions [156]. A range of optoelectronic devices have exploited these properties, including photodetectors operating in the IR [157] and THz [158] regions, and optical modulators with footprints as small as 350 nm [8, 159].

Recently, a great deal of attention has been paid to the effects of strain on two-dimensional (2d) materials [13]. Examples of strain effects in the IR regime include demonstrations that the dispersion of HPhPs is altered by the presence of strain in hBN [160], and that wrinkles in graphene may act as scattering sites for PPs [161].

Bubbles and wrinkles in vdW heterostructures are deformations, which are well known to correlate with strain in 2d materials [70, 162]. These features have recently emerged as an interesting platform to study the effects of strain effects. For example in transition metal dichalcogenides (TMDs) bubbles have been shown to act as highly localised photoluminescent emitters, with strain-dependent peak energies [73]. Similarly in graphene, nanoscale bubbles have been shown to act as localised plasmonic hotspots [123], and to sustain high-Tesla pseudomagnetic fields [20, 126]. On top of that, graphene wrinkles have shown unequivocal quantum dot signatures [19] and both wrinkles and bubbles have been proposed to be effective valley splitters [14, 18, 19, 163, 164].<sup>1</sup>

<sup>1</sup> See section 1.1.2 for more detail on the effect of strain on graphene's electronic properties.

Bubbles in vdW heterostructures arise from the ultra-thin layer of surface contamination that coats 2d materials [5, 71, 72]. This contamination is believed to originate either from adsorbed atmospheric hydrocarbons and water vapour [5, 11], or from polymers used during heterostructure fabrication [88]. They are formed via the self-cleaning mechanism of vdW heterostructures described in section 2.2.2.

One benefit of using bubbles to study strain in 2d materials is that the stochastic nature of their formation means they provide a wide range of strain values and configurations. This means that, with a suitable method to measure local strain, a single sample can be used to correlate strain with any strain induced effects, without the need for external sources of strain variation. These strain-induced effects have great potential for exploitation in novel devices, which may be based on bubbles themselves, or on more controllable methods of straining 2d materials, such as transfer onto engineered substrates [113, 136, 165–169].

From a different perspective, the ubiquity of bubbles means it is also important to understand any unintended effects they may have on devices, for quality control purposes. Particularly because the small sizes of modern devices are comparable to those of typical bubbles in van der Waals heterostructures. For large-scale production of graphene-based IR devices to become viable, knowledge of the role that bubbles may play in device performance is vital.

The practice of encapsulating graphene in hBN is now standard for graphene devices intended for ambient operation, as described in section 2.2.1. In the IR, hBN encapsulation has been shown to enable low loss PPs in graphene, with strong field confinement and

hybridisation with hBN HPhPs [23].

In this chapter, I use SNOM to probe the nanoscale IR response of a network of variously shaped bubbles in an hBN-encapsulated graphene heterostructure. This reveals distinct domains with significantly enhanced absorption within individual bubbles at wavenumbers,  $k$ , in the region of  $1000\text{ cm}^{-1}$ . The same domains are not reproduced at  $1362\text{ cm}^{-1}$ , which shows the effect is wavelength dependent. The domain boundaries correlate with ridges in the shape of the bubbles, which leads us to attribute them to nanoscale domains with different strain configurations. I investigate this further by using confocal Raman spectroscopy, along with vector decomposition analysis (as described in chapter 5), to create spatial maps of strain and doping variations in the same heterostructure. I demonstrate that networks of bubbles induce mixed and intricate strain configurations, with localised areas of mostly uniaxial or biaxial strain. This is accompanied by a pronounced increase in hole doping induced by the contaminants in the bubbles.

### 6.1 Network of bubbles in encapsulated graphene

The encapsulated graphene sample studied in this chapter was fabricated from mechanically exfoliated crystals using the (poly)methyl methacrylate (PMMA) dry transfer technique which is described in section 2.2.3.

A  $\sim 1.2\text{ nm}$ -thick hBN layer was used to pick up a graphene crystal with a suitable area of single layer graphene (SLG). The resultant stack was then deposited onto a  $\sim 220\text{ nm}$ -thick crystal, which had been exfoliated onto a  $290\text{ nm}$ -thick  $\text{SiO}_2$  substrate. After the transfer, the sample was annealed for 3 hours at  $300\text{ }^\circ\text{C}$ , to promote bubble formation via self cleaning [70].

Based on observations made during each step of the transfer (and the Raman analysis in section 6.4 below), I assume that the contamination in the bubbles in the final heterostructure is trapped between graphene and the lower hBN layer.

Figure 6.1 shows a schematic cross-section of the final structure of the heterostructure, and a top-down optical microscope image of the heterostructure is shown in figure 6.2.

The thick lower hBN layer fills the entire field of view. The SLG area was identified by Raman spectroscopy and is indicated with a solid, yellow line. The extent of the upper hBN layer, which is hard to see in the optical image, was identified using AFM and is indicated with a dashed, blue line. The darker purple areas in the image are multilayer graphene.

Many bubbles with varied shapes and sizes are visible as blue dots in the encapsulated area of the heterostructure. In the rest of this chapter I will focus on a representative area of the heterostructure, which is indicated by a black, dotted rectangle in figure 6.2.

Zooming in on that area using peak-force tapping AFM reveals that the large bubbles are connected by thin wrinkles or filaments. It

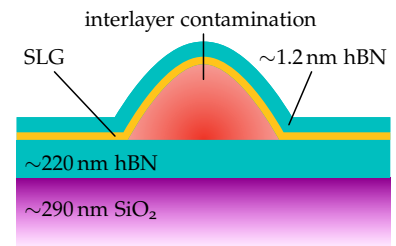


Figure 6.1: Side-on schematic of the heterostructure studied in this chapter.

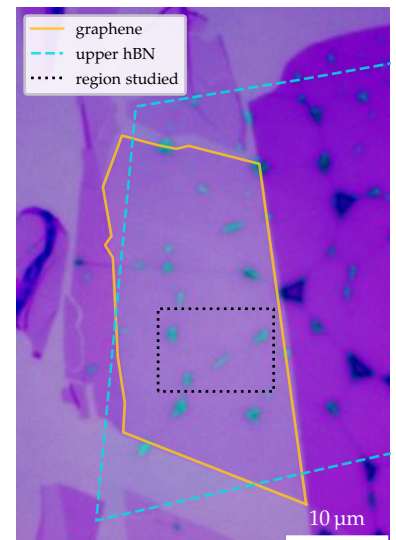
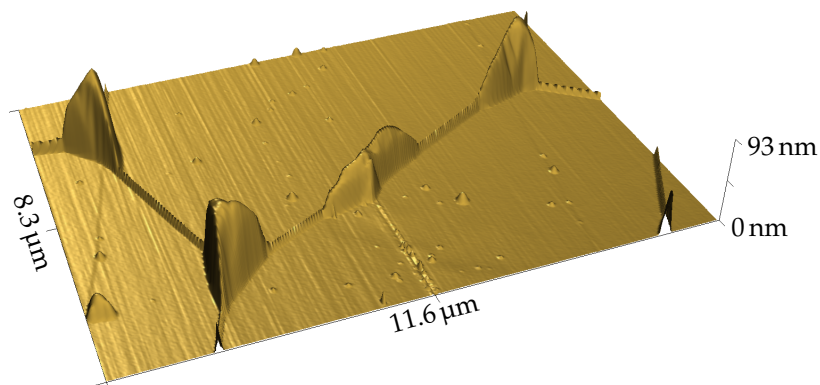


Figure 6.2: Optical microscope image showing bubbles in encapsulated graphene. I'm grateful to Matt Hamer for this image.

Figure 6.3: AFM topography of bubbles in an encapsulated graphene heterostructure. The scale of the z-coordinates has been exaggerated to show topographical features more clearly.



also reveals smaller, more circular bubbles, which are disconnected. This is shown in the three-dimensional (3d) image in figure 6.3.

These filaments are related to the shape of the bubbles, with the number of filaments connected to each bubble corresponding to the number of sharp corners in its footprint. This signals that the proximity of the bubbles in this heterostructure led to their exerting a collective influence on each other's shape during formation, which may explain their varied and complicated geometry.

As well as the filaments, the AFM also shows one-dimensional (1d) ridges in the sides of the larger bubbles, which separate regions of different curvature. Such 1d features in 2d materials result from Poisson contraction [170], a feature associated with uniaxial strain configurations [19].

The scratch visible in the centre of the image was introduced during fabrication and is not due to the peak-force AFM, which used a gentle setpoint of 500 pN to avoid damaging the bubbles.

Importantly, the large variety of shape deformations introduced to the 2d materials by the bubbles shows that this area must feature a wide range of strain configurations, making it well suited to studying strain effects in graphene.

## 6.2 Nanoscale infrared domains within bubbles

If graphene and hBN are to be exploited in nanophotonic devices, it is important to understand the effect of any nanoscale features on their local IR properties. I used SNOM to probe how the bubbles affect our heterostructure's IR response.<sup>2</sup> This allows imaging of complex light-matter interactions at a resolution many orders of magnitude below the diffraction limit, typically  $\sim 30$  nm, as described in section 3.2.

Figure 6.4 shows the third-harmonic near-field scattering amplitude,  $s_3$ , and phase,  $\phi_3$ , from the same area of the sample as shown in figure 6.3. The maps were taken using excitation wavenumbers of 1000 and  $1362\text{ cm}^{-1}$ .

The backscattered amplitude at  $1000\text{ cm}^{-1}$ , shown in figure 6.4 (a),

<sup>2</sup> See section 3.2 for detail on this technique.

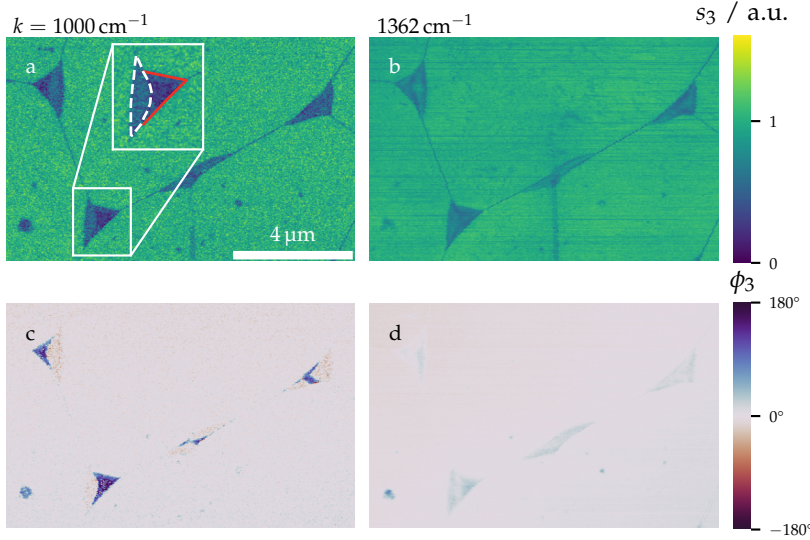


Figure 6.4: SNOM maps of a network of bubbles in encapsulated graphene at  $k = 1000$  and  $1362 \text{ cm}^{-1}$ . (a, b) Near-field scattering amplitude, normalised to the flat graphene by dividing by the median value from the image. (c, d) Near-field scattering phase, normalised to the flat graphene by subtracting the median value from the image. The enlarged portion of (a) highlights the distinct domains observed within a single bubble.

is significantly reduced at the bubbles and filaments, and there are two distinct levels of contrast seen within the larger bubbles. One level has an amplitude of  $\sim 0.6$  and the other has an amplitude  $\sim 0.25$  times the level of the flat graphene (shown by red and white outlines in the zoomed portion of the image). Interestingly, these two distinct amplitudes form sharply bounded domains, whose edges correlate well with the 1d ridges in the sides of the bubbles which were seen in figure 6.3.

The amplitude at  $1362 \text{ cm}^{-1}$ , shown in figure 6.4 (b), is also reduced at bubbles and filaments compared to the flat graphene, however to a lesser extent. The amplitude within the bubbles is also more homogeneous and the same pronounced domains are not observed.

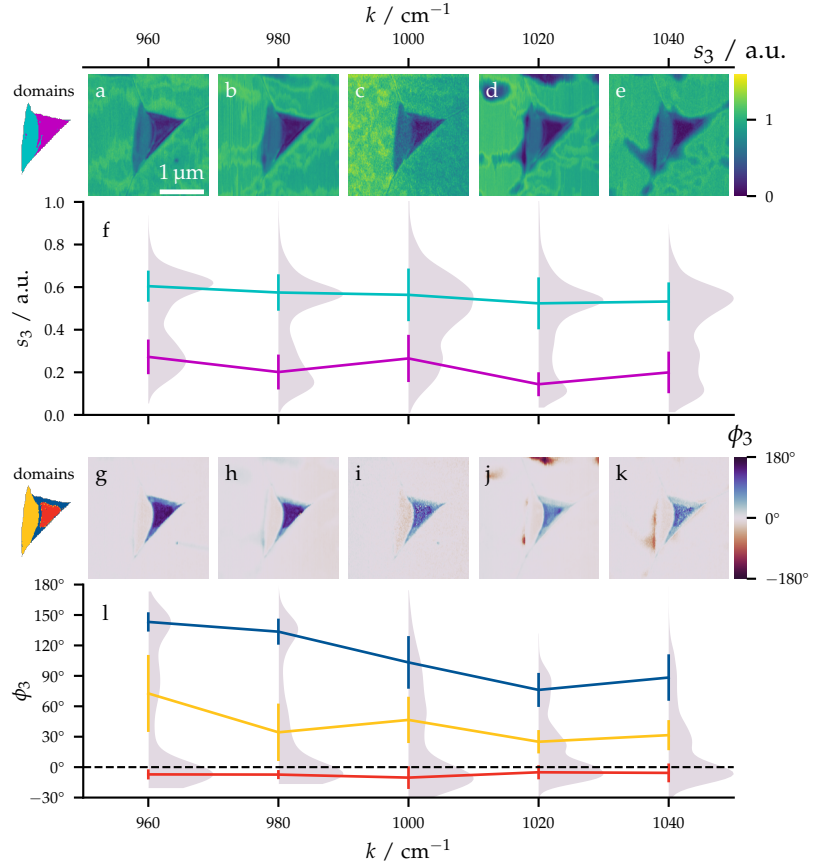
Figure 6.4 (c) shows the corresponding near-field scattering phase at  $1000 \text{ cm}^{-1}$ . The same domains seen in figure 6.4 (a) are clearly visible, with their sharp boundaries appearing in the same position. The parts of the bubbles with the greatest amplitude reduction have a significant phase shift of  $\sim 90^\circ$ . This is particularly noteworthy, because such large phase shifts are a hallmark of strong light-matter interactions, which may indicate polaritonic resonances in the material [79]. The remaining parts of the same bubbles are characterised by a slight negative phase shift of  $\sim 5^\circ$ .

Conversely, the phase shifts within bubbles at  $1362 \text{ cm}^{-1}$ , shown in figure 6.4 (d), are much smaller, at  $\sim 30^\circ$ , and the domain structure is significantly less pronounced.

### 6.3 Spectroscopic characteristics of the bubbles

To investigate the wavelength dependence of the sharp domains that appear at  $1000 \text{ cm}^{-1}$  in more detail, the bubble highlighted in figure 6.4 (a) was imaged repeatedly at a higher resolution, while changing  $k$  from  $960$  to  $1040 \text{ cm}^{-1}$ .

Figure 6.5: Wavelength dependence of the domains near  $1000\text{ cm}^{-1}$  for a single bubble. (a-e) Near-field scattering amplitude images, normalised to the flat graphene by dividing by the median value from each image. (f) Kernel density histograms showing the distribution of  $s_3$  values from within the bubble, overlaid with error bars showing the means and standard deviations returned from fitting a 2-component GMM. Lines are coloured to match the guide to the domains shown left of (a). (g-k) Near-field scattering phase images, normalised to the flat graphene by subtracting the median value from each image. (l) Kernel density histograms showing the distribution of  $\phi_3$  values from within the bubble, overlaid with error bars showing the means and standard deviations returned from fitting a 3-component GMM. Lines are coloured to match the guide to the domains shown left of (g).



Figures 6.5 (a-e) show the resulting third-harmonic near-field scattering amplitude maps from the bubble and the surrounding area. The bubble is again split into two domains as was seen in figure 6.4 (a).

To investigate these internal domains more clearly the  $s_3$  values from within the bubble were isolated by selecting only those values whose height in the corresponding AFM image was more than 15 nm above the median flat graphene level. The distribution of scattering amplitudes inside the bubble are shown for each  $k$  value by kernel density histograms in figure 6.5 (f).

To gain a more quantitative measure of the evolution of these domains, a Gaussian mixture model (GMM) was fit to each distribution.<sup>3</sup> This assumes that a dataset is composed of  $N$  normally distributed clusters, then uses the expectation-maximisation algorithm [171] to determine the parameters of the  $N$  Gaussian peaks which would best describe these clusters. Here  $N$  was set to match the number of experimentally observed domains.

For the  $s_3$  maps we observe two domains experimentally, so use  $N = 2$  for the GMM. The means and standard deviations of each Gaussian cluster returned by the GMM are overlaid as lines with error bars in figure 6.5 (f).

To verify that the components returned are the same as the experimentally observed domains, and to serve as a guide, the  $s_3$  points were evaluated according to which Gaussian component they are

<sup>3</sup>See chapter 8 for more details on GMM and further applications of the technique.

most likely to belong to and coloured accordingly. This is displayed, using data from  $k = 960 \text{ cm}^{-1}$  as an example, to the left of the plot.

This analysis reveals that, close to  $1000 \text{ cm}^{-1}$ , the amplitudes of each domain do not vary significantly, with the left side remaining at  $\sim 0.6$  and the right-hand side at  $\sim 0.25$  times the background amplitude, as in figure 6.4 (a).

Figures 6.5 (g-k) show the corresponding third-harmonic near-field scattering phase maps. In these images there are three, rather than two, distinct levels of phase contrast in this bubble. The third contrast level, which wasn't discernible in figure 6.4 (c), is now visible thanks to the higher resolution and slower tip speed of the smaller scans. Relative to the flat graphene, the left side has a small negative phase shift as before, and the right-hand side has a high shift in the centre which is reduced at the edges. Both phase shift domains in the right-hand side reduce with increasing  $k$ .

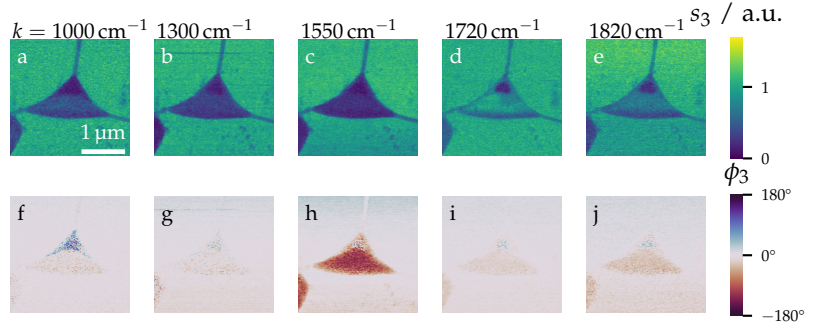
Once again, kernel density histograms, and the means and standard deviations of the domains returned by a GMM with  $N = 3$  are shown for the phase values in 6.5 (l). This reveals that the leftmost domain (shown in red to the left of 6.5 (g)) with a slight negative phase shift of  $\sim 5^\circ$  is wavenumber independent. However the domains with large phase shift are wavenumber dependent, with the centre-right domain (blue) shifting from  $\sim 150^\circ$  to  $\sim 90^\circ$  and the edges of the right-hand side (yellow) shifting from  $\sim 75^\circ$  to  $\sim 30^\circ$ , with a  $k$  increase from  $960$  to  $1040 \text{ cm}^{-1}$ . This local wavelength dependence hints that the region around  $1000 \text{ cm}^{-1}$  could be the side of an absorptive peak for these domains [172–174]. Unfortunately, the practical tunability range of our quantum cascade laser (QCL) precludes probing wavenumbers below  $\sim 960 \text{ cm}^{-1}$ , however it may be that at lower wavenumbers, further from the universal absorption regime, the phase shift is even higher.

### 6.3.1 Wavelength dependence of the domains across the mid-IR

Figure 6.6 shows the SNOM amplitude and phase images from a bubble in the heterostructure, at a wider range of frequencies than shown above, using multiple QCL sources. The main feature focused on in this chapter is the sharply defined domains, whose boundaries coincide with topographic ridges, which can be seen most clearly in figure 6.6 (f), for  $k = 1000 \text{ cm}^{-1}$ .

At other wavenumbers there is a less pronounced difference in phase between the two halves of the bubble, and there is a seemingly wavelength-independent drop in the scattered amplitude in the upper half of the bubble. This may be related to the different thicknesses of contaminant, or to a difference in the adhesion of the contamination to the bubble walls [149]. Importantly, this has less spatial correlation with the 1d ridges, which may give some explanation for the three distinct phase domains we see in figure 6.5: a superposition of effects from a wavelength-independent feature related to the bubble geometry or thickness, and a sharply bounded

Figure 6.6: Single bubble imaged with a range of frequencies. **(a-e)** Near-field scattering amplitude images at  $k = 1000 - 1820 \text{ cm}^{-1}$ , normalised to the flat graphene by dividing by the median value from each image. **(f-j)** Corresponding Near-field scattering phase images, normalised to the flat graphene by subtracting the median value from each image. The feature in the lower left of the images is a clump of surface adsorbants which accumulated at the edge of a scan region during repeated AFM measurements of another bubble (the scans in figure 6.5).



domain which only appears close to  $1000 \text{ cm}^{-1}$ .

There is also a strong absorption at  $1550 \text{ cm}^{-1}$  which is more homogeneous across the whole bubble. We see this same absorption signature from an accumulated mass of surface adsorbants (left after repeated AFM scanning of another bubble) in the lower left of the image. For this reason, we can attribute this particular absorption to the influence of the material that fills the bubble, which is very likely to be composed of the same adsorbants which accumulate on the upper surface [5].

### 6.3.2 Probing the chemical contents of bubbles with AFM-IR

Figures 6.7 (a) and (b) show SNOM amplitude and phase images from a bubble in the heterostructure outside of the region focused on in the rest of this chapter. It has the same characteristic nanoscale optical domains as the bubble shown in figure 6.5, albeit with slightly different shape.

To probe the contents of the bubble, I used resonance-enhanced AFM-IR, to collect IR absorption spectra comparable to those found from Fourier transform infrared (FTIR) spectroscopy, but with a spot size of  $\sim 30 \text{ nm}$  [86].<sup>4</sup>

The contact resonance of the tip and sample varied with the tip position, so before each spectrum was taken, the pulse rate was tuned to maximise the intensity of the measured signal. Each spectrum was normalised, then a spectrum from a flat area of the graphene-hBN heterostructure was subtracted, to remove any background signal. The resulting signal, shown in figure 6.7 (c), therefore shows the difference in IR absorption between the spectrum location, which is indicated in figure 6.7 (a), and the flat areas of the heterostructure.

The most prominent peak is  $\sim 1360 \text{ cm}^{-1}$  (though we can only see half of this peak, due to the limited tunability of our QCL). This might be attributed to the hBN  $E_{2g}$  phonon resonance at  $\sim 1370 \text{ cm}^{-1}$  [31], measured indirectly through heat transfer from hBN to the bubble contents. In general, 2d and vdW materials are hard to measure with AFM-IR, because of their high thermal conductivities and low out-of-plane thermal expansion coefficients. However if they are in thermal contact with a material with lower thermal conductivity and higher out-of-plane expansion, then they become possible to

<sup>4</sup> See section 3.3 for more detail on this technique.

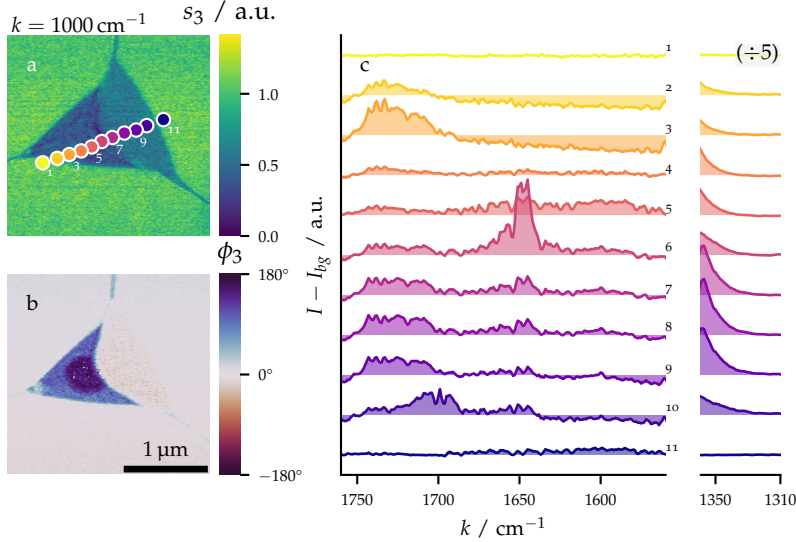


Figure 6.7: AFM-IR of a bubble in encapsulated graphene. **(a)** SNOM amplitude image. **(b)** SNOM phase image. **(c)** Normalised AFM-IR spectra taken from the locations indicated in (a). The intensity of the peak on the right has been divided by five to fit all spectra in the same plot.

measure due to heat transfer from the 2d material causing expansion of the other material [87]. This could explain why we observe an hBN absorption on the bubble, but not on the flat area of the heterostructure.

The only other prominent peak that we see is  $\sim 1650 \text{ cm}^{-1}$  in spectrum 6, taken from the boundary between two optical domains, which is most likely due to carbon-carbon double bonds. This may be from the graphene itself, perhaps measurable due to local curvature of the graphene creating a charge imbalance on either side of the lattice and therefore inducing a dipole, or it could be from some other source of carbon, either inside or outside the bubble.

Besides the features discussed above, there are no significant differences in the IR spectra obtained from different optical domains.

A recent AFM-IR work [88] was able to enhance the signal from interlayer contamination enough to differentiate between different forms of polymer contaminants, by concentrating the contamination using contact mode AFM to push bubbles together[71]. However this is necessarily a destructive technique and could not be used for in situ measurements of bubbles.

#### 6.4 Colocalised strain and doping mapping

The IR absorption domains are separated by ridges in the bubbles' shape (see figure 6.3). Such 1d features are known to result from uniaxial strain applied parallel to the feature [19, 170]. The differing bubble shape and curvature on either side of the ridges also necessitate that the domains must have different strain configurations [70, 162]. To investigate this further, I used Raman spectroscopy to visualise the strain variations in this heterostructure.<sup>5</sup>

Raman is routinely used as an indicator of strain, doping and defect density in graphene [94, 108, 128]. The solid blue line in fig-

<sup>5</sup> I used the apparatus described in section 4.2, with a 532 nm excitation laser.

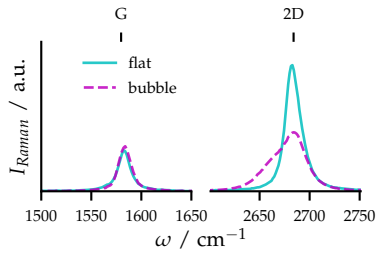


Figure 6.8: Raman spectra from a flat area (solid blue line, location indicated with a triangle in 6.10 (a)) and a bubble (dashed purple line, location indicated with a circle in 6.10 (a)).

<sup>6</sup>This effect is more significant for this sample than the ones discussed in chapter 5 due to the  $\sim 220$  nm-thickness of the bottom hBN.

Figure 6.8 shows a spectrum taken from a flat area of the heterostructure (indicated in figure 6.10 (a)), free from bubbles. It displays the characteristic G and 2D peaks of graphene, at  $\sim 1580$  and  $\sim 2680$   $\text{cm}^{-1}$ . The 2D to G height ratio of  $\sim 3$  and 2D peak full width at half maximum (FWHM) of  $\sim 20$   $\text{cm}^{-1}$  are characteristic of high-quality hBN-encapsulated SLG. The graphene D peak at  $\sim 1362$   $\text{cm}^{-1}$  (not shown) is not apparent, which is another indicator of defect-free graphene.

To produce spatial maps of strain and doping, a Raman datacube was collected from the area of the sample shown above, and Lorentzians were fit to the G and 2D peaks. The extracted positions for the peak centres,  $\omega_G$  and  $\omega_{2D}$ , are correlated in a scatterplot in figure 6.9.

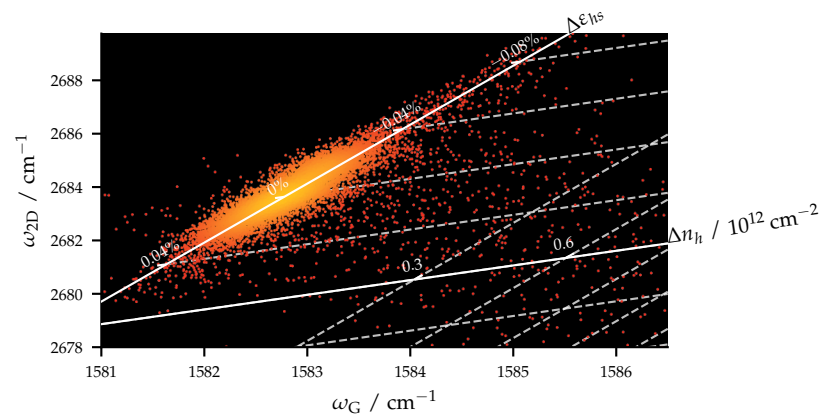
Both hole doping,  $n_h$ , and hydrostatic strain,  $\varepsilon_{hs}$ , in graphene cause a shift of the G and 2D peaks, so additional analysis is needed to determine the separate  $\varepsilon_{hs}$  and  $n_h$  contributions. This can be achieved using vector decomposition, and comparison with empirical measurements [94, 108, 114], as described in chapter 5. This vector decomposition analysis is illustrated by the additional axes shown in figure 6.9.

In this sample, the thick lower hBN layer leads to dielectric screening which displaces the position of the point  $(\omega_G, \omega_{2D})$  corresponding to unstrained, undoped graphene away from the values used to calibrate the model [101, 137]. This would add an unquantified systematic error to the values returned.<sup>6</sup> To bypass this issue I normalise both strain and doping to their median values and report relative changes,  $\Delta\varepsilon_{hs}$  and  $\Delta n$ , rather than absolute values.

The resulting strain and doping images and a map of the splitting of the 2D peak are shown in figure 6.10. For ease of comparison with the colocalised Raman-acquired maps, the AFM topography image from figure 6.3 is also included as a 2d image in figure 6.10 (a).

Figure 6.10 (b) shows the median-normalised hydrostatic strain distribution around the area of bubbles. The greatest values of tensile (positive) strain are localised at the centres of bubbles, coinciding with the areas of greatest height. Interestingly the areas of graphene and hBN in the vicinity of the bubbles (where graphene is flat and may be assumed to be undisturbed) are not free from strain. The

Figure 6.9: Strain-doping decomposition, as discussed in chapter 5.  $\omega_G$ - $\omega_{2D}$  scatter plot for encapsulated graphene. White superimposed axes can be used to read the corresponding changes of hydrostatic strain and hole doping for each spectrum. Points are lightened according to their local density in the  $\omega_G$ - $\omega_{2D}$  space, so that the distribution can still be seen clearly even when points overlap. Due to an offset induced by dielectric screening, the strain and doping values are median normalised.



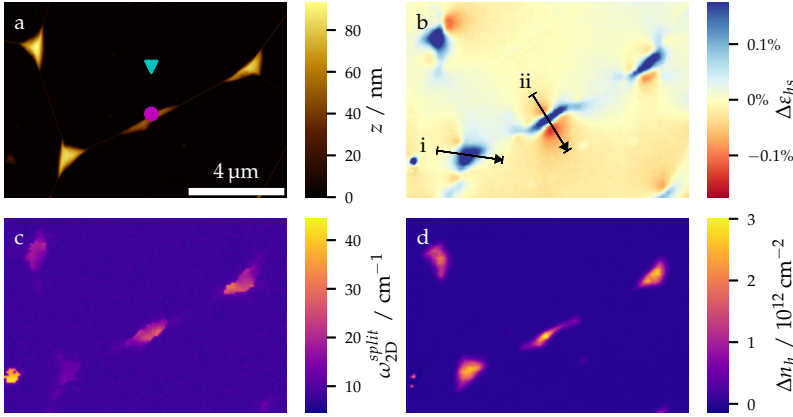


Figure 6.10: Raman acquired maps from sample. (a) AFM topography showing the same data as 6.3 for ease of comparison. Blue triangle and purple circle show the locations of the spectra in 6.8. (b) Change in hydrostatic strain relative to the median value. Black arrows show the location and thickness of the line profiles in 6.11. (c) Splitting of the 2D peak. (d) Change in hole concentration relative to the median value.

areas between bubbles, within  $\sim 2\mu\text{m}$  of the filaments seen in figure 6.3, show small increases in tensile strain relative to the background. Similar strain profiles, extending beyond the area of bubbles, have previously been observed at a smaller scale in scanning tunneling microscopy (STM) studies of graphene-hBN bubbles [17].

Additionally, at the sides of some bubbles, particularly the narrow, elongated bubble in the centre of the image, there are small areas of more compressive strain. These are due to Poisson contraction, a phenomenon associated with uniaxial strain configurations [170]. This is illustrated more clearly by the AFM and  $\epsilon_{hs}$  line profiles taken from a more biaxially and a more uniaxially strained bubble. These are marked as i and ii in figure 6.11, and their positions are marked with arrows in figure 6.10 (b).

Uniaxial strains add an anisotropic deformation to the lattice, and therefore correlate with the shear strain,  $\epsilon_s$ .<sup>7</sup> The dashed purple line in figure 6.8 shows a Raman spectrum taken from the central bubble in the heterostructure (indicated in figure 6.10 (a)). The presence of  $\epsilon_s$  has caused splitting of the 2D peak. The asymmetry in the height of the split peaks is the result of a small polarisation dependence in the Raman measurement introduced by the diffraction grating [108].<sup>8</sup>

By fitting two Lorentzians to a peak, it is possible to obtain a measure of this peak splitting. I performed this for the 2D peak, and the resulting splitting,  $\omega_{2D}^{split}$ , is shown in figure 6.10 (c). As discussed above, this should be proportional to  $\epsilon_s$ . Indeed, the greatest values of  $\omega_{2D}^{split}$  correlate well with the areas of Poisson contraction in figure 6.10 (b), providing further evidence that these areas have a more uniaxial strain configuration.

The change in hole concentration of the graphene is also returned by the vector analysis. Figure 6.10 (d) shows the median-normalised doping distribution. The concentration correlates well with the topography of the bubbles, much more so than for  $\epsilon_{hs}$ , showing an increase of  $\sim 3 \times 10^{12} \text{ cm}^{-2}$  relative to the background at the bubble locations. This confirms that the primary doping source in these bubbles is the contaminant that fills them, and that the doping and

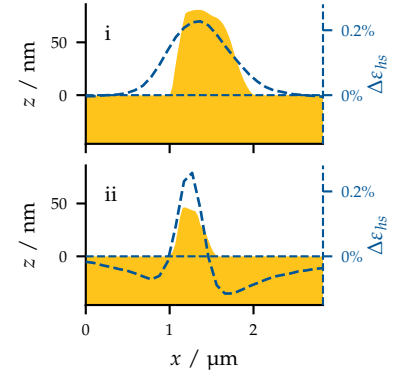


Figure 6.11: Height and strain line profiles from (i) a relatively biaxially strained bubble, and (ii) a relatively uniaxially strained bubble. Locations of (i) and (ii) are shown in 6.10 (b).

<sup>7</sup> See section 4.4.2 for the definitions of the different strain components.

<sup>8</sup> I used circularly polarised incident light to reduce this polarisation dependence as much as possible, see sections 4.4.2 and 5.1.1 for more detail on this.

strain are generally independent in this system. Doping is seen even in the case of the small, more rounded bubbles, not connected by filaments. The graphene between the bubbles is shown to be dopant-free, supporting the perception that bubble formation is an effective self-cleaning mechanism [5].

It is helpful to compare the measured changes in hole concentration with the expected behaviour. Graphene encapsulated in hBN is known to have an intrinsic doping close to charge neutrality, due to a lack of dangling bonds in the hBN and screening of the graphene from charged impurities and atmospheric dopants [11, 68, 140]. Furthermore, the self-cleaning nature of vdW heterostructures collects the typical hydrocarbon contaminants, which induce hole doping in graphene [5, 11], into bubbles.

It is notable, therefore, that the doping profile of the heterostructure relative to the median closely matches the expected absolute doping profile for encapsulated graphene, with flat areas close to charge neutrality and increased p-type doping at bubble locations. For this reason, we may make the approximation that  $\Delta n_h \approx n_h$ .

It has been predicted that an increase in  $\epsilon_{hs}$ , should induce hole doping in  $sp^2$  carbon [175], however the fact that we do not observe significant doping in the strained graphene areas between bubbles, which are far from the contaminants, suggests this is not a significant effect in our system.

We do not observe features that immediately correlate with the domains seen from SNOM in any of the Raman-acquired maps. However this is to be expected, as the spot size for our Raman measurements ( $\sim 450$  nm) is comparable to the lateral sizes of the domains ( $\sim 500$  nm).

## 6.5 Origin of the nanoscale domains

In this section I will discuss possible mechanisms leading to the formation of the SNOM-observed IR domains.

One such mechanism could be charge inhomogeneity due to chemical doping from the contaminants in the bubbles. It is known that variations in the Fermi level,  $E_F$ , can change the IR absorption of graphene. I convert between  $E_F$  and  $n_h$  using equation 1.5. Applying this to the Raman-acquired  $n_h$  values yields a map of  $E_F$ , shown in figure 6.12 (a).

The absorption of graphene is roughly proportional to the real part of its frequency-dependent optical conductivity,  $\sigma(k)$ .<sup>9</sup> At high photon energy,  $E_{ph}$ , interband transitions dominate, leading to a universal conductance value of  $\sigma_0$ , resulting in a flat absorption of  $\sim 2.3\%$ . But for photon energies below  $2E_F$ , these interband transitions are prevented by Pauli blocking, which leads to a drop in absorption and a Drude-type, metallic response to light. The position of the Pauli transition, at  $E_{ph} = 2E_F$ , depends on the level to which the graphene is doped [22].

The optical conductivity of graphene as a function of  $E_F$ , calcu-

<sup>9</sup>See section 1.1.3 for more detail on graphene's optical conductivity.

lated using the local random phase approximation (RPA), given in equation 1.14, at  $T = 0\text{K}$ , is shown for wavenumbers of 1000 and  $1362\text{ cm}^{-1}$  in figure 6.12 (b) [22]. The onset of the Pauli blocked regime occurs at  $E_F = 62$  and  $84\text{ meV}$ . To compare this calculation with the experimentally determined  $E_F$ , the values from figure 6.12 (a) are shown as a histogram in figure 6.12 (b). The Pauli transition for  $k = 1000\text{ cm}^{-1}$  is also shown as a dashed white line in figure 6.12 (a).

At both wavenumbers,  $E_F$  is below the Pauli transition for the areas of flat graphene (corresponding to the prominent peak in the histogram), which indicates that they should be in the high absorption, universal conductance regime. The doping at the bubbles shifts  $E_F$  into the Pauli blocked regime, which should be accompanied by a reduced  $\sigma$  and absorption. However, the fact that we see an increase, rather than the predicted decrease, in absorption at the bubble locations indicates that the variations cannot be explained by altered  $E_F$  alone, and that other factors need to be considered.

We should also consider the effects of the materials adjacent to graphene in bubbles. The optical characteristics of the contaminants are expected to influence the SNOM-measured absorption, via their own IR absorption and their effect on the dielectric environment of the graphene. AFM-IR measurements did not show a difference in chemical composition between domains in a bubble, which suggests that the contaminant composition is homogeneous across both domains. This is in agreement with previous transmission electron microscopy [5] and AFM-IR [88] measurements, which also showed that contaminants are expected to be homogeneously distributed within bubbles, and may be composed of atmospheric hydrocarbons or polymer residue from fabrication.

The other material in contact with the graphene is hBN. Frequencies in the range  $960$  to  $1040\text{ cm}^{-1}$  are far from the reststrahlen bands, in which hBN supports HPhPs, so we can conclude that most of the IR activity is due to the graphene. However hBN is known to reduce plasmonic losses in graphene, which should lead to a general enhancement of the near-field scattering intensity [23, 26].

One factor to consider is possible plasmonic effects in relation to the variations in IR absorption. Graphene-hBN heterostructures, doped above the Pauli transition are known to support PPs in the wavenumber region around  $1000\text{ cm}^{-1}$  [23]. Although we do not observe the plasmonic standing waves typical of SNOM measurements of PPs in graphene [22, 23, 26, 152, 153], this is likely due to the lack of low-loss reflection sites for PPs, such as graphene edges. Nevertheless, it is possible that the origin of the domains observed at  $1000\text{ cm}^{-1}$  is plasmonic in nature or has a substantial plasmonic contribution.

Theoretical simulations of self-assembled 3d graphene nanostructures, such as pyramids and polyhedrons, have suggested that vertices and edges in such structures could have strong plasmonic field enhancement due to combined in- and out-of-plane coupling of plasmonic modes [176]. However there is no clear evidence of this en-

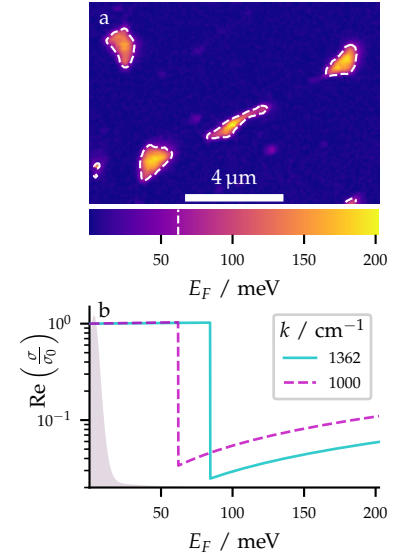


Figure 6.12: Graphene Fermi level and onset of Pauli blocking. **(a)** Fermi level calculated from the Raman-acquired data in figure 6.10. White dashed lines show the onset of Pauli blocking at  $E_{ph} = 2E_F$  for  $k = 1000\text{ cm}^{-1}$ . **(b)** Real part of graphene optical conductivity, normalised to the universal conductance value,  $\sigma_0$ . Calculated for  $k = 1000$  and  $1362\text{ cm}^{-1}$ , using the local RPA at  $T = 0\text{K}$  [22]. Experimental  $E_F$  values from (a) are shown as a normalised kernel density histogram in grey.

hancement at the bubble edges and vertexes in this chapter. This may be due to the fact that the bubbles (which have heights  $\sim 0.1 \times$  their footprints) are much flatter than the 3d self-assembled structures (which have heights comparable to their footprints). This would reduce the effect of the mode coupling.

Finally, we can consider nanoscale strain differences induced in the graphene by bubbles. Although the Raman spot size prevents us from visualising strain variations within individual bubbles, I have shown that, at a larger scale, the strain configuration from a network of closely spaced bubbles is intricate and varied. The distributions revealed, featuring Poisson contraction and increased tensile strain between bubbles, are similar to theoretical calculations of stress in graphene sheets deposited over networks of trapped particles [162].

Deformations in 2d material shape are well known to correlate with differences in strain configuration [70, 162], so I infer from the AFM topography that there are additional nanoscale strain variations within bubbles, though their characteristic size is below Raman resolution. These strain variations are expected to alter the band structure of graphene, through local modification of the lattice constant and electron hopping energies [143].<sup>10</sup>

<sup>10</sup> See section 1.1.2 for more detail on strain effects on graphene.

Importantly, 1d strain features in graphene are known to induce potential barriers, whose carrier transmission has an anisotropic dependence on strain [19]. In the bubbles studied in this work, we can expect the effect to be the most pronounced at the ridges, as well as at the sharp edges at the base [15, 143]. These have been shown to lead to confinement effects, including quantum wires and Fabry-Perot type resonators, which can also introduce density of states (DOS) quantisation [19].

The SNOM measurements in this chapter were carried out under ambient conditions at room temperature. Consequently, any potential barrier or quantised energy step must be higher than the thermal energy of the system,  $k_B T \approx 25$  meV, to play a significant role. In the case of quantum confinement effects, we expect energy steps on the order of  $\hbar v_F / b$ , where  $b$  is the characteristic width of a strain feature [14]. These exceed the thermal energy for features below  $\sim 25$  nm. This is on the lower resolution limit for our AFM, but it is likely that the sharp ridges that bound the IR domains are below this width, meaning they could present significant electronic barriers.

The presence of discrete DOS steps induced by the strain could also influence the optoelectronic behaviour of graphene through the additional energy gaps added to the band structure. These could prevent certain interband transitions from taking place, as previously allowed electronic states would become forbidden. This would lead to a breakdown of the simple model of optical conductivity described by the local RPA above [22].

Moreover, the presence of a bandgap would convert graphene into a semiconductor rather than a metallic conductor, so the Drude model of conductivity may be inappropriate, even in the already Pauli-blocked regime. As plasmons are enhanced in metals [26],

this could mean that the optical response of the strained graphene has a comparatively suppressed plasmonic contribution, compared to unstrained graphene with a similar charge doping.

## 6.6 Conclusions

In this chapter, I have demonstrated the existence of nanoscale optical domains, with strongly enhanced absorption of light around  $1000\text{ cm}^{-1}$ , in bubbles in closely spaced networks in graphene hBN-heterostructures. Using Raman spectroscopy and vector decomposition analysis, I showed that these networks induce intricate and varied strain configurations in graphene and locally dope the graphene enough to support PPs.

The different shape and curvature of the domains on either side of the ridges mean they must have different strain configurations, and consequent differences in electronic dispersion. This must further alter the plasmonic dispersion and thus also affect the wavelength-dependent degree of light-matter interaction in the graphene. It is worth reiterating that a plasmonic explanation is only one of several possible explanations, including the effect of adjacent materials on the dielectric environment and doping of graphene, as discussed above. However, in combination with the barriers presented by the ridges, this is strong evidence that the sharply bounded IR absorption domains relate to nanoscale strain differences within bubbles.

Strain-induced areas of enhanced light absorption have great potential for the design of future graphene-based IR devices. Existing approaches to devices make use of local gates [8, 177] or graphene patterned into nanostructures [155, 178, 179] to spatially modulate absorption. Networks of bubbles, like the one shown here, are generally created stochastically during heterostructure assembly. However, it is possible to control global strain in graphene by, for example, depositing it onto a flexible substrate and bending it [180]. It is also possible to create similar strain patterns to these bubble networks in more reproducible ways.

One approach involves inflating graphene bubbles, by pumping pressurised gas through networks of holes in a substrate [113, 136].

Or similarly, in a recent work by Hu et al., the height of inflated graphene membranes, suspended over patterned microwells, was controllably modulated by changing the environmental pressure [181]. Then by imaging plasmonic fringes reflecting from the edges of the microwells, they were able to demonstrate that this also led to a controllable modulation of the plasmonic dispersion. However it is important to note that, unlike the Hu paper, the domains we observe are closely linked to the unique shapes of the bubbles studied in this chapter.

An alternative approach involves depositing graphene onto arrays of nanoparticles [165–168], or inducing periodic buckling, by annealing graphene on a non-lattice-matched substrate [169]. While these approaches are not dynamically controllable, if a desired pattern of

optical properties could be induced in graphene simply by depositing it onto an engineered substrate, they could provide a pathway towards large-scale production of tailored graphene metamaterial or photonic crystal devices.

Indeed, in the following chapter I will use optical spectroscopy to investigate how two types of engineered substrates of this kind might be used to induce controlled strain profiles in another vdW material, InSe.

# 7

## *Probing strains in indium selenide with optical spectroscopy*

In this chapter I use optical spectroscopy to investigate strains in the van der Waals (vdW) material InSe.

This builds upon the work in earlier chapters, where I showed that uncontrolled features of other vdW materials and heterostructures, such as bubbles and wrinkles, introduce nanoscale strains which can be used to tune material properties. Here the focus is on ways that we can introduce such strains deliberately. I measure two InSe samples, both of which have been deposited onto substrates that were engineered to induce strains and geometric deformations to the material.

This work was part of my contribution to the paper *Anomalous Low Thermal Conductivity of Atomically Thin InSe Probed by Scanning Thermal Microscopy* by Buckley et al., in the journal *Advanced Functional Materials* (see [Dissemination](#)). I'm grateful to Zakhar Kudrynskyi and Amalia Patanè for their helpful discussions, and particularly to Nila Balakrishnan for fabricating the samples I measured in this chapter.

Indium selenide (InSe) compounds are the most heavily studied of the post-transition metal chalcogenides (PTMCs),<sup>1</sup> because they boast some distinct properties from other vdW materials. In its  $\gamma$  phase, InSe is a semiconductor with a bandgap energy that increases with decreasing layer thickness, and it undergoes a direct to indirect bandgap transition when thinned down to a monolayer [39, 40]. It also has a broadband photoresponse from the infrared (IR) to the ultraviolet [182, 183], excellent carrier mobility [41, 184], and a strain tunable bandgap [185].

In this chapter I use confocal Raman and photoluminescence (PL) spectroscopy<sup>2</sup> to investigate two samples of  $\gamma$ -InSe:

*Sample A* A  $\sim 45$  nm-thick flake bent over an array of (poly)methyl methacrylate (PMMA) nanopillars on a SiO<sub>2</sub> substrate.

*Sample B* A  $\sim 12$  nm-thick flake deposited onto an array of holes patterned into a SiO<sub>2</sub> substrate.

<sup>1</sup> See section 2.1.3 for a general background on this family of materials.

<sup>2</sup> See section 4.2 for a description of the apparatus used.

In previous scanning thermal microscopy measurements of the same samples, it was shown that the InSe had a reduced thermal conductivity where it was bent over the pillars and at the edges of the holes [42].

Two possible explanations for this are that tensile strain [186, 187] and different substrates [188, 189] are known to affect the thermal conductivity of InSe.

As strain also affects both the phonon frequencies and bandgap energy [185, 190, 191], Raman and PL spectroscopy are well suited to investigating whether either of these effects is more likely.

### 7.1 The Raman spectrum of indium selenide

In comparison to graphene, the Raman spectrum of InSe is characterised by lower frequency peaks and a lower signal level, which makes extracting information by fitting curves more complicated. Figure 7.1 shows an example Raman spectrum taken from  $\sim 12$  nm-thick InSe, with the visible peaks labelled according to their group theory descriptions [191].

The two most prominent peaks are the  $A_1'(\Gamma_1^2)$  and  $A_1'(\Gamma_1^3)$  peaks at  $\sim 115$  and  $\sim 230$   $\text{cm}^{-1}$ , and I will focus on these for the rest of this chapter. Between them, there are two lower intensity peaks labelled  $E''$  and  $A_2''$ .<sup>3</sup> Due to their low signal level it is hard to extract quantitative information from these, but as they are close to peaks of interest, they must still be accounted for when fitting.

Below  $\sim 105$   $\text{cm}^{-1}$ , there is a region of suppressed signal caused by the notch filter which removes Rayleigh scattering at the laser frequency.<sup>4</sup> This is very close to the Raman shift of the  $A_1'(\Gamma_1^2)$  peak, so it must also be taken into account in the fit.

To determine the notch filter behaviour I fit a logistic function to a flat background spectrum from taken from the substrate. The fitting function used was

$$I_{\text{Raman}} = I_{bg}N(\omega; \omega_N, \Gamma_N) + q_n, \quad (7.1)$$

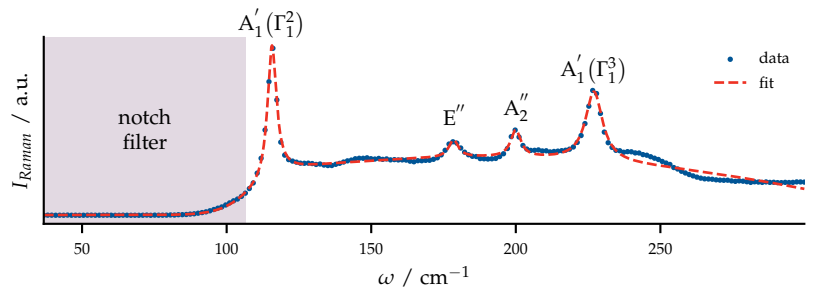
$$N(\omega; \omega_N, \Gamma_N) = \frac{1}{1 + e^{-\frac{\omega - \omega_N}{\Gamma_N}}},$$

with free parameters  $I_{bg}$  for the background amplitude;  $\omega_N$  and  $\Gamma_N$  for the frequency and width of the notch filter,  $N(\omega)$ ; and  $q_n$  to account for detector noise introduced after the filter. From this fit I was

<sup>3</sup> I have omitted their full description in the figure: the peak marked  $A_2''$  is technically  $A_2''(\Gamma_1^1)$  and the peak marked  $E''$  is the degenerate combination of  $E''(\Gamma_3^1)$  and  $E''(\Gamma_3^3)$ .

<sup>4</sup> See chapter 4 for more detail on Raman spectroscopy and why this filter is needed.

Figure 7.1: The Raman spectrum of InSe, taken from the  $\sim 12$  nm-thick flake discussed in section 7.3. Peak assignments are based on reference [191].



able to extract values for the cutoff frequency of  $\omega_N = 106.8 \text{ cm}^{-1}$ , and width of  $\Gamma_N = 5.5 \text{ cm}^{-1}$ . These could then be used as constants in all subsequent Raman fits.

The fitting function I used for Raman in the rest of this chapter is then given by

$$I_{Raman} = N(\omega) \left[ \left( \sum_{i=1}^4 L(\omega; I_i, \omega_i, \Gamma_i) \right) + I_{bg}(\omega; q_0, q_1, q_2) \right] + q_n,$$

$$L(\omega; I_i, \omega_i, \Gamma_i) = \frac{I_i}{1 + 4 \left( \frac{\omega - \omega_i}{\Gamma_i} \right)^2}, \quad (7.2)$$

$$I_{bg}(\omega; q_0, q_1, q_2) = q_2 \omega^2 + q_1 \omega + q_0,$$

where  $N(\omega)$  is the predetermined notch filter function;  $L(\omega)$  is a Lorentzian peak with height, Raman shift and full width at half maximum (FWHM)  $I_i$ ,  $\omega_i$  and  $\Gamma_i$ ;  $I_{bg}(\omega)$  is a quadratic background with coefficients  $q_0$ ,  $q_1$  and  $q_2$ ; and  $q_n$  once more accounts for detector noise introduced after the filter.

An example fit using this function is shown in figure 7.1.

## 7.2 Sample A: indium selenide on pillars

Sample A consists of a  $\sim 45 \text{ nm}$ -thick flake of InSe on a  $\text{SiO}_2$  substrate patterned with an array of PMMA micropillars. An optical image of the sample can be seen in figure 7.2.

The pillars were created by transferring an InSe flake onto an array of holes with a PMMA membrane.<sup>5</sup> The membrane was left on the substrate and cleaned away with solvents, during which some of the dissolved PMMA was drawn into the holes to create pillars. From atomic force microscopy (AFM) measurements, we know the resulting pillars have an average height of  $\sim 16 \text{ nm}$ , a width of  $1 \mu\text{m}$ , and that they exist even in the holes which were covered by InSe [42].

The result of the pillars is that the InSe flake has an out-of-plane deformation, as shown by the cross-section diagram in figure 7.3. This can be expected to induce strain to the InSe, which can be probed with optical spectroscopy.

### 7.2.1 Raman characterisation

A Raman datacube was collected from the area indicated in figure 7.2, and the function in equation 7.2 was fit to every spectrum. The results of this are shown in figure 7.4.

Figures 7.4 (a) and (b) show the peak area,  $A$ , for the  $A_1'(\Gamma_1^2)$  and  $A_1'(\Gamma_1^3)$  peaks.<sup>6</sup> The PMMA pillars can be seen in the maps as circular areas with a reduced intensity for both peaks. There is also an increase in the peak intensity at the flake edges.

Figures 7.4 (c) and (d) show the corresponding Raman shift,  $\omega$ , for each peak. For tensile strained InSe we should expect a red shifting of the Raman peaks [185, 190, 191], however we observe very little shift at all. The noisy appearance of the images is a reflection that

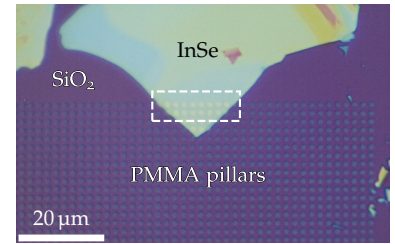


Figure 7.2: Optical image of indium selenide on pillars. The white dashed rectangle marks the location of the Raman and PL scans shown in figures 7.4 and 7.5.

<sup>5</sup> See section 2.2.3 for details of a very similar transfer process.

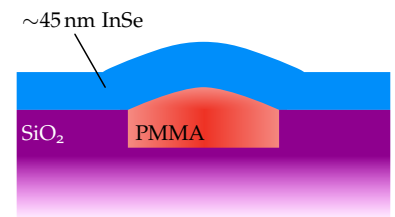
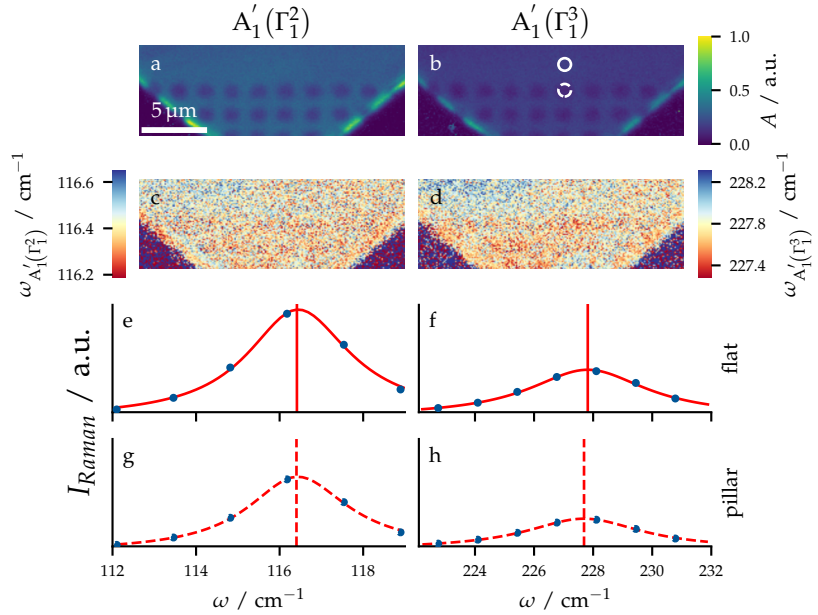


Figure 7.3: Cross-section of InSe on a PMMA pillar. Not to scale.

<sup>6</sup> In this chapter I generally plot peak area,  $A$ , rather than peak height  $I$ , for images showing Raman peak intensity. This is because when the signal-to-noise ratio (SNR) is low, the negative fitting covariance between a peak's height and width,  $\Gamma$ , can make height images very noisy. But as  $A \propto I\Gamma$ , area images are less susceptible to this noise.

Figure 7.4: Raman mapping of InSe on pillars. (a, b) Maps of peak area for the  $A'_1(\Gamma_1^2)$  and  $A'_1(\Gamma_1^3)$  peaks. (c, d) Corresponding maps of the peak centres. (e-h) Zoom in of spectra averaged over the regions indicated in (b) for flat and pillar regions. Blue points show the experimental measured data, red lines show fits to that data and vertical lines show the determined peak centres. Line styles are set to match those in (b).



any peak shifting that occurs is comparable to the noise floor of the spectral shifts we are able to resolve.

To visualise the peak stability in a different way, figures 7.4 (e) and (f) show the  $A'_1(\Gamma_1^2)$  and  $A'_1(\Gamma_1^3)$  peaks from an area of flat InSe, averaged from within the solid circle in figure 7.4 (b), and figures 7.4 (g) and (h) show the peaks from an area of bent InSe, averaged from within the dashed circle.

Blue points show the measured data points, and red lines show the curves found by fitting to the data.<sup>7</sup> The vertical lines indicate the Raman shift of each peak found by the fit, and it is clear that there is almost no position change between the flat InSe and the InSe bent by a pillar.

This is an indication that any strains induced to the InSe are small enough that they have little effect on the spectral properties. The relative thickness of the flake compared to the deformation may give some explanation for this behaviour.

From the lack of observed strain, I conclude that the reduced peak intensity seen at the pillars is due to a reduction in the general back-scattered intensity, caused by the differing optical properties of SiO<sub>2</sub> and PMMA.

### 7.2.2 Photoluminescence characterisation

Another way to probe the strain in InSe is to use PL spectroscopy. With increased tensile strain, we should expect a reduction of the bandgap energy and a consequent reduction in the energies of the PL peaks [185, 190, 191].

The  $\sim 45$  nm thickness of sample A means it can be treated as bulk

<sup>7</sup>It may be tempting to look at the spacing of data points in the spectra and conclude that we can't resolve peak shifts smaller than that spacing. However by fitting to the peaks we can achieve a much finer resolution, as the tails of a peak will span across multiple points. The resolution of a peak position found through fitting is known as spectral shift resolution, and is quoted by the manufacturer of our Raman microscope to be  $\ll 0.1 \text{ cm}^{-1}$ , however the true value will also depend on the SNR and the peak lineshape.

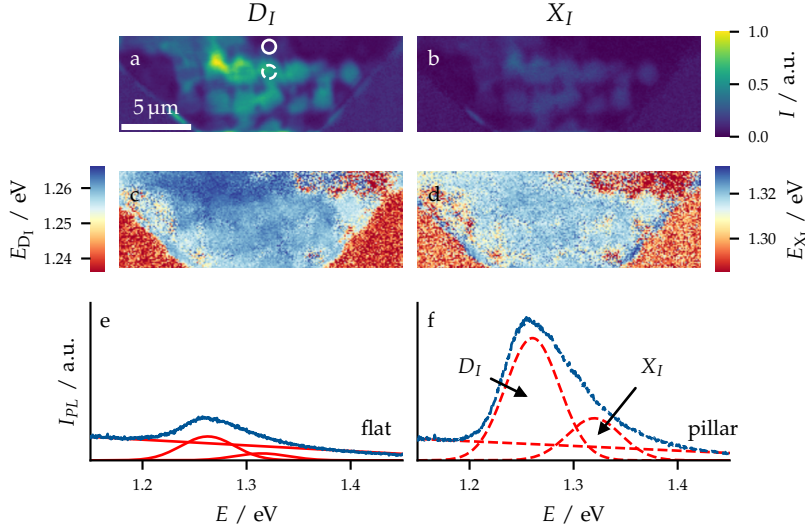


Figure 7.5: PL mapping of InSe on pillars. (a, b) Maps of peak area for the  $D_I$  and  $X_I$  peaks. (c, d) Corresponding maps of the peak centres. (e, f) Zoom in of spectra averaged over the regions indicated in (a) for flat and pillar regions. Blue points show the experimental measured data, red lines show fits to that data and vertical lines show the determined peak centres. Line styles are set to match those in (a). Peaks are drawn without including the background, which is drawn separately.

InSe, so to fit to the measured PL spectra I use the function

$$I_{PL} = G(E; I_{D_I}, E_{D_I}, \Gamma) + G(E; I_{X_I}, E_{X_I}, \Gamma) + I_{bg}(E; q_0, q_1),$$

$$G(E; I_i, E_i, \Gamma_i) = I_i 2^{-\left(\frac{2(E-E_i)}{\Gamma_i}\right)^2}, \quad (7.3)$$

$$I_{bg}(E; q_0, q_1) = q_1 E + q_0,$$

where  $G(E)$  is a Gaussian peak with height, centre and FWHM  $I_i$ ,  $E_i$  and  $\Gamma_i$ ; and  $I_{bg}(\omega)$  is a linear background with coefficients  $q_0$  and  $q_1$ .

There are two Gaussian components in this equation. The first accounts for a resonance at  $\sim 1.26$  eV, which is generally attributed to defect-bound excitons, and I shall refer to this as  $D_I$ . The second accounts for a resonance at  $\sim 1.33$  eV, which is generally attributed to exciton recombination across the bandgap, and I shall refer to this as  $X_I$  [192]. Following the example of reference [193], I constrained both peaks to have the same FWHM.

I collected a PL datacube from the same area as the Raman datacube shown above and the results of fitting equation 7.3 are shown in figure 7.5. This includes maps of peak intensity and position, and example spectra from a flat and bent area, as was shown for the Raman scan.

Figures 7.5 (a) and (b) reveal that the intensity of both PL components is enhanced at the pillar locations. There is also an enhanced area at the upper left of the image, which overlaps both pillar and flat regions.

Figures 7.5 (c) and (d) reveal that once again, we don't see a significant peak shifting. This supports the conclusion gathered from the Raman analysis that the pillars do not significantly strain the InSe, so we must look for another explanation for the enhanced PL.

Recently, Mazumder et al. reported an enhancement of PL emission from InSe transferred onto Si pillars [191]. They attributed this to a breakdown of the selection rules governing which excitonic res-

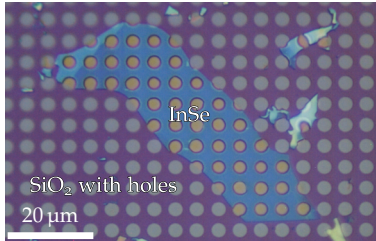


Figure 7.6: Optical image of indium selenide on holes.

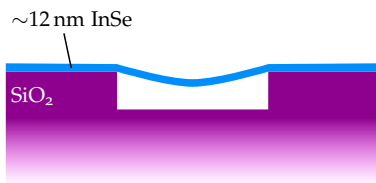


Figure 7.7: Cross-section of InSe suspended over a hole patterned in SiO<sub>2</sub>. Not to scale.

onances can be excited by linearly polarised light, caused by geometric deformations rather than strain. This is also a likely explanation for the bright PL from our PMMA pillars.

I leave this section with one final note, which is that all the PL and Raman measurements in this chapter were carried out at room temperature. For PL, this can make peak assignments complicated because the peaks we see at room temperature may be composed of multiple different resonances with overlapping linewidths. For more definitive conclusions to be drawn from PL, it is helpful to go to low temperatures, where Fermi-Dirac broadening is minimised meaning individual components can be more readily identified.

### 7.3 Sample B: indium selenide on holes

Sample B consists of a  $\sim 12$  nm-thick flake of InSe on a SiO<sub>2</sub> substrate patterned with an array of holes. An optical image of the sample can be seen in figure 7.6.

This sample was created in a similar fashion to sample A, except that the PMMA membrane was lifted away from the substrate rather than being cleaned away with solvents. From AFM measurements, we know that the InSe is suspended over the holes, which have a diameter of 3  $\mu\text{m}$ , and doesn't touch the bottom [42].

The resulting structure is shown by the cross-section diagram in figure 7.7. We can expect high strains at the edges of the suspended region.

#### 7.3.1 Raman characterisation

A Raman datacube was collected from an area spanning two holes in sample A, and the function in equation 7.2 was fit to every spectrum. The results of this are shown in figure 7.8.

Figures 7.8 (a) and (b) show the peak area,  $A$ , for the  $A_1'(\Gamma_1^2)$  and  $A_1'(\Gamma_1^3)$  peaks. The holes can be seen in the maps by their reduced intensity for both peaks. The elliptical appearance of the holes was caused by lateral drifting of the sample during the scan.

Figures 7.8 (c) and (d) show the corresponding Raman shift,  $\omega$ , for each peak. At the edges of the holes, we can see a significant red shifting of the Raman peaks, which indicates that these areas are indeed more tensile strained as we had expected [185, 190, 191]. In the suspended regions, the peak centre maps lose spatial coherence, which indicates that the SNR is too low to reliably determine peak position from fitting to the individual spectra.

To improve the SNR I took averages of the spectra from the regions shown by the ellipses in 7.8 (b). These are representative regions of the supported InSe, outlined by a dashed and dotted line; the edge of the hole, enclosed between the two dashed lines; and the suspended InSe, outlined with a solid line.

The resulting spectra are shown in figures 7.8 (e-j). As in section 7.2.1, the vertical lines indicate the Raman shift of each peak found

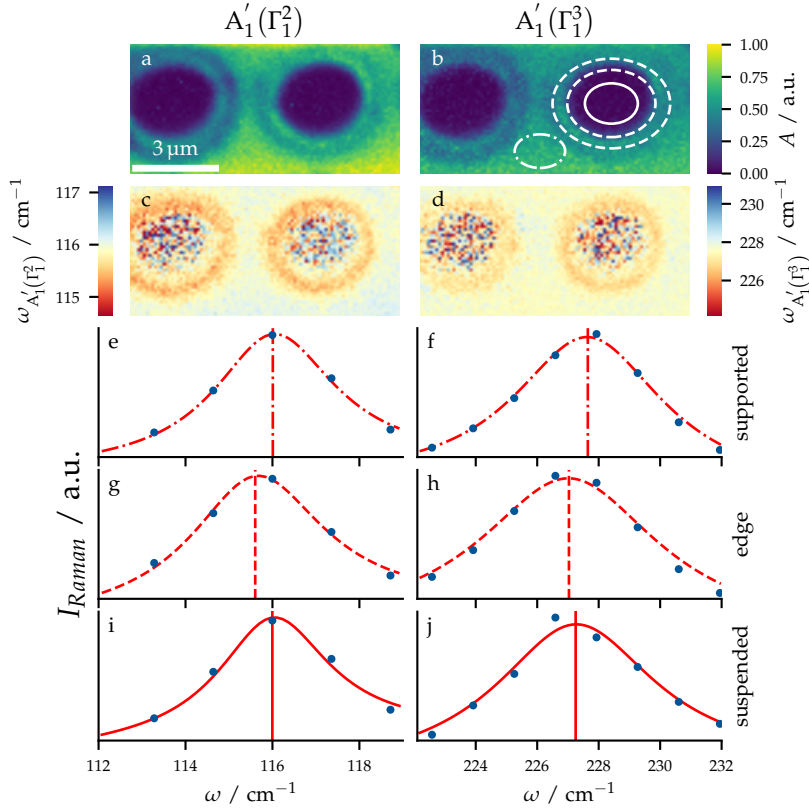


Figure 7.8: Raman mapping of InSe on holes. **(a, b)** Maps of peak area for the  $A'_1(\Gamma_1^2)$  and  $A'_1(\Gamma_1^3)$  peaks. Ellipses indicate the areas from which the spectra in (e-j) were averaged. **(c, d)** Corresponding maps of the peak centres. **(e-j)** Zoom in of spectra averaged over the regions indicated in (b) for supported, edge and suspended regions. Blue points show the experimental measured data, red lines show fits to that data and vertical lines show the determined peak centres. Line styles are set to match those in (b).

by fitting. As we observed in the images, there is a redshift at the edges compared to the supported InSe of  $\sim 0.40$  and  $\sim 0.65 \text{ cm}^{-1}$  for the  $A'_1(\Gamma_1^2)$  and  $A'_1(\Gamma_1^3)$  peaks.

Importantly, by averaging over the suspended region we are able to get a good enough SNR to reliably fit to the spectrum. Compared to the edge region, we see a slight blue shift, particularly for the  $A'_1(\Gamma_1^2)$  peak, which suggests that the greatest strain in the material is located at the edges of the holes.

There are some factors we must consider here to assess whether conclusions drawn from averaging over a low-signal region like this are valid. Usually the spot size of our Raman microscope is  $\sim 450 \text{ nm}$  in FWHM, which means that spectra from the centre of a  $3 \mu\text{m}$  region like these holes should have minimal overlap with spectra from the edge. However, as the signal is very low for the suspended InSe, there will be a proportionally greater amount of Raman signal from the edges of the acquisition area.

Thankfully, I note that the closest points to the suspended region with a good SNR are the points at the edge which were red shifted compared to the flat InSe. The fact that we see a relative blue shift indicates that we must have a significant contribution from the suspended InSe, and that the true blue shift may be even higher.

### 7.3.2 Photoluminescence characterisation

I collected a PL datacube from a different area of sample A, also spanning two holes.

As sample B is  $\sim 12$  nm in thickness I fit it with the function

$$I_{PL} = G(E; I_i, E_i, \Gamma_i) + I_{bg}(E; q_0, q_1), \quad (7.4)$$

which consists of a single Gaussian and a linear background. This has shown to be a good match for the PL spectrum of  $\sim 12$  nm InSe from literature [193]. The definition of the Gaussian function is unchanged from the one shown in equation 7.3.

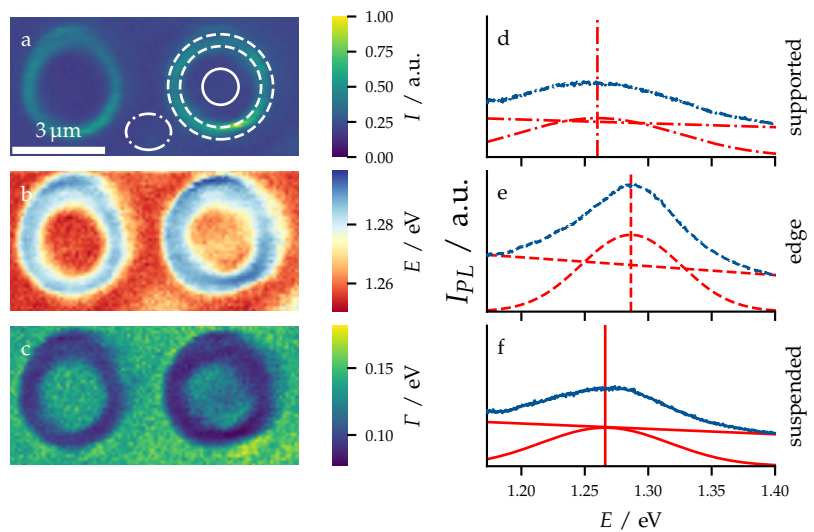
The parameter maps and representative spectra shown in figure 7.5.

We see that the edges of holes are typified by an increased peak intensity, a blue shifting of the peak energy and a narrowing of the peak linewidth. This blue shift is in fact the opposite trend to what would be expected for tensile uniaxial strain [185, 190, 191].

For this reason it seems likely that the dominant effect governing changes in the PL spectrum of this sample is once again geometrical factors rather than strain [191]. It may be that what appears as a blue shift of the peak energy at room temperature is actually an activation of a previously forbidden higher energy resonance by the curvature of the flake. Low temperature measurements may be better able to distinguish between these two scenarios because of the reduced linewidths of the peaks, which could lessen the overlap between resonances.

I note that the peak energy for the supported InSe, at  $\sim 1.27$  eV, is lower than the  $\sim 1.3$  eV that would be expected for a 12 nm flake at room temperature [40]. I attribute this to a photoinduced oxidation of the InSe [194].

Figure 7.9: PL mapping of InSe on holes. **(a-c)** Maps of peak height, centre and FWHM **(d-f)** Zoom in of spectra averaged over the regions indicated in (a) for supported, edge and suspended regions. Blue points show the experimental measured data, red lines show fits to that data and vertical lines show the determined peak centres. Line styles are set to match those in (a). Peaks are drawn without including the background, which is drawn separately.



### 7.3.3 Probing light-induced oxidation of indium selenide

To probe this further, I took a time-resolved PL measurement from an area of supported InSe in sample B that I hadn't measured before. I used the same laser power which I used to acquire the images above, which was  $\sim 85 \mu\text{W}$ , and I recorded 130 consecutive 1 s exposures. The resulting spectra are shown in figure 7.10 (a), with the darkest colours representing the earliest spectra.

It is apparent that as the laser exposure goes on, the intensity of the initial PL signal decreases, and the peak energy is red shifted. To show this more quantitatively I fit function 7.4 to every spectrum and plotted the normalised intensity and peak energy as a function of time in figures 7.10 (b) and (c). Over the course of the 130 s we see a fast threefold reduction in the intensity, and we see the energy of the PL decrease from the expected value at  $\sim 1.3 \text{ eV}$  to the value observed in the images above,  $\sim 1.27 \text{ eV}$ .

This is clear evidence that we are indeed seeing photoinduced oxidation, but there is still a puzzle left to solve. The spectra in the PL datacube taken above only used a 3 s exposure time, though we have seen that it takes  $\sim 130 \text{ s}$  for the oxidation to reduce the peak energy to the observed value. The reason for this is that the Raman datacubes were deliberately oversampled to yield a better image quality: the spot size of the measurement is  $\sim 450 \text{ nm}$ , but each spectrum in the map is only 100 nm away from its neighbours. This means that there is a significant overlap between consecutive exposures which significantly increases the effective time that each area of InSe is exposed to the laser.

I used the same exposure settings for both Raman and PL, which means we can therefore also expect oxidation to have occurred during the Raman acquisition. To quantify any effects that this may have, I performed a time-resolved Raman measurement using the same methodology as for the PL. The results of this are shown in figure 7.11.

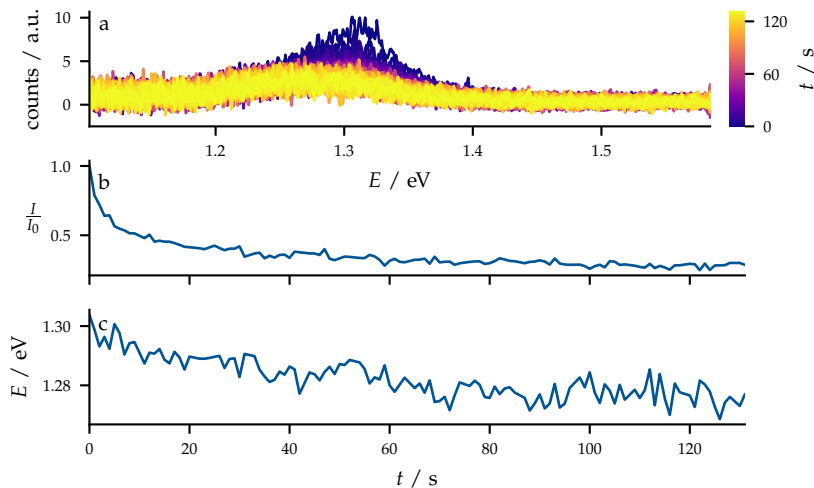
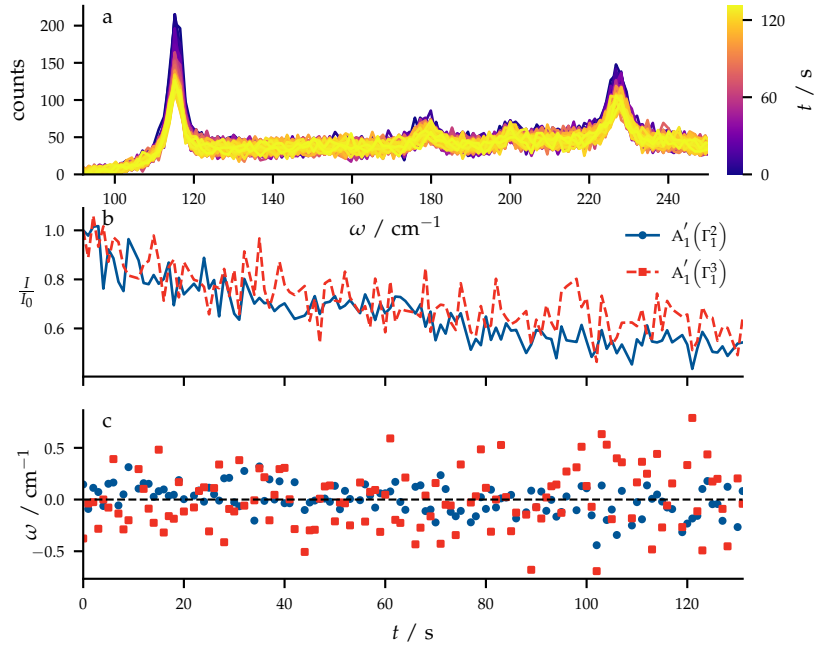


Figure 7.10: Time-resolved PL of InSe. **(a)** A series of 130 consecutive 1 s PL exposures taken from a single spot on the supported InSe. The colour of each spectrum is mapped to its starting time relative to the start of the measurement series, with darker lines showing earlier measurements. **(b)** The amplitude of a single Gaussian peak fit to each spectrum from (a) as a function of time, found from fitting equation 7.4 to the data shown in (a). **(c)** The corresponding peak energy of the same peak as a function of time.

Figure 7.11: Time-resolved Raman of InSe. **(a)** A series of 130 consecutive 1 s Raman exposures taken from a single spot on the supported InSe. The colour of each spectrum is mapped to its starting time relative to the start of the measurement series, with darker lines showing earlier measurements. **(b)** The amplitude of the  $A_1'(\Gamma_1^2)$  and  $A_1'(\Gamma_1^3)$  peaks relative to their starting amplitude as a function of time, found from fitting equation 7.2 to the data shown in (a). **(c)** The corresponding shifts of the same peaks from their mean positions, 115.35 and 227.25  $\text{cm}^{-1}$ , as a function of time.



During the time-resolved measurement, we observe a decrease in the intensity of both  $A_1'(\Gamma_1^2)$  and  $A_1'(\Gamma_1^3)$ . However unlike for the PL peak, the decay is roughly linear with time, and we don't observe any frequency shifting of the Raman peaks.

#### 7.4 Conclusions

I used Raman and PL spectroscopy to investigate strains in two InSe samples.

In sample A, the  $\sim 45$  nm thickness means that the PMMA nanopillars did not induce a significant strain that we could detect with Raman spectroscopy. This is good evidence that the decrease in thermal conductivity observed at the pillars [42] is related to the difference in the substrate [188, 189]. Nevertheless, we observed clear PL signatures which I attribute to relaxation of the selection rules governing excitonic resonances by geometric deformations to the material [41].

In sample B, we did observe clear signatures of tensile strain via Raman, at the edges of the holes where the drop in thermal conductivity was observed [42]. This suggests that strain plays a significant factor in the thermal conductivity of the thinner  $\sim 12$  nm sample, in line with previous reports [186, 187]. We also observed a distinct PL spectrum, characterised by an apparent blue shift of the PL energy and an increase in intensity. As this is the opposite behaviour to that expected for strained InSe, I once more attribute this to geometric effects caused by the deformation around the patterned substrate, rather than strain.

Finally in the thinner sample, we observed clear signs of oxidation caused by laser induced heating [194]. This may be exacerbated by the reduced thermal mass compared to the bulk material, but is

also further evidence of the anomalously low thermal conductivity of InSe compared to other vdW materials [42].

On top of their significance for InSe, the results from sample B are clear evidence that nanoscale strains, like those studied in chapters 5 and 6, can be induced controllably in sufficiently thin vdW materials by substrate engineering.



## 8

# *Data cluster analysis of twisted bilayer graphene*

In chapters 5 and 6 of this thesis I showed how nanoscale features of van der Waals (vdW) heterostructures, such as fractures, folds and bubbles, induce highly localised variations to the materials' optoelectronic properties. These could be exploited in devices, but the fact that they typically appear stochastically means that time spent searching for desired features could become a major bottleneck in the fabrication process. In the previous chapter I showed one approach to surmounting this problem, by trying to recreate the stochastic features using controllably engineered substrates. An alternative approach would be to find a way to automate the analysis and identification of such features. In this chapter I address an analogous problem: analysing and identifying different types of twisted bilayer graphene (TBLG) from a sample with a stochastic distribution of twist angles.

I demonstrate different approaches to how data clustering, a machine learning tool, can be applied to Raman datacubes for this purpose. I use the Gaussian mixture model (GMM) algorithm to highlight areas with particular twist angles, from a sample with a wide range of orientations. I then show that once the model has been trained, it can be reapplied to new data to assess the similarity between the new materials and the ones previously identified. This has potential to fast-track the prototyping of TBLG devices, by allowing fully computerised detection of particular twist angles from automated large-area scans.

This project came about during the coronavirus pandemic that began in 2020. When the lockdown blocked our access to the lab, we had to find new ways to carry on our research from home. So I began to investigate whether machine learning could reveal any new information from previously collected data. Thankfully, data clustering turned out to be both interesting to study and successful. It revealed features of our TBLG, which I hadn't appreciated from traditional Raman analysis alone.

I have prepared a manuscript based on the work in this chapter, *Data cluster analysis and machine learning for classification of twisted bilayer graphene*, which is currently submitted to the journal Carbon

(see [Dissemination](#)). I'm grateful to our collaborators at Kyushu University in Japan, Kenji Kawahara and Professor Hiroki Ago, who fabricated the TBLG I studied in this chapter.

The demonstration of superconductivity in TBLG [9] sparked a flurry of new research into this material [30, 195–201]. It is formed of two sheets of single layer graphene (SLG) stacked together, with one lattice rotated relative to the other. Interference between the two lattices adds an extra moiré superlattice potential, whose period depends on the twist angle. This modifies the electronic band structure of the bilayer graphene (BLG), leading to novel properties such as enhanced photocurrent generation [202], superconductivity [9, 46] and correlated insulating phases [28, 195] at particular twist angles. With the advent of twist engineering, bilayer graphene has expanded from a single material to a whole family of materials with continuously tunable properties. More recently, twist engineering has been applied to bilayers and heterobilayers of other two-dimensional (2d) materials, demonstrating its wider applicability beyond graphene [203–206].

However fabricating TBLG samples is a highly time and labour-consuming process. The most common method used is the 'tear and stack' technique [9, 46, 75], which involves manually picking up and rotating flakes before depositing them. These samples have a tendency to relax into twist angles other than those intended [9], due to the varying interlayer potential associated with different twist, so methods to accurately determine the twist angle are vital. Existing methods, including Raman spectroscopy [102–105], transmission electron microscopy [102] and low energy electron diffraction [105], are inherently laborious and need highly-specialised human input for data interpretation.

A recent theoretical work by Sheremetyeva et al. reviews the performance of several different machine learning algorithms – kernel ridge regression, random forest regression and a multilayer perceptron neural network – for identifying twist angle from the Raman spectra of bilayer graphene [207]. They use simulated Raman spectra, focused on the G peak of graphene, as a training dataset, which has the advantage that they can generate spectra covering the whole 30°-range of possible twist angles. However a downside of this approach is that it doesn't account for experimental factors, such as spectral broadening and resonant Raman processes at certain twist angles.

In this chapter, I explore new analysis techniques for Raman spectroscopy data acquired from a TBLG sample with a wide range of different twist angles. Firstly, I present a manual analysis to identify features in the Raman spectra associated with particular twist angles. I then apply a data clustering technique, the GMM. I demonstrate a priori application of the technique to identify distinct material types within Raman maps, showing that it can identify the same key regions found by human analysis, and that it can provide further statistical information on features such as strain in the graphene. I then

show that once a model has been trained on an area of interest, it can be used to successfully categorise new regions of TBLG in terms of similarity to desired twist angles.

I present two approaches to dimensionality reduction of the Raman spectra: first by using parameters returned by fitting peaks to the data, and then by using principle component analysis (PCA). By doing this, I demonstrate that data clustering has the potential to enable high-throughput classification of TBLG, by allowing computerised detection of particular TBLG species from automated large-area scans.

### 8.1 Sample characteristics

The TBLG sample used in this work consists of two batches of chemical vapour deposition (CVD) graphene, which were transferred to the same  $\text{SiO}_2$  substrate, as shown in figure 8.1. Batch 1 is formed of hexagonal, single-layer grains on the order of tens of microns in lateral size, with a stochastic distribution of orientations. Batch 2 is formed of larger single-layer grains on the order of hundreds of microns in lateral size, with a single dominant alignment. Batch 1 sits on top of batch 2, and the areas where the two batches overlap form TBLG, with a stochastic distribution of twist angles.

An optical microscope image of a representative area of the sample is shown in figure 8.2.

A key advantage of this fabrication process is that we can infer the orientation of the graphene lattice from the angle of the hexagonal grain edges, which gives us a reasonable estimation of the TBLG twist angle,  $\theta_t$ . I use the shorthand  $\text{TBLG}_\theta$  to refer to TBLG with an estimated angle  $\theta$ . The edges are not perfectly straight, which leads to an uncertainty on the order of  $\pm 1^\circ$ .

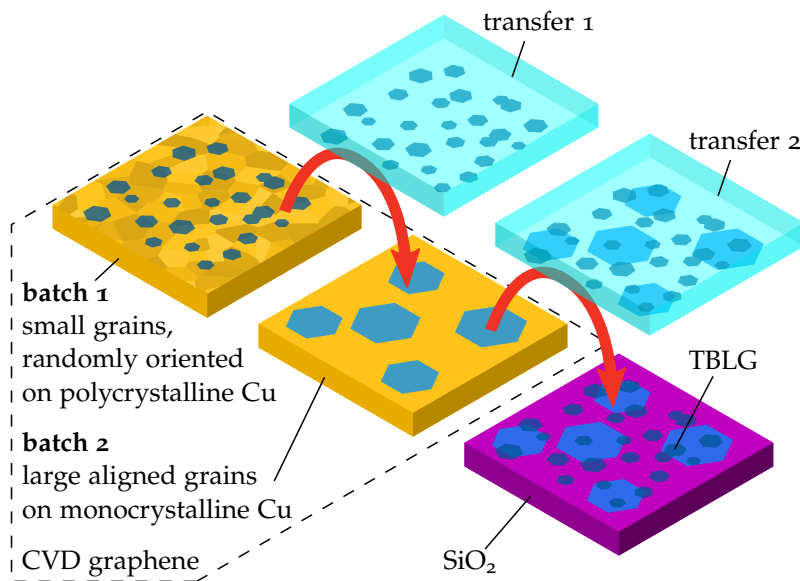
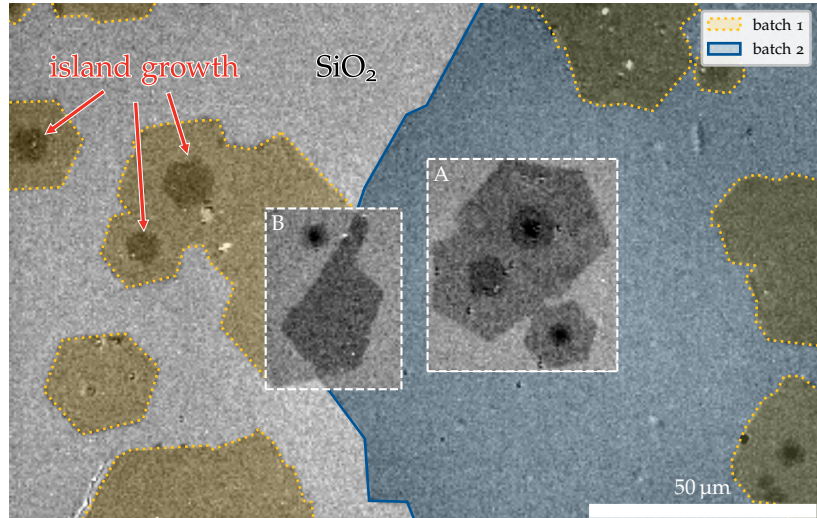


Figure 8.1: Fabrication process. Randomly oriented (batch 1) and aligned (batch 2) graphene grains are grown on polycrystalline Cu foil and  $\text{Cu}(111)$  film respectively, then transferred to the same  $\text{SiO}_2$  substrate.

Figure 8.2: Optical microscope image showing resulting sample, with areas of TBLG formed by overlapping graphene batches. Regions A and B, focused on in the rest of this work, are indicated with white rectangles. Randomly oriented grains from batch 1 are coloured yellow and outlined with dotted lines, a large grain from batch 2 is coloured blue and outlined with a solid line. No annotations are added within regions A and B to show the sample more clearly. Some multilayer islands are indicated with red arrows.



The grains of batch 1 feature several small patches of bilayer and multilayer graphene. These appear as darker areas in the optical image, towards the centre of some grains, and are highlighted by red arrows in figure 8.2. I shall refer to these patches as multilayer islands throughout this chapter. I stress that any bilayers which result from these islands are produced by a different mechanism to the artificially created bilayers formed by overlapping grains from batches 1 and 2, and as such we should not expect the same varied distribution of twist angles. By comparison, the grains in batch 2 are almost entirely free of multilayers.

In the rest of this work, I focus on two similar regions of the sample. Region A is used for training the data clustering models, and region B is used to test the pretrained models. The locations of these regions are shown in figure 8.2.

## 8.2 Raman analysis

Before we discuss data clustering, we first present a more traditional analysis, to explain the main Raman features of this TBLG sample.

### 8.2.1 Region A

A Raman datacube was collected from region A using the apparatus described in section 4.2.

Figure 8.3 (a) shows a set of representative Raman spectra taken from key areas. The dominant features of the graphene Raman spectrum are the G and 2D peaks, whose positions are shown at the top of figure 8.3 (a). I will analyse these peaks in terms of their intensity,  $I$ , Raman shift,  $\omega$ , and full width at half maximum (FWHM),  $\Gamma$ .

Figures 8.3 (b) and (c) show spatial maps of the 2D to G peak intensity ratio and the 2D peak FWHM. These are typical metrics used to indicate the quality and layer number of graphene [92]. The locations of the displayed spectra are indicated in these maps.

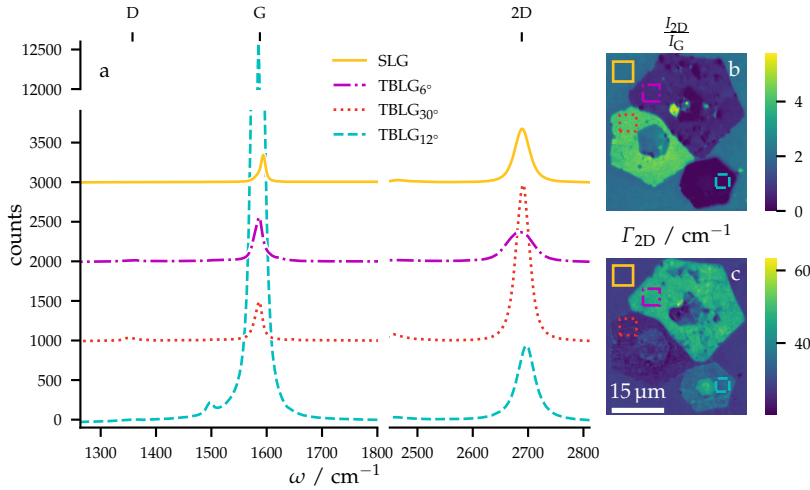


Figure 8.3: Raman features of twisted bilayer graphene: region A. (a) Representative averaged Raman spectra, showing large variation with twist angle. The averages were taken from within the squares of the corresponding colour and line style shown in (b) and (c). (b) Map of the 2D-to-G peak intensity ratio. (c) Map of the 2D peak FWHM.

The spectrum from the SLG has a 2D to G ratio of  $\sim 2$ , which is typical for monolayers on  $\text{SiO}_2$ . The graphene D peak, whose position is also indicated in figure 8.3 (a), and whose intensity correlates with defect density, is notably absent. This confirms that the graphene from CVD batch 1 is high quality and single layer, as designed.

There are three TBLG grains in region A, which can be seen clearly in figures 8.3 (b) and (c). As discussed above, I estimated the twist angles from the grain edge orientations to be  $6^\circ$ ,  $12^\circ$  and  $30^\circ$  using the optical image in figure 8.2. Figure 8.3 (a) shows that all three domains have a small D peak, which indicates that batch 2 has a slightly higher defect density than batch 1, though the D to G intensity ratio is generally low at  $< 0.1$ .

The  $\text{TBLG}_{6^\circ}$  spectrum has a broadened 2D peak and a 2D to G ratio of  $< 1$ . This is typical for graphene with a twist angle below  $\sim 10^\circ$  [103].

The  $\text{TBLG}_{30^\circ}$  spectrum has an enhanced 2D peak, and appears similar to the expected spectrum from SLG, which also matches predictions and observations for large twists from literature [102–104].

The  $\text{TBLG}_{12^\circ}$  spectrum has a strong ( $\sim 30\times$ ) enhancement of the G peak. This is caused by van Hove singularities (saddle points) in the superlattice band structure with a separation close to the energy of our excitation laser [102, 103, 105], which leads to a strongly resonant Raman process. For a 532 nm excitation laser, I calculate that this enhancement should occur for TBLG with a twist close to  $11.9^\circ$  [103], which is consistent with our estimated angle.

The maps also reveal that the multilayer islands at the centre of each grain have distinct Raman characteristics, and that some of them contain grain boundaries themselves.

A typical Raman analysis may involve comparing the parameters of many peaks, as demonstrated here. This can be a laborious process, which needs expert input, and often requires fitting many peaks to the collected data.

### 8.2.2 Region B

As for region A, a Raman datacube was collected from region B, and the results are shown in figure 8.4.

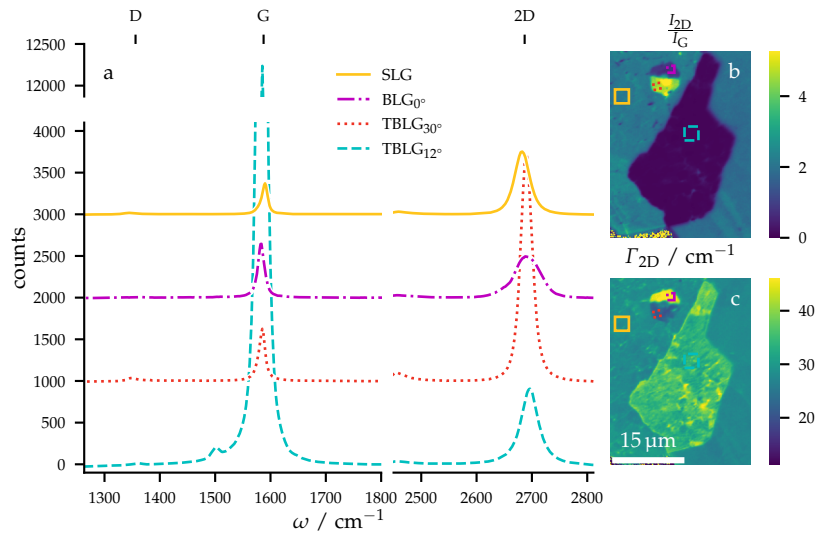
There are clear similarities between the two regions. Like region A, region B has domains composed of SLG, as well as TBLG<sub>12°</sub> and TBLG<sub>30°</sub>, identified by their grain edge orientations. As we should expect, the corresponding spectra shown in figure 8.4 (a) appear very similar to those in figure 8.3.

However there are also some differences which need to be considered. There is no TBLG<sub>6°</sub> present in region B, though there is a small patch of Bernal stacked bilayer, indicated by BLG<sub>0°</sub>, formed by island growth. The BLG<sub>0°</sub> and TBLG<sub>6°</sub> spectra, both shown with purple lines, appear superficially similar.

Whereas in region A all of the SLG came from the large batch 2 grain, in region B there is an area of batch 1 SLG on the left and an area of batch 2 SLG on the right. This is particularly evident from looking at the optical image in figure 8.2.

The final key difference is that, in region A all of the main TBLG domains identified were formed by stacking batches 1 and 2, but in region B the BLG<sub>0°</sub> and TBLG<sub>30°</sub> domains are due to island growth within batch 1.

Figure 8.4: Raman features of twisted bilayer graphene: region B. **(a)** Representative averaged Raman spectra, showing large variation with twist angle. The averages were taken from within the squares of the corresponding colour and line style shown in (b) and (c). **(b)** Map of the 2D-to-G peak intensity ratio. **(c)** Map of the 2D peak FWHM.



### 8.3 Mahalanobis normalisation

Data clustering algorithms compare the distance between points in an  $n$ -dimensional space, where each dimension is formed by a separate observation (for example  $I_{2D}/I_G$ ,  $\Gamma_{2D}$ ). However, the observations may have different units or variances, which could give unfair weighting to some observations over others. We therefore use Mahalanobis normalisation [208] to enforce that each dimension is unitless, has a mean of zero and has unit variance. In the rest of this

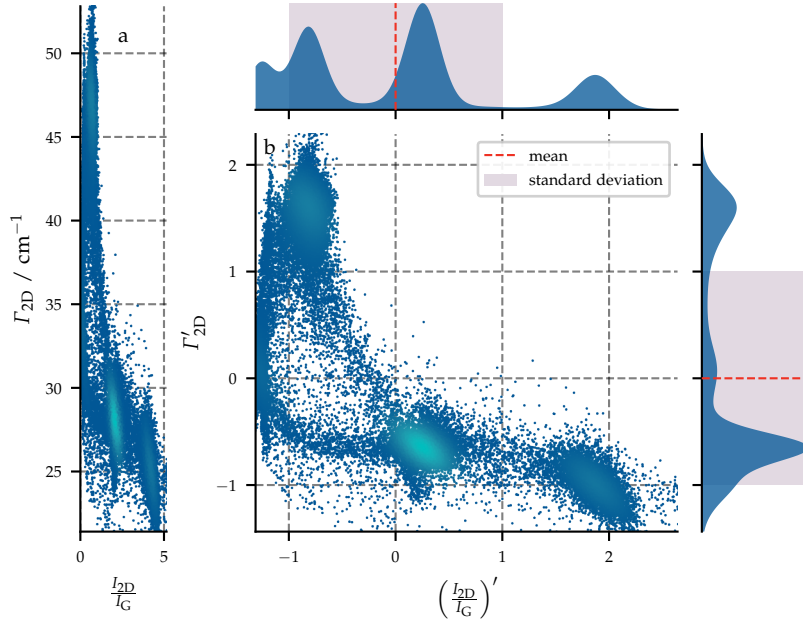


Figure 8.5: Mahalanobis normalisation. (a) Scatter plot of 2D peak FWHM against 2D-to-G ratio, from region A. (b) Mahalanobis normalised equivalent of (a), with added kernel density histograms for each axis. Both plots are drawn such that the scaling of the  $x$  and  $y$  axes are equal. Points are lightened according to their local density, so that the distribution can still be seen clearly even when points overlap.

work, for an arbitrary parameter  $p$ , I use the shorthand  $p'$  to denote its Mahalanobis normalised equivalent.

As an example to demonstrate the need for this normalisation, the FWHM of the 2D peak is plotted as a function of the dimensionless 2D-to-G ratio in figure 8.5 (a).<sup>1</sup> If we try to calculate the Euclidean distance between points in the resulting space, then the differences in  $\Gamma_{2D}$ , which has a standard deviation of  $\sigma_s \approx 8.4 \text{ cm}^{-1}$ , will dominate over the differences in  $I_{2D}/I_G$ , with its standard deviation of  $\sigma_s \approx 1.3$ . The bias between the two quantities would also change if  $I$ , for example, expressed  $\Gamma_{2D}$  in units of  $\text{m}^{-1}$  instead of  $\text{cm}^{-1}$ . But by Mahalanobis normalising both quantities, as shown in figure 8.5 (b), neither parameter is given unfair weighting in distance measurements.

#### 8.4 Gaussian mixture model

GMM is a data clustering technique which assumes a dataset is drawn from a set of  $N$  normally distributed clusters. It uses the expectation-maximisation algorithm [171] to find the means, covariance matrices and weightings of the  $N$  Gaussian probability distributions that best describe the data.

I use a two-dimensional example to illustrate the GMM fitting process. Figure 8.6 shows the peak shifts of the G and 2D peaks from region A. These shifts are often studied in SLG, because they reveal information about the strain and doping of a sample.<sup>2</sup> Figure 8.7 (a) is a scatterplot comparing the normalised equivalent quantities.

A GMM with  $N = 8$  Gaussian clusters was fit to the data shown, and the points were assigned a colour based on which of the resulting clusters they were most likely to belong to. Numbers next to each

<sup>1</sup> This is the same data shown in the maps in figure 8.3.

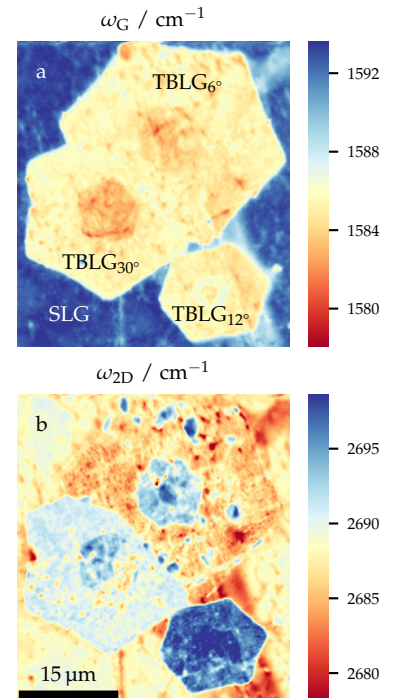
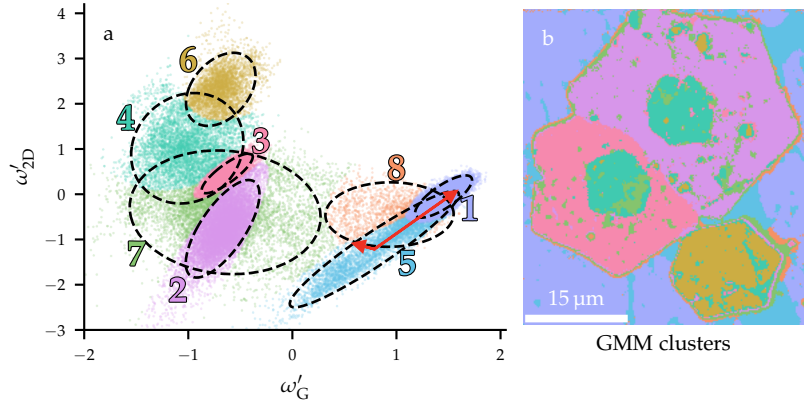


Figure 8.6: Unnormalised (a) G and (b) 2D peak shifts from region A. Twisted grains and single layer areas are indicated in (a).

<sup>2</sup> See chapter 5 for more detail on how this works.

Figure 8.7: Gaussian mixture model example. **(a)** Scatterplot of Mahalanobis normalised positions of the G and 2D peaks from region A. Points are coloured according to the cluster assigned to them by an 8-component GMM fit to the data shown. Black dashed lines show the  $2\sigma_s$  confidence ellipses for each cluster. Red arrows show the principal component vectors (scaled to  $2\sigma_s$ ) for cluster 5. **(b)** Key to cluster colour and spatial distribution.



cluster serve as labels and are ordered from the most (1) to the least (8) populated cluster. Confidence ellipses for each Gaussian cluster have also been added to figure 8.7 (a), to highlight the shape of the clusters. These are drawn at  $2\sigma_s$  away from the mean, where  $\sigma_s$  is the direction-dependent standard deviation.

In general, the positions and covariances of the identified clusters will depend somewhat on the number of clusters fit to the data. In this case, the value  $N = 8$  was chosen for the purpose of demonstration, based on the number of distinct colours that could be shown in a visualisation. There are certain techniques, such as Bayesian GMM, which can infer the number of clusters to use from the data itself [209], however these are beyond the scope of this work. For real-world applications, prior knowledge of the expected number of clusters can often be used to inform the choice of  $N$ .

Figure 8.7 (b) shows each coloured observation in the scatterplot mapped back to its original spatial position. This serves as a key to the colours, and shows that identified clusters correspond to the same distinct material types that I identified with the traditional Raman analysis above. There are clusters which account for all three kinds of TBLG (clusters 2, 3 and 6), as well as the island growth (cluster 4) and SLG (clusters 1 and 5). The width of each cluster is a reflection of the distribution of values within the cluster.

Note that the GMM has included some wide clusters with a low weighting (clusters 7 and 8), which account for observations that do not fit into any of the main clusters. These can be viewed as a background to the total probability density function. Points that are identified as belonging to these background clusters are few, and often localised at the spatial boundaries between materials, where the Raman spectra may have features of both materials present due to the finite beam size. Including these background-type clusters is possible because GMM explicitly accounts for overlapping distributions.<sup>3</sup>

It is interesting to note that the SLG has been split into two clusters (1 and 5), caused by small areas within the region with downshifted peak positions. I attribute this to variation in substrate interaction,

<sup>3</sup> This is a key advantage of GMM over other data clustering techniques such as  $k$ -means, which assigns observations to a cluster based on the closest cluster centre, and positions the centres to minimise the intra-cluster variance. A  $k$ -means fit to the same data as figure 8.7 is shown in figure A.4 for comparison.

which may induce both strain and doping to the graphene.

In single layer graphene, strain induces a linear shift of the G and 2D positions, whose gradient depends on the type and orientation of the strain [94, 108, 128]. I use eigendecomposition of covariance matrices, to find the principal component vectors for the SLG clusters. These vectors show the directions which correlate with most variance within a particular cluster.

Red arrows in figure 8.7 (a) show the principal components for a single cluster as an example. We can calculate the true gradients of these principal components by transforming them back into the unnormalised data space. If the origin of the peak shifting is solely due to strain, we should expect the gradient of the dominant principal component vector to lie in the range 2.02-2.44 [128]. For the highest weighted cluster, corresponding to majority of the SLG (cluster 1), we obtain a gradient of 2.02, but for the cluster corresponding to the downshifted SLG (cluster 5) we obtain a lower gradient of 1.69. This shows that the position shift cannot be explained by strain alone, and there is likely also a component of the variation induced by doping inhomogeneity [94, 108, 114, 128]. This is a good example of the analytical power of GMM, beyond simple material identification.

### 8.5 Classifying new data using a pretrained model

In this section, I show an example of a GMM trained on one area of the sample (region A) being used to identify similar materials in a new area (region B). Figure 8.8 (a) shows the clusters in region A identified by a three-dimensional GMM with  $N = 8$ , whose inputs are the intensity, position and width of the 2D peak.

To visualise the spatial distribution of the distinct material types identified, I plot the relative likelihood that a point is drawn from each Gaussian cluster in figure 8.9. The colours of the maps are chosen to correspond to the colour of the associated cluster in figure 4 8.8.

I assigned a label to each cluster, based on the traditional Raman analysis performed above, and on the twist angle estimated from the

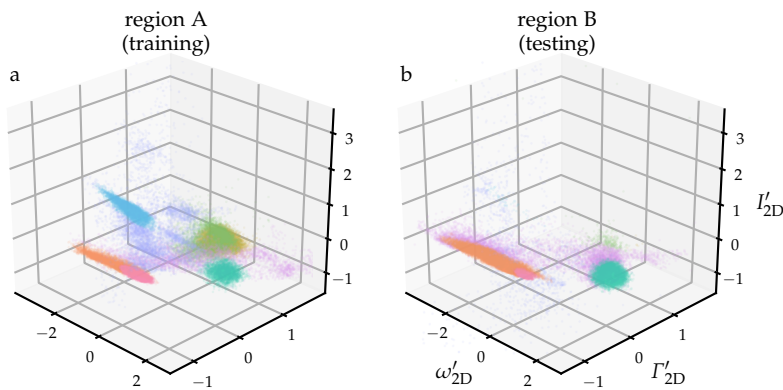
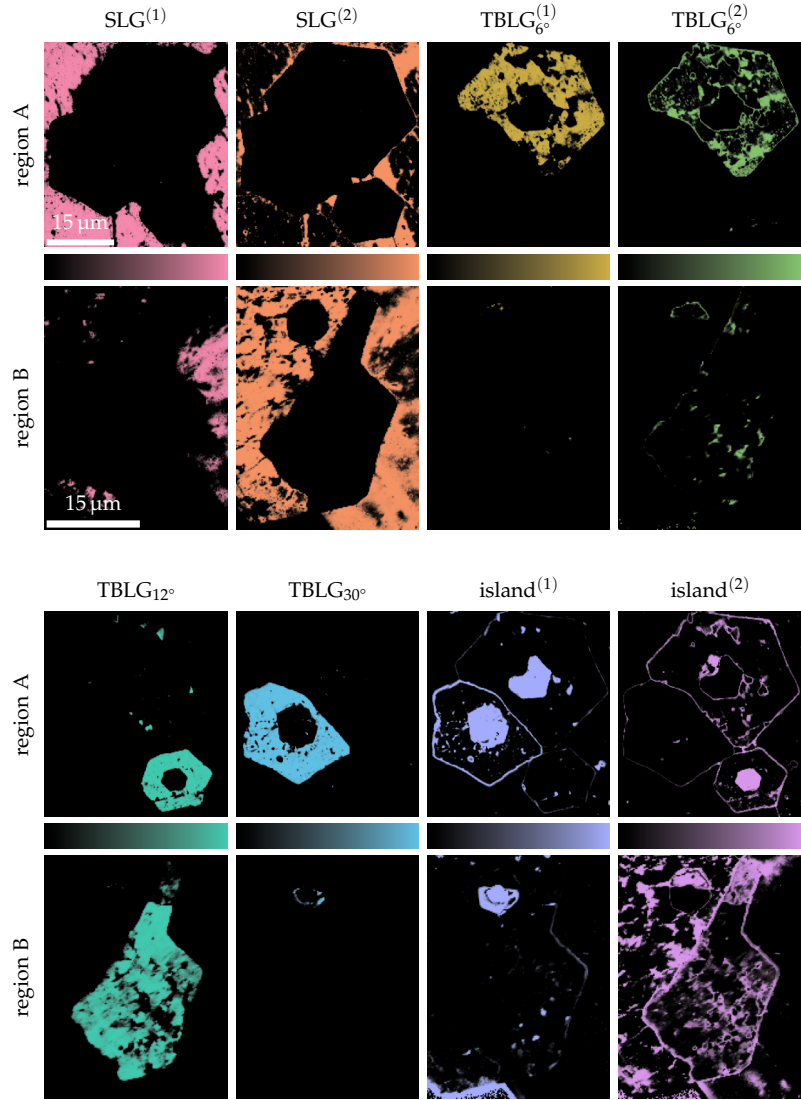


Figure 8.8: Classifying new data using pretrained clusters. (a) Scatterplot of Mahalanobis normalised intensity, position and width of the 2D peak from region A. Points are coloured according to the cluster assigned to them by an 8-component GMM fit to the data shown. (b) Corresponding scatterplot from region B, normalised using the same mapping as the data for region A. Points are coloured according to the cluster assigned to them by the same GMM previously fit to the data in region A.

Figure 8.9: 2D peak clustering and identification. Images show spatial maps of the relative likelihood that a point is drawn from each Gaussian cluster identified from fits to the 2D peak of region A, as shown in figure 8.8. The colours correspond to the associated figure 8.8 cluster. Labels assigned are based solely on analysis of region A.



optical image in figure 8.2. These are indicated at the top of figure 8.9.

We can see that the SLG is once again split due to strain- and charge-induced effects. We also see that the  $\text{TBLG}_{6^\circ}$  region has split into two clusters. This may be caused by small domains of locally relaxed twist angle, compared to the global twist of the whole grain [105]. Similarly, we see that there are two clusters corresponding to island growth, which can be attributed to domains with AB- and non-AB-stacked growth. Where multiple clusters have been assigned to one type of material in this way, I use superscript numbers in parentheses to refer to the individual clusters (for example  $\text{SLG}^{(1)}$  and  $\text{SLG}^{(2)}$ , for two distinct SLG clusters).

Once a model has been trained, and the desired materials have been labelled, the clusters can then be reapplied to new data, to judge how similar the new material is to the training material. I applied the model trained on region A to classify the data from region B

(indicated in figure 8.2).

To show the correspondence between similar values across the two regions, figure 8.8 (b) shows the intensity, position and width of the 2D peak from region B in the same normalised space as the region A data in figure 8.8 (a) (in other words, normalised to the mean and variance of region A).

The region B points were assessed according to the likelihood that they were drawn from the previously identified region A clusters and coloured accordingly. Where the 2D peak has similar characteristics to a region A cluster, the point falls in a similar location in the normalised space and so is identified as belonging to that cluster.

The spatial distributions of the identified materials from Region B are also shown in figure 8.9. This shows that the GMM has correctly identified the SLG in region B. Interestingly we see a reversal of the distribution of the two clusters from region A. In region B most points belong to the cluster marked  $SLG^{(1)}$ , whereas in region A most points were in the cluster marked  $SLG^{(2)}$ . This can be attributed to strain and doping variations between regions A and B. Note also that the SLG in the left of region B is from batch 2, whereas the SLG in the right, and in region A is from batch 1 (see figure 8.2). The cluster marked  $SLG^{(1)}$  only appears significantly in the batch 1 SLG. The cluster for the  $TBLG_{12^\circ}$ , and the island growth clusters have also correctly identified the same features from region B.

$TBLG_{6^\circ}$  is absent from region B so the corresponding maps are mostly empty. The map showing the  $TBLG_{30^\circ}$  cluster in region B is also mostly empty, although it accurately reflects the small amount of  $TBLG_{30^\circ}$  present. It should be noted that the  $TBLG_{30^\circ}$  in region B is formed by island growth, and the GMM classification identifies most of it as having more similarity to the islands from region A, than to the  $TBLG_{30^\circ}$  from region A (see the lower row of figure 8.9).

The example above is a good illustration of one of the pitfalls of this sort of automated data analysis: much care needs to be taken when labelling clusters from the training set. As the fitting is performed without human guidance, the model may not have converged on the features that one would expect. Any error in the labelling is likely to lead to a misidentification of features further down the line.

Overall, I have shown that, once trained and labelled, the GMM is able to successfully identify similar materials from a new region of the sample. The fact that we were able to identify all these regions from the parameters of a single peak also shows that the GMM can enhance the discriminating power of relatively small numbers of parameters.

## 8.6 Application to full spectra

The demonstrations above used peak parameters as inputs. This can be useful for analysis but requires fitting of peaks to the spectra, which can be time consuming and usually requires expert intervention to optimise the fits.

Figure 8.10: The 5 selected principal components.

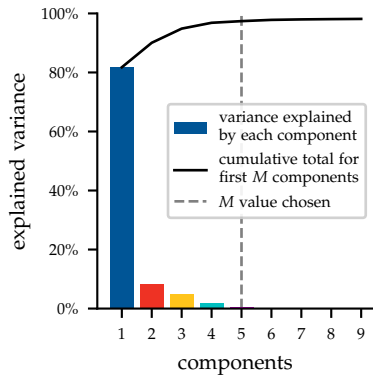
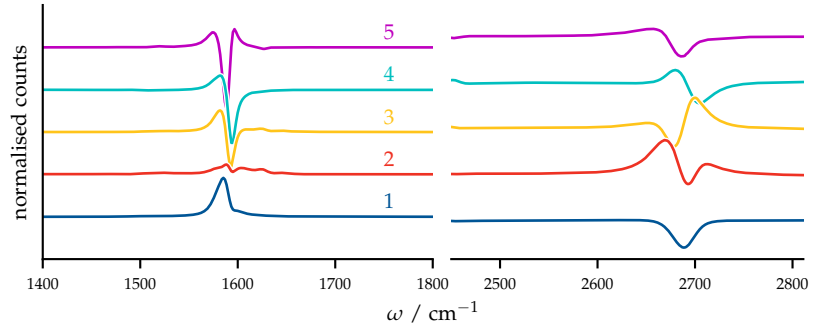


Figure 8.11: Bar chart showing the proportion of the total datacube variance explained by each component and solid line showing the cumulative total. A linear combination of just 5 components describes  $\sim 97.5\%$  of the total sample variance.

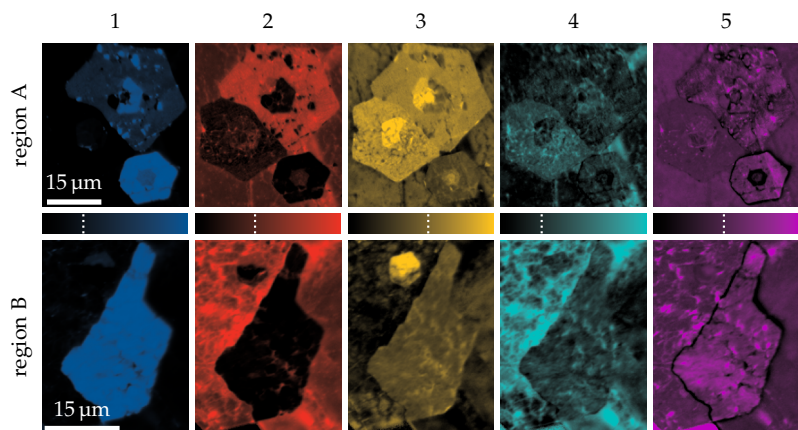
For fast material identification it would be more practical to put the whole Raman spectrum as input into the GMM without any supervised preprocessing. Although this is possible, the procedure is computationally expensive, as there are typically  $\sim 1000$  points in a typical spectrum, leading to a  $\sim 1000$ -dimensional space for the fitting. This is impractical as it takes a long time to converge and has a higher likelihood of converging on spurious local minima.

I circumvent this problem by reducing the dimensionality of our data using PCA, which works by using eigendecomposition of the covariance matrix of an entire dataset to identify the principal component vectors. For an  $M$ -dimensional space, there will be  $M$  vectors of length  $M$ . The data can then be expressed as a linear combination of these components. Each of these vectors accounts for a certain proportion of the total variance of the dataset. When there are strong correlations between parameters, as there are between neighbouring points in Raman spectra, we can account for a large fraction of the total variation using only a few components.

I ran PCA on the datacube from region A, normalised such that each spectrum forms a vector with unit magnitude. For Raman data, the principal component vectors resemble spectra. I show the normalised vectors for the first 5 principal components in figure 8.10.

Figure 8.11 shows the total variance explained by the 9 most dom-

Figure 8.12: Spatial distribution of principal components. Maps showing the coefficients of each of the 5 selected principal components (shown in figure 8.10), making up every spectrum in regions A and B. Coefficients can be positive or negative, and the white, dotted lines show the zero position.



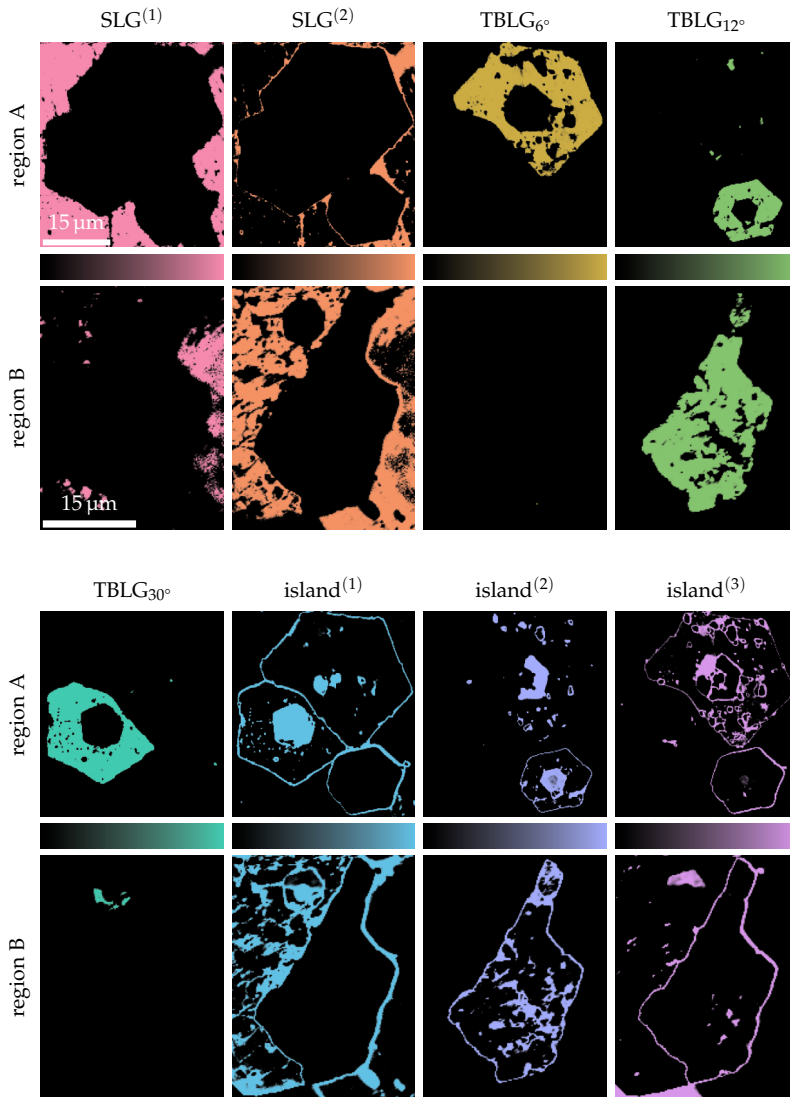


Figure 8.13: Full-spectrum, PCA-reduced clustering and identification. Images show spatial maps of the relative likelihood that a point is drawn from each Gaussian cluster identified in the 5-dimensional, PCA-reduced space. Labels assigned are based solely on analysis of region A.

inant components. It shows that we can reduce the dimensionality of our dataset from 1015 to just 5, by expressing our data using just those first 5 components and still explain  $\sim 97.5\%$  of the total variance.

A spectrum can then be expressed as a 5-dimensional vector of coefficients, corresponding to the amount of each component present. Spatial maps of these coefficients across both regions A and B are shown in figure 8.12.

I use these coefficients as input to a GMM trained on region A with  $N = 8$ , and then assign labels as I did in the preceding section. These are shown in figure 8.13. As the input vector is now 5-dimensional I cannot show a scatterplot showing the cluster distribution in data space as I did previously, but I show a pairwise scatterplot of each coefficient for region A and B in figure A.5. We see that the GMM has once again identified the same key regions we identified above, with the SLG area split into two clusters by varied

strain and charge doping, however we also see three distinct island growth clusters, which we attribute to different stacking configurations.

As before, I apply the pretrained model to classify region B, as shown in figure 8.12. We see that the SLG, TBLG<sub>12°</sub> and TBLG<sub>30°</sub> are correctly identified, and the absent TBLG<sub>6°</sub> does not appear in the map. There is some notable uncertainty in identification of the island growth regions, which also pick up a lot of the boundaries between regions. However this is shown in both training and test data, so could easily be accounted for with more verbose labelling. This indicates that these clusters are of the wide, low-weighting background-type discussed above. Additionally, these clusters are all composed of features that are not necessarily shared by both regions (there are no trilayer islands in region B), so it is unsurprising that the GMM does not find the same features in each region.

This shows that the PCA dimensionality reduction expresses the data well enough to be a viable alternative to curve fitting as a preprocessing step for GMM, which could potentially reduce the amount of expert time needed to perform this analysis.

## 8.7 Conclusions

In this chapter, I have demonstrated that, following initial training, GMM data clustering can be used successfully to quickly identify desired species of TBLG from Raman spectra. I showcased two approaches to reduce the dimensionality of the spectra before passing them to the algorithm: fitting peaks to the spectra, and pairing the GMM with PCA.

The advantage of using parameters returned from peak fitting as GMM inputs is that the returned clusters yield easy-to-interpret physical information on the per-cluster parameter distribution. This makes it a good complement to a more traditional Raman analysis approach.

I showed how the statistical information returned by the GMM after training, specifically the per-cluster means and covariance matrices, can be used to reveal important details about the sample. In our example I showed that the shifting of the G and 2D peaks in the SLG, attributed to inhomogeneous substrate interaction, could not result solely from strain, and must also have a contribution from changes in charge doping. This demonstrates a significant advantage of GMM above other clustering algorithms, which do not return the same statistical information.

By contrast, the physical meanings of the cluster distributions from GMM paired with PCA are harder to interpret. However the algorithms can take entire Raman spectra as input, which is a key benefit, as it means that acquired spectra could be assessed immediately, without the need for human intervention. It therefore enables automation of a process which often requires many hours of expert scrutiny, condensing the total analysis time down to seconds.

Like any machine learning tool, the performance of a GMM for classification will depend on the training data used and appropriate labelling of the identified clusters. For example, the areas I showed with the most indeterminacy in classification were the areas of our sample which differed most between our training and testing regions (for example the clusters in figure 8.9 associated with TBLG<sub>30°</sub> formed by artificial stacking in region A, and island growth in region B). In practice this can be mitigated by careful initial labelling, and appropriate selection of training data.

It is important to note that while twist angle is a continuous parameter, this analysis only demonstrates identification of the discrete bands of twist angles which were present in the training and testing datasets. For the purposes of material identification for applications, this doesn't present a problem, as typically only a single targeted twist angle is required. I also note that the recent theoretical work by Sheremetyeva et al. demonstrates the success of machine learning approaches for TBLG identification across the full range of possible twists [207]. This suggests that a training dataset covering a larger range of twists could enable discrimination of a greater number of angles.

As I have shown above, GMM is very well suited to classifying materials based on Raman spectra, but the techniques shown here can also be applied to any set of colocalised measurements, for example other forms of spectroscopy, or data acquired via scanning probe microscopy (SPM). Likewise, I have demonstrated the technique for successfully identifying TBLG, but it is equally suited to identifying species in any type of mixed-material sample, whose materials produce distinct measurements.

Automated analysis, using the machine learning techniques shown here, has potential to dramatically speed up material identification, particularly when paired with automated scanning. This will have profound consequences for the future of material optimisation and device fabrication, as it will remove a major bottleneck in the fabrication process. It can also make other samples with a stochastic distribution of materials, such as the TBLG shown in this work, more practicable for inclusion in devices, as automated scanning and analysis could identify and locate target materials from a whole substrate in a matter of hours, a process which previously may have taken days for a trained scientist.



## *Conclusions and outlook*

In this thesis, I have investigated a range of different van der Waals (vdW) materials and heterostructures with light-coupled scanning probe microscopy (SPM) and optical spectroscopy. There are two core findings which unite all of the original research chapters in part [III](#):

1. Nanoscale features of vdW materials and heterostructures, such as fractures folds and bubbles, play a significant role in determining their optoelectronic properties, particularly via their local effects on strain and doping.
2. Combining advanced microscopy and hyperspectral imaging with modern computational techniques, such as vector decomposition and machine learning, allows us to recover a wealth of important material properties from large datasets.

In chapter [5](#) I adapted a Raman vector decomposition scheme to spatial mapping. This showed how fractures, folds and bubbles in graphene-hexagonal boron nitride (hBN) heterostructures, which are typically introduced during fabrication, induce nanoscale strain and charge variations. I revealed that the scatter in the positions of Raman peaks reported in previous works [[108](#), [128](#)] is not random, but correlated to these features. Thanks to the strong influence of strain on the properties of two-dimensional (2d) materials [[13](#), [15](#)], we can expect that these would also play a significant role in determining their other optoelectronic properties.

Indeed, this is what I demonstrated in chapter [6](#), where I used scanning near-field optical microscopy (SNOM) to reveal nanoscale domains with strong absorption and high phase shifts for infrared (IR) light in bubbles in hBN-encapsulated graphene. As these domains were strongly correlated to one-dimensional features in the sides of bubbles, which alter the local band structure of graphene [[19](#)], I proposed that they were related to strain-induced changes in plasmonic properties. The ability to modify the nanoscale IR properties of graphene by strain suggests potential pathways to the creation of tailor made nanophotonic devices or metamaterials. However as bubbles are formed stochastically during fabrication of vdW heterostructures, this approach will only be viable if similar strain profiles are created artificially, or if fast automated methods to identify specific kinds of features from large areas are developed.

In chapter [7](#) I investigated the former of those conditions, by using

Raman and photoluminescence (PL) spectroscopy to probe strains in InSe that had been deposited on patterned substrates. I was able to demonstrate that for a sample of bulk InSe bent over an array of pillars, there was no detectable strain induced to the material. But for thin, 2d InSe, suspended over an array of holes, there were clear signatures of strain in the Raman spectra. This may be a partial reflection of the strain sensitivity of 2d materials compared to their bulk forms [13]. I also observed an enhancement of the PL signature at both pillars and holes, which I attributed to geometric effects caused by deformed materials, independent of strain [41].

Finally in chapter 8, I showcased several approaches to how data cluster analysis, a machine learning tool, can be used to quickly identify and analyse samples of twisted bilayer graphene (TBLG) from their Raman spectra. Like the bubbles discussed in chapters 5 and 6, these were formed stochastically, which would make locating specific kinds of TBLG time-consuming and laborious. The techniques I demonstrated in this chapter could allow fully automated Raman scanning, which could speed up prototyping of TBLG devices, and save precious hours of scientists' time.

As the field of 2d materials approaches adulthood, the focus of research must shift more and more towards scalable fabrication of 2d materials and devices. And as we navigate this transition, from bespoke, lab-based prototypes to mass production, the findings presented in this thesis will become more and more important.

I have shown that for optoelectronic 2d-material applications to be viable, we must have a thorough understanding of the strain and doping variations induced by nanoscale material features. As new fabrication techniques arise, and as new vdW materials are exploited, evaluating the effects of such features will become a vital quality control step.

Typically an increase in production yield is accompanied by a reduction in the scrutiny applied to each sample produced. However this need not be the case. Modern computational techniques, like the vector decomposition and data clustering showcased in this thesis, are readily adaptable to automated, high-throughput analysis, which means they should be able to keep up with a substantial expansion of 2d-material fabrication. On top of this, the success of such techniques for research purposes means they will likely soon become a part of the standard set of tools used to study new materials and devices.

In the long term, I hope that the methods and findings presented in this thesis will assist the development and refinement of scalable production methods for 2d-material devices, with precise control of the nanoscale material properties. This could enable features like bubbles and wrinkles to become functional and versatile elements to manipulate light-matter interaction at the nanoscale.

# Dissemination

## Publications

### **Surface-Mediated Aligned Growth of Monolayer MoS<sub>2</sub> and In-Plane Heterostructures with Graphene on Sapphire**

Kenshiro Suenaga, Hyungoo Ji, Yung-Chan Lin, **Tom Vincent**, Mina Maruyama, Adha Sukma Aji, Yoshihiro Shiratsuchi, Dong Ding, Kenji Kawahara, Susuma Okada, Vishal Panchal, Olga Kazakova, Hiroki Hibino, Kazu Suenaga and Hiroki Ago

[ACS Nano](#) **12** 10032 (2018)

### **Probing the nanoscale origin of strain and charge doping in graphene-hBN heterostructures**

**Tom Vincent**, Vishal Panchal, Tim Booth, Stephen R Power, Antti-Pekka Jauho, Vladimir Antonov and Olga Kazakova

[2D Materials](#) **6** 015022 (2019)

### **Contactless probing of graphene charge density variation in a controlled humidity environment**

Karl Brown, **Tom Vincent**, Eli G Castanon, Florina S Rus, Christos Melios, Olga Kazakova and Cristina E Giusca

[Carbon](#) **163** 408 (2020)

### **Strongly Absorbing Nanoscale Infrared Domains within Strained Bubbles at hBN-Graphene interfaces**

**Tom Vincent**, Matthew Hamer, Irina Grigorieva, Vladimir Antonov, Alexander Tzalenchuk and Olga Kazakova

[ACS Applied Materials and Interfaces](#) **12** 57638 (2020)

### **Anomalous low-thermal conductivity of atomically thin InSe probed by scanning thermal microscopy**

David Buckley, Zakhar R Kudrynskiy, Nilanthy Balakrishnan, **Tom Vincent**, Eli Castanon, Zakhar D Kovalyuk, Olga Kazakova, Alexander Tzalenchuk and Amalia Patanè

[Advanced Functional Materials](#) **31** 2008967 (2021)

<sup>4</sup> Invited front-matter article

### **Scanning near-field infrared microscopy<sup>4</sup>**

**Tom Vincent**

[Nature Reviews Physics 3 537 \(2021\)](#)

### **Opportunities in Electrically Tunable 2D Materials Beyond Graphene: Recent Progress and Future Outlook**

<sup>5</sup> Joint first authorship with Jiayun Liang and Simrjit Singh

**Tom Vincent,<sup>5</sup> Jiayun Liang, Simrjit Singh, Eli G Castanon, Xiaotian Zhang, Amber McCreary, Deep Jariwala, Olga Kazakova and Zakaria Al Balushi**

[Applied Physics Reviews 8 4 \(2021\)](#)

### **Probing nanoscale Schottky barrier characteristics at WSe<sub>2</sub>/graphene heterostructures via electrostatic doping**

Filipe Richheimer, **Tom Vincent**, Alessandro Catanzaro, Nathaniel Huang, Mark A Baker, Robert A Dorey, Cristina Giusca, Fernando A Castro, Olga Kazakova and Sebastian Wood

Accepted for publication at Advanced Electronic Materials

### **Curvature-enhanced localised emission from dark states in wrinkled monolayer WSe<sub>2</sub> at room temperature**

Sebastian Wood, Filipe Richheimer, **Tom Vincent**, Vivian Tong, Alessandro Catanzaro, Yameng Cao, Olga Kazakova, and Fernando A Castro

Submitted to Advanced Materials

### **Data Cluster Analysis and Machine Learning for Classification of Twisted Bilayer Graphene**

**Tom Vincent**, Kenji Kawahara, Vladimir Antonov, Hiroki Ago and Olga Kazakova

Submitted to Carbon and available on [arXiv](#)

## *Presentations*

### *Oral*

#### **Nanoscale optical properties of bubbles in graphene heterostructures**

European Forum on Nanoscale IR Spectroscopy,  
Amsterdam, Netherlands (2019)

#### **Optical metrology of 2d materials on the nanoscale**

NPL frontiers of measurement seminar for UCL CDT students,  
Teddington, UK (2020)

#### **Data clustering for fast analysis of Raman data**

NPL QMS internal conference, online (2020)  
NPL PGI conference, online (2020)

### **Revealing the nanoscale infrared properties of strained graphene bubbles**

NanoIR Spectroscopy and Imaging: Recent Developments and Applications,<sup>6</sup> online (2021)  
 Microscience Microscopy Congress,<sup>7</sup> online (2021)

<sup>6</sup> Invited presentation

<sup>7</sup> Flash presentation

#### *Posters*

### **Raman mapping of strain and doping in graphene-hBN heterostructures**

**Tom Vincent**, Eli Castañón, Vishal Panchal, Tim Booth and Olga Kazakova  
 Graphene Study Winter, Obergurgl, Austria (2018)

### **Combined sSNOM and Raman study on folded graphene in graphene-MoS<sub>2</sub> lateral heterostructures**

**Tom Vincent**, Christos Melios, Vishal Panchal, Hiroki Ago, Vladimir Antonov and Olga Kazakova

Graphene Study Summer, Hindås, Sweden  
 European Forum on Nanoscale IR Spectroscopy, Teddington, UK  
 NPL Graphene and 2-D Materials Conference, Teddington, UK  
 NPL Science & Technologies Advisory Council, Teddington, UK  
 (all 2018)

### **Nanoscale properties of bubbles in graphene heterostructures**

**Tom Vincent**, Matthew Hamer, Irina Grigorieva, Alexander Tzalenchuk and Olga Kazakova

Graphene Week, Helsinki, Finland (2019)  
 EPSRC visit to Royal Holloway, Egham, UK (2019)  
 THz imaging of 2d materials workshop, Teddington, UK (2020)  
 Microscience Microscopy Congress, online (2021)

### **Probing optical properties of Bi<sub>2</sub>Se<sub>3</sub> nanowires with infrared and terahertz SNOM**

**Tom Vincent**, Jessica Boland and Olga Kazakova

THz imaging of 2d materials workshop, Teddington, UK (2020)

### **Machine-learning-assisted identification and analysis of twisted bilayer graphene**

**Tom Vincent**, Kenji Kawahara, Vladimir Antonov, Hiroki Ago and Olga Kazakova

Graphene Week, online (2021)  
 EPSRC visit to Royal Holloway, Egham, UK (2022)



## *List of abbreviations*

*1d* one-dimensional.

*2d* two-dimensional.

*3d* three-dimensional.

*AC* alternating current.

*AFM* atomic force microscopy.

*AFM-IR* atomic force microscope infrared spectroscopy.

*BLG* bilayer graphene.

*BZ* Brillouin zone.

*CCD* charge-coupled device.

*CNP* charge neutrality point.

*CVD* chemical vapour deposition.

*DC* direct current.

*DOS* density of states.

*EM* electromagnetic.

*EPS* electron-phonon scattering.

*FDM* finite dipole model.

*FET* field effect transistor.

*FTIR* Fourier transform infrared.

*FWHM* full width at half maximum.

*GMM* Gaussian mixture model.

*hBN* hexagonal boron nitride.

*HP $h$ P* hyperbolic phonon polariton.

*IR* infrared.

*MCT* mercury cadmium telluride detector.

*OPD* optical path distance.

*PCA* principle component analysis.

*PDF* probability density function.

*PDM* point dipole model.

*PID* proportional, integral, derivative controller.

*PL* photoluminescence.

*PLL* phase-locked loop.

*PMF* pseudomagnetic field.

*PMMA* (poly)methyl methacrylate.

*PP* plasmon polariton.

*PTMC* post-transition metal chalcogenide.

*PVA* (poly)vinyl acetate.

*QCL* quantum cascade laser.

*RPA* random phase approximation.

*SLG* single layer graphene.

*SNOM* scanning near-field optical microscopy.

*SNR* signal-to-noise ratio.

*SPM* scanning probe microscopy.

*SPP* surface plasmon polariton.

*STM* scanning tunnelling microscopy.

*TBLG* twisted bilayer graphene.

*TMD* transition metal dichalcogenide.

*vdW* van der Waals.

## *List of symbols*

$A$  peak area.

$A_{PV}$  pseudovector potential.

$a$  nearest neighbour lattice separation.

$\mathbf{a}_1$  1<sup>st</sup> real space lattice vector.

$\mathbf{a}_2$  2<sup>nd</sup> real space lattice vector.

$B_{PMF}$  pseudomagnetic field.

$\mathbf{b}_1$  1<sup>st</sup> reciprocal lattice vector.

$\mathbf{b}_2$  2<sup>nd</sup> reciprocal lattice vector.

$C_g$  geometrical capacitance.

$c_0$  vacuum speed of light.

$\mathbf{E}$  electric field.

$E$  energy.

$E_b$  exciton binding energy.

$E_F$  Fermi level.

$E_g$  bandgap energy.

$E_{ph}$  photon energy.

$E_\omega$  phonon energy.

$e$  Euler's number.

$e_q$  electron charge.

$g_s$  strain-scalar potential coupling energy.

$h$  Planck constant.

$\hbar$  reduced Planck constant ( $h/2\pi$ ).

$I$  peak intensity.

$i$  the imaginary unit.

$J$  current density.

$k$  wavevector.

$k$  wavenumber.

$k_B$  Boltzmann constant.

$k_{PP}$  complex PP wavevector.

$k_{\parallel}$  in-plane component of wavevector.

$k_{\perp}$  normal component of wavevector.

$n$  carrier density.

$n_e$  electron density.

$n_h$  hole density.

$q$  wavevector relative to the  $\mathbf{K}$  point.

$r_p$  AFM probe radius of curvature.

$s_n$   $n^{\text{th}}$  harmonic demodulated near-field amplitude.

$T$  temperature.

$t$  time.

$V$  voltage.

$V_{def}$  AFM deflection voltage.

$V_{ds}$  transistor drain-source voltage.

$V_g$  gate voltage.

$v_F$  Fermi velocity.

$X$  lock-in amplifier in-phase demodulated signal.

$Y$  lock-in amplifier out-of-phase demodulated signal.

$\alpha$  polarisability.

$\alpha_{fs}$  fine structure constant.

$\beta$  shear deformation potential.

$\beta_{ML}$  multilayer reflection coefficient.

- $\beta_{PP}$  PP confinement factor.
- $\beta_r$  electrostatic reflection coefficient.
- $\beta_\varepsilon$  hopping potential decay constant.
- $\Gamma$  full width at half maximum.
- $\gamma$  Grüneisen parameter.
- $\gamma_0$  nearest-neighbour hopping energy.
- $\gamma'_0$  second-nearest-neighbour hopping energy.
- $\gamma_1$  interlayer vertical hopping energy.
- $\gamma_D^{-1}$  inverse damping coefficient.
- $\varepsilon$  dielectric function.
- $\varepsilon_0$  vacuum permittivity.
- $\varepsilon$  strain.
- $\varepsilon_{bi}$  biaxial strain.
- $\varepsilon_{hs}$  hydrostatic strain.
- $\varepsilon_s$  shear strain.
- $\theta_t$  relative twist angle between lattices.
- $\lambda$  wavelength.
- $\lambda_m$  moiré period.
- $\lambda_{PP}$  wavelength.
- $\rho$  density of states per unit cell.
- $\sigma$  conductivity.
- $\sigma_0$  graphene universal conductivity.
- $\sigma_s$  standard deviation.
- $\tau$  carrier relaxation time.
- $\phi_n$   $n^{\text{th}}$  harmonic demodulated near-field phase.
- $\phi_{ref}$  lock-in amplifier reference phase.
- $\Phi_s$  scalar potential.
- $\omega$  angular frequency; phonon wavenumber (see [explanation](#) in chapter 4).
- $\omega_0$  AFM tapping frequency.
- $\omega_{ref}$  lock-in amplifier reference frequency.



## List of figures

1.1	Graphene lattice structure	15
1.2	Graphene Brillouin zone	16
1.3	Band structure of graphene	17
1.4	Simple graphene field effect transistor example.	18
1.5	Example transfer curve from a graphene field effect transistor.	18
1.6	Pseudomagnetic fields and scalar potentials in strained graphene.	19
1.7	Interband optical transitions in charge-neutral and doped graphene.	20
1.8	Graphene optical conductivity.	21
1.9	Doping dependence of graphene's optical conductivity.	21
1.10	Diagram of PPs in graphene	22
1.11	Dispersion of surface plasmon polaritons in graphene	23
1.12	Example image of PPs in graphene.	24
1.13	Bernal-stacked bilayer graphene	25
1.14	Bilayer graphene band structure.	26
1.15	Moiré patterns in twisted bilayer graphene.	27
1.16	Qualitative description of TBLG twist dependence.	27
2.1	Hexagonal boron nitride lattice structure	30
2.2	Example image of HPhPs in hBN.	30
2.3	Transition metal dichalcogenide lattice structure	31
2.4	Post-transition metal chalcogenide lattice structure	32
2.5	Contacting encapsulated graphene.	35
2.6	Self cleaning in van der Waals heterostructures.	36
2.7	Transfer of 2d materials.	37
3.1	Diagram of an AFM setup.	42
3.2	Lock-in amplifier operation principle.	43
3.3	Near-field-sample interaction.	44
3.4	Origin of the high harmonics in the near field.	46
3.5	Michelson interferometer for phase-sensitive SNOM.	47
3.6	Principle of AFM-IR.	48
4.1	Light-matter interaction processes for optical spectroscopy.	52
4.2	Optical spectroscopy apparatus schematic.	53
4.3	Graphene phonon dispersions.	54
4.4	The Raman peaks of graphene.	55
4.5	Strain-dependent G and 2D peak shifts.	57
4.6	Doping-dependent G and 2D peak shifts.	58

5.1	Strain and doping induced peak shifting.	63
5.2	Strain-doping decomposition.	64
5.3	Heterostructure A optical image.	65
5.4	Heterostructure A AFM images.	66
5.5	Line profiles taken across a fracture and a fold.	66
5.6	Heterostructure A Raman intensities.	66
5.7	Key Raman indicators for bare and hBN-covered graphene.	67
5.8	G-2D position scatter plot for bare and hBN-covered graphene.	67
5.9	Strain and doping in bare and hBN-covered graphene.	68
5.10	Heterostructure B optical image.	69
5.11	Heterostructure B AFM image.	69
5.12	Heterostructure B Raman intensities.	70
5.13	Key Raman indicators for encapsulated graphene.	70
5.14	G-2D position scatter plot for encapsulated graphene.	70
5.15	Spatial maps of strain and doping in encapsulated graphene.	71
5.16	Line profiles taken across a bubble.	72
6.1	Side-on schematic of the heterostructure studied in this chapter.	77
6.2	Optical image showing bubbles in encapsulated graphene.	77
6.3	Topography of bubbles in encapsulated graphene.	78
6.4	SNOM maps of a network of bubbles in encapsulated graphene.	79
6.5	Wavelength dependence of the domains near $1000\text{ cm}^{-1}$ .	80
6.6	Single bubble imaged with a range of frequencies.	82
6.7	AFM-IR of a bubble in encapsulated graphene.	83
6.8	Raman spectra from a flat area and a bubble.	84
6.9	Strain-doping decomposition.	84
6.10	Raman acquired maps from sample.	85
6.11	Strain profiles of a uni- and biaxially strained bubble.	85
6.12	Graphene Fermi level and onset of Pauli blocking.	87
7.1	The Raman spectrum of indium selenide.	92
7.2	Optical image of indium selenide on pillars.	93
7.3	Cross-section of indium selenide on a pillar.	93
7.4	Raman mapping of indium selenide on pillars.	94
7.5	PL mapping of indium selenide on pillars.	95
7.6	Optical image of indium selenide on holes.	96
7.7	Cross-section of indium selenide on a pillar.	96
7.8	Raman mapping of indium selenide on holes.	97
7.9	PL mapping of InSe on holes.	98
7.10	Time-resolved PL of indium selenide.	99
7.11	Time-resolved Raman of indium selenide.	100
8.1	Fabrication process.	105
8.2	Optical microscope image.	106
8.3	Raman features of twisted bilayer graphene: region A.	107
8.4	Raman features of twisted bilayer graphene: region B.	108
8.5	Mahalanobis normalisation.	109
8.6	Unnormalised G and 2D peak shifts from region A.	109
8.7	Gaussian mixture model example.	110
8.8	Classifying new data using pretrained clusters.	111

8.9	2D peak clustering and identification.	112
8.10	The 5 selected principal components.	114
8.11	Bar chart of principal components.	114
8.12	Spatial distribution of principal components.	114
8.13	Full-spectrum, PCA-reduced clustering and identification.	115
A.1	Visible light unit conversions.	135
A.2	Mid-IR light unit conversions.	136
A.3	Raman shift to PL energy conversions.	136
A.4	<i>k</i> -means example.	137
A.5	Pairwise comparison of principle components.	137



# Appendices

## Optical unit conversion charts

There are many units to describe light and different units are helpful in different situations. The charts in this section can be used to quickly convert between units for light in the visible and mid-infrared (IR) regions. I've also added a chart which can be used to convert between Raman shift and photoluminescence (PL) energy for optical spectroscopy measurements with a known excitation laser wavelength.

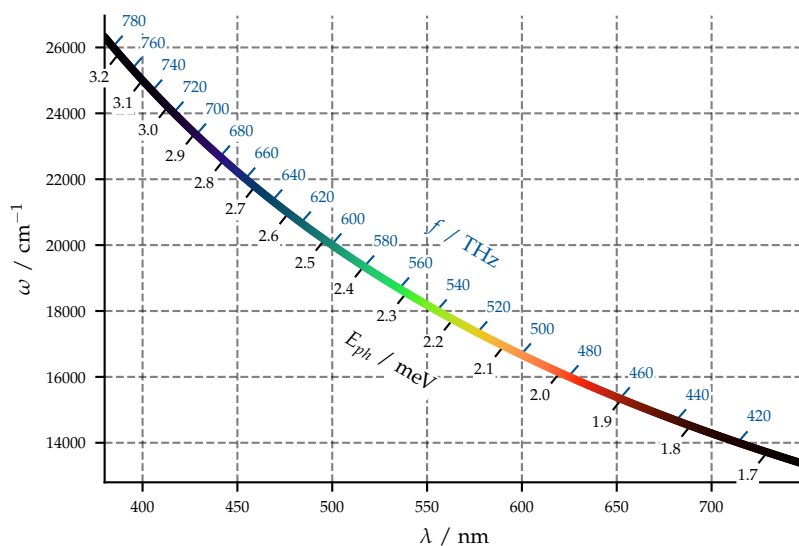


Figure A.1: Visible light unit conversions.

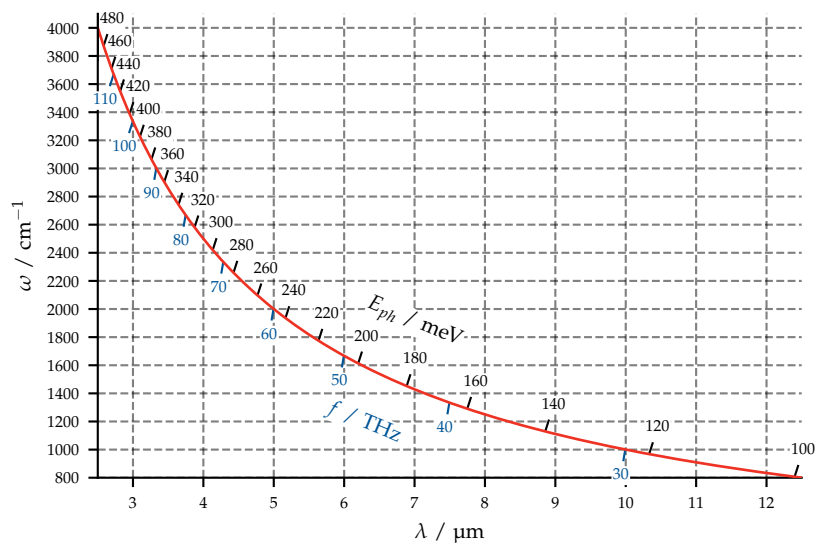


Figure A.2: Mid-IR light unit conversions..

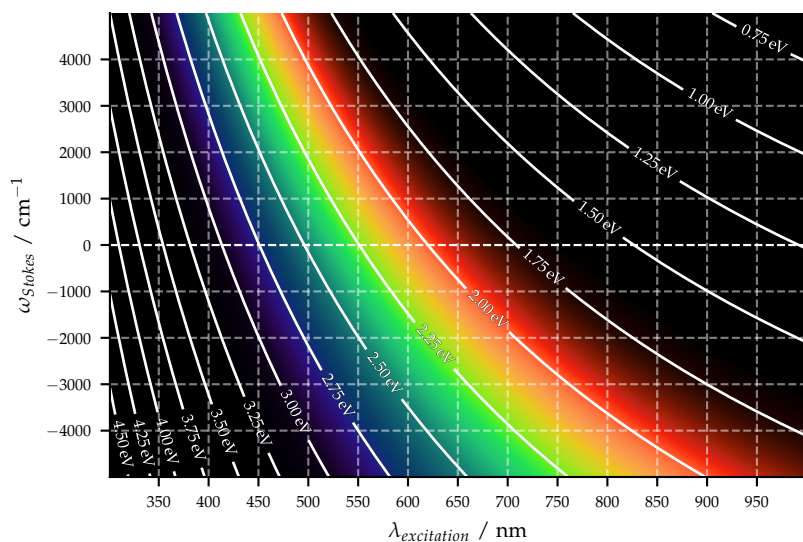


Figure A.3: Raman shift to PL energy conversions.

### Supplementary data clustering figures

This section contains extra figures which relate to the work presented in chapter 8, [Data cluster analysis of twisted bilayer graphene](#).

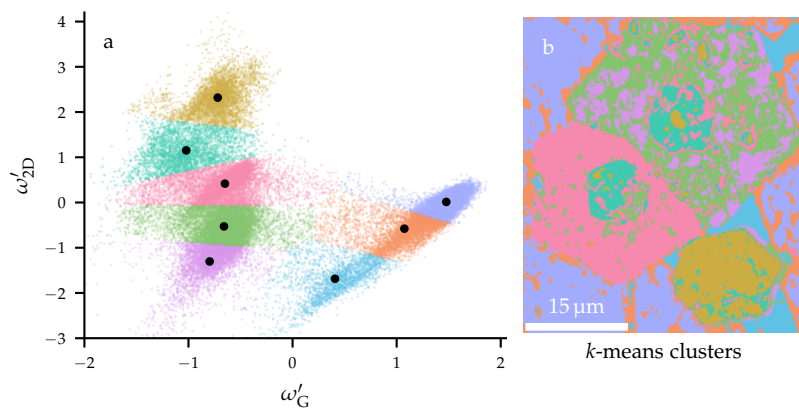


Figure A.4: *k*-means example. **(a)** Scatterplot of Mahalanobis normalised positions of the G and 2D peaks from region A. Points are coloured according to the cluster assigned to them by an 8-component *k*-means analysis of the data shown. **(b)** Key to cluster colour and spatial distribution.

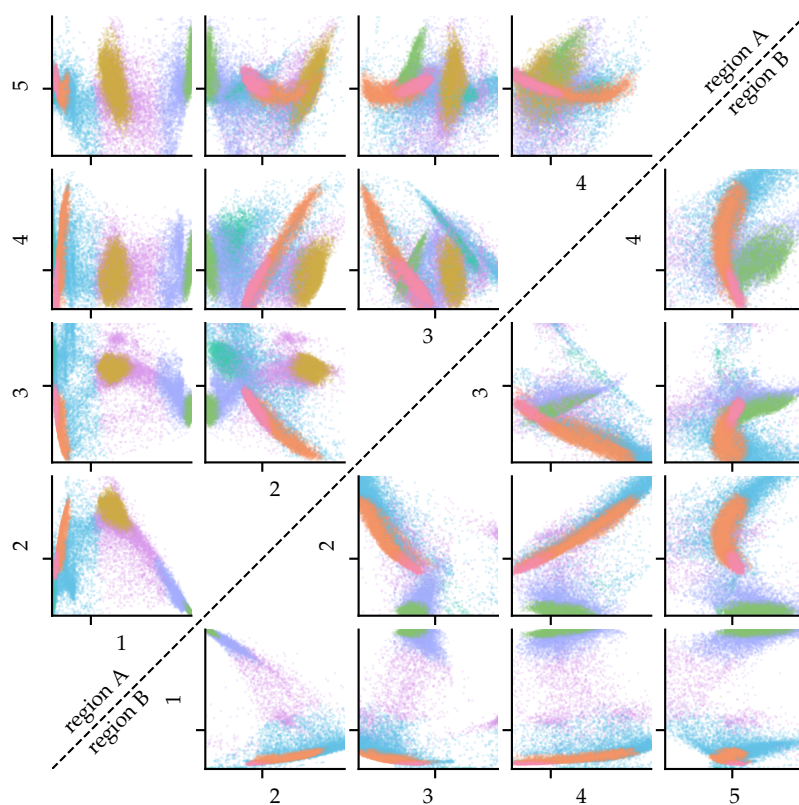


Figure A.5: Pairwise comparison of principle components. Scatterplots showing the relative distribution between each combination of the 5 selected principal components (shown in figure 8.10). Points are coloured by the cluster assigned by the full spectrum Gaussian mixture model (GMM), as shown in (figure 8.12). Data is in arbitrary units and axis ticks indicate the zero position. Plots above and below the central diagonal show the distributions in regions A and B.



# Bibliography

1. Novoselov, K. S., Geim, A. K., Morozov, S. V., Jiang, D., Zhang, Y., Dubonos, S. V., Grigorieva, I. V. & Firsov, A. A. [Electric Field Effect in Atomically Thin Carbon Films](#). *Science* **306**, 5696 (2004).
2. Vincent, T., Liang, J., Singh, S., Castanon, E. G., Zhang, X., McCreary, A., Jariwala, D., Kazakova, O. & Al Balushi, Z. Y. [Opportunities in electrically tunable 2D materials beyond graphene: Recent progress and future outlook](#). *Applied Physics Reviews* **8**, 4 (2021).
3. Geim, A. K. & Grigorieva, I. V. [Van der Waals heterostructures](#). *Nature* **499**, 7459 (2013).
4. Dean, C. R., Young, A. F., Meric, I., Lee, C., Wang, L., Sorgenfrei, S., Watanabe, K., Taniguchi, T., Kim, P., Shepard, K. L. & Hone, J. [Boron nitride substrates for high-quality graphene electronics](#). *Nature Nanotechnology* **5**, 10 (2010).
5. Haigh, S. J., Gholinia, A., Jalil, R., Romani, S., Britnell, L., Elias, D. C., Novoselov, K. S., Ponomarenko, L. A., Geim, A. K. & Gorbachev, R. [Cross-sectional imaging of individual layers and buried interfaces of graphene-based heterostructures and superlattices](#). *Nature Materials* **11**, 9 (2012).
6. Novoselov, K. S., Mishchenko, A., Carvalho, A. & Castro Neto, A. H. [2D materials and van der Waals heterostructures](#). *Science* **353**, 6298 (2016).
7. Seo, G., Lee, G., Kim, M. J., Baek, S.-h., Choi, M., Ku, K. B., Lee, C.-S., Jun, S., Park, D., Kim, H. G., Kim, S.-J., Lee, J.-o., Kim, B. T., Park, E. C. & Kim, S. I. [Rapid Detection of COVID-19 Causative Virus \(SARS-CoV-2\) in Human Nasopharyngeal Swab Specimens Using Field-Effect Transistor-Based Biosensor](#). *ACS Nano* **14**, 4 (2020).
8. Woessner, A., Gao, Y., Torre, I., Lundberg, M. B., Tan, C., Watanabe, K., Taniguchi, T., Hillenbrand, R., Hone, J., Polini, M. & Koppens, F. H. L. [Electrical  \$2\pi\$  phase control of infrared light in a 350-nm footprint using graphene plasmons](#). *Nature Photonics* **11**, 7 (2017).
9. Cao, Y., Fatemi, V., Fang, S., Watanabe, K., Taniguchi, T., Kaxiras, E. & Jarillo-Herrero, P. [Unconventional superconductivity in magic-angle graphene superlattices](#). *Nature* **556**, 7699 (2018).

10. Castro Neto, A. H., Guinea, F., Peres, N. M. R., Novoselov, K. S. & Geim, A. K. [The electronic properties of graphene](#). *Reviews of Modern Physics* **81**, 1 (2009).
11. Kretinin, A. V., Cao, Y., Tu, J. S., Yu, G. L., Jalil, R., Novoselov, K. S., Haigh, S. J., Gholinia, A., Mishchenko, A., Lozada, M., Georgiou, T., Woods, C. R., Withers, F., Blake, P., Eda, G., Wirsig, A., Hucho, C., Watanabe, K., Taniguchi, T., Geim, A. K. & Gorbachev, R. V. [Electronic properties of graphene encapsulated with different two-dimensional atomic crystals](#). *Nano Letters* **14**, 6 (2014).
12. Das, A., Chakraborty, B., Piscanec, S., Pisana, S., Sood, A. K. & Ferrari, A. C. [Phonon renormalization in doped bilayer graphene](#). *Physical Review B* **79**, 15 (2009).
13. Bissett, M. A., Tsuji, M. & Ago, H. [Strain engineering the properties of graphene and other two-dimensional crystals](#). *Physical Chemistry Chemical Physics* **16**, 23 (2014).
14. Zhai, D. & Sandler, N. [Electron dynamics in strained graphene](#). *Modern Physics Letters B* **33**, 28 (2019).
15. Settnes, M., Power, S. R., Lin, J., Petersen, D. H. & Jauho, A.-P. [Bubbles in graphene - a computational study](#). *Journal of Physics: Conference Series* **647**, 1 (2015).
16. Stegmann, T. & Szpak, N. [Current splitting and valley polarization in elastically deformed graphene](#). *2D Materials* **6**, 1 (2018).
17. Georgi, A., Nemes-Incze, P., Carrillo-Bastos, R., Faria, D., Viola Kusminskiy, S., Zhai, D., Schneider, M., Subramaniam, D., Mashoff, T., Freitag, N. M., Liebmann, M., Pratzner, M., Wirtz, L., Woods, C. R., Gorbachev, R. V., Cao, Y., Novoselov, K. S., Sandler, N. & Morgenstern, M. [Tuning the Pseudospin Polarization of Graphene by a Pseudomagnetic Field](#). *Nano Letters* **17**, 4 (2017).
18. Faria, D., León, C., Lima, L. R., Latgé, A. & Sandler, N. [Valley polarization braiding in strained graphene](#). *Physical Review B* **101**, 8 (2020).
19. Wu, Y., Zhai, D., Pan, C., Cheng, B., Taniguchi, T., Watanabe, K., Sandler, N. & Bockrath, M. [Quantum Wires and Waveguides Formed in Graphene by Strain](#). *Nano Letters* **18**, 1 (2018).
20. Levy, N., Burke, S. A., Meaker, K. L., Panlasigui, M., Zettl, A., Guinea, F., Neto, A. H. C. & Crommie, M. F. [Strain-Induced Pseudo-Magnetic Fields Greater Than 300 Tesla in Graphene Nanobubbles](#). *Science* **329**, 5991 (2010).
21. Nair, R. R., Blake, P., Grigorenko, A. N., Novoselov, K. S., Booth, T. J., Stauber, T., Peres, N. M. R. & Geim, A. K. [Fine Structure Constant Defines Visual Transparency of Graphene](#). *Science* **320**, 5881 (2008).

22. Koppens, F. H. L., Chang, D. E. & García de Abajo, F. J. [Graphene Plasmonics: A Platform for Strong Light–Matter Interactions](#). *Nano Letters* **11**, 8 (2011).
23. Woessner, A., Lundeberg, M. B., Gao, Y., Principi, A., Alonso-González, P., Carrega, M., Watanabe, K., Taniguchi, T., Vignale, G., Polini, M., Hone, J., Hillenbrand, R. & Koppens, F. H. L. [Highly confined low-loss plasmons in graphene–boron nitride heterostructures](#). *Nature Materials* **14**, 4 (2015).
24. Falkovsky, L. A. [Optical properties of graphene](#). *Journal of Physics: Conference Series* **129** (2008).
25. Jablan, M., Buljan, H. & Soljačić, M. [Plasmonics in graphene at infrared frequencies](#). *Physical Review B* **80**, 24 (2009).
26. Ni, G. X., McLeod, A. S., Sun, Z., Wang, L., Xiong, L., Post, K. W., Sunku, S. S., Jiang, B.-Y., Hone, J., Dean, C. R., Fogler, M. M. & Basov, D. N. [Fundamental limits to graphene plasmonics](#). *Nature* **557**, 7706 (2018).
27. Low, T., Chaves, A., Caldwell, J. D., Kumar, A., Fang, N. X., Avouris, P., Heinz, T. F., Guinea, F., Martin-Moreno, L. & Koppens, F. [Polaritons in layered two-dimensional materials](#). *Nature Materials* **16**, 2 (2017).
28. Cao, Y., Fatemi, V., Demir, A., Fang, S., Tomarken, S. L., Luo, J. Y., Sanchez-Yamagishi, J. D., Watanabe, K., Taniguchi, T., Kaxiras, E., Ashoori, R. C. & Jarillo-Herrero, P. [Correlated insulator behaviour at half-filling in magic-angle graphene superlattices](#). *Nature* **556**, 7699 (2018).
29. Chen, G., Sharpe, A. L., Fox, E. J., Zhang, Y.-H., Wang, S., Jiang, L., Lyu, B., Li, H., Watanabe, K., Taniguchi, T., Shi, Z., Senthil, T., Goldhaber-Gordon, D., Zhang, Y. & Wang, F. [Tunable correlated Chern insulator and ferromagnetism in a moiré superlattice](#). *Nature* **579**, 7797 (2020).
30. Yankowitz, M., Xue, J. & LeRoy, B. J. [Graphene on hexagonal boron nitride](#). *Journal of Physics: Condensed Matter* **26**, 30 (2014).
31. Caldwell, J. D., Aharonovich, I., Cassabois, G., Edgar, J. H., Gil, B. & Basov, D. N. [Photonics with hexagonal boron nitride](#). *Nature Reviews Materials* **4**, 8 (2019).
32. Dai, S., Ma, Q., Andersen, T., Mcleod, A. S., Fei, Z., Liu, M. K., Wagner, M., Watanabe, K., Taniguchi, T., Thiemens, M., Keilmann, F., Jarillo-Herrero, P., Fogler, M. M. & Basov, D. N. [Sub-diffractive focusing and guiding of polaritonic rays in a natural hyperbolic material](#). *Nature Communications* **6**, 1 (2015).
33. Bak, A. O., Yoxall, E. O., Sarriugarte, P., Giannini, V., Maier, S. A., Hillenbrand, R., Pendry, J. B. & Phillips, C. C. [Harnessing a Quantum Design Approach for Making Low-Loss Superlenses](#). *Nano Letters* **16**, 3 (2016).

34. Yoxall, E., Schnell, M., Nikitin, A. Y., Txoperena, O., Woessner, A., Lundeborg, M. B., Casanova, F., Hueso, L. E., Koppens, F. H. & Hillenbrand, R. [Direct observation of ultraslow hyperbolic polariton propagation with negative phase velocity](#). *Nature Photonics* **9**, 10 (2015).
35. Dai, S., Ma, Q., Yang, Y., Rosenfeld, J., Goldflam, M. D., McLeod, A., Sun, Z., Andersen, T. I., Fei, Z., Liu, M., Shao, Y., Watanabe, K., Taniguchi, T., Thiemens, M., Keilmann, F., Jarillo-Herrero, P., Fogler, M. M. & Basov, D. N. [Efficiency of Launching Highly Confined Polaritons by Infrared Light Incident on a Hyperbolic Material](#). *Nano Letters* **17**, 9 (2017).
36. Mak, K. F., Lee, C., Hone, J., Shan, J. & Heinz, T. F. [Atomically Thin MoS<sub>2</sub>: A New Direct-Gap Semiconductor](#). *Physical Review Letters* **105**, 13 (2010).
37. Splendiani, A., Sun, L., Zhang, Y., Li, T., Kim, J., Chim, C. Y., Galli, G. & Wang, F. [Emerging photoluminescence in monolayer MoS<sub>2</sub>](#). *Nano Letters* **10**, 4 (2010).
38. Balakrishnan, N., Steer, E. D., Smith, E. F., Kudrynskyi, Z. R., Kovalyuk, Z. D., Eaves, L., Patanè, A. & Beton, P. H. [Epitaxial growth of  \$\gamma\$ -InSe and  \$\alpha\$ ,  \$\beta\$ , and  \$\gamma\$ -In<sub>2</sub>Se<sub>3</sub> on  \$\epsilon\$ -GaSe](#). *2D Materials* **5**, 3 (2018).
39. Mudd, G. W., Molas, M. R., Chen, X., Zólyomi, V., Nogajewski, K., Kudrynskyi, Z. R., Kovalyuk, Z. D., Yusa, G., Makarovskiy, O., Eaves, L., Potemski, M., Fal'ko, V. I. & Patanè, A. [The direct-to-indirect band gap crossover in two-dimensional van der Waals Indium Selenide crystals](#). *Scientific Reports* **6**, 1 (2016).
40. Mudd, G. W., Svatek, S. A., Ren, T., Patanè, A., Makarovskiy, O., Eaves, L., Beton, P. H., Kovalyuk, Z. D., Lashkarev, G. V., Kudrynskyi, Z. R. & Dmitriev, A. I. [Tuning the Bandgap of Exfoliated InSe Nanosheets by Quantum Confinement](#). *Advanced Materials* **25**, 40 (2013).
41. Bandurin, D. A., Tyurnina, A. V., Yu, G. L., Mishchenko, A., Zólyomi, V., Morozov, S. V., Kumar, R. K., Gorbachev, R. V., Kudrynskyi, Z. R., Pezzini, S., Kovalyuk, Z. D., Zeitler, U., Novoselov, K. S., Patanè, A., Eaves, L., Grigorieva, I. V., Fal'ko, V. I., Geim, A. K. & Cao, Y. [High electron mobility, quantum Hall effect and anomalous optical response in atomically thin InSe](#). *Nature Nanotechnology* **12**, 3 (2017).
42. Buckley, D., Kudrynskyi, Z. R., Balakrishnan, N., Vincent, T., Mazumder, D., Castanon, E., Kovalyuk, Z. D., Kolosov, O., Kazakova, O., Tzalenchuk, A. & Patanè, A. [Anomalous Low Thermal Conductivity of Atomically Thin InSe Probed by Scanning Thermal Microscopy](#). *Advanced Functional Materials* **2008967** (2021).
43. Burch, K. S., Mandrus, D. & Park, J.-g. [Magnetism in two-dimensional van der Waals materials](#). *Nature* **563**, 7729 (2018).

44. Gong, C. & Zhang, X. [Two-dimensional magnetic crystals and emergent heterostructure devices](#). *Science* **363**, 6428 (2019).
45. Chang, K., Liu, J., Lin, H., Wang, N., Zhao, K., Zhang, A., Jin, F., Zhong, Y., Hu, X., Duan, W., Zhang, Q., Fu, L., Xue, Q.-K., Chen, X. & Ji, S.-H. [Discovery of robust in-plane ferroelectricity in atomic-thick SnTe](#). *Science* **353**, 6296 (2016).
46. Yankowitz, M., Chen, S., Polshyn, H., Zhang, Y., Watanabe, K., Taniguchi, T., Graf, D., Young, A. F. & Dean, C. R. [Tuning superconductivity in twisted bilayer graphene](#). *Science* **363**, 6431 (2019).
47. Backes, C. *et al.* [Production and processing of graphene and related materials](#). *2D Materials* **7**, 2 (2020).
48. Cai, Z., Liu, B., Zou, X. & Cheng, H.-m. [Chemical Vapor Deposition Growth and Applications of Two-Dimensional Materials and Their Heterostructures](#). *Chemical Reviews* **118**, 13 (2018).
49. Ogawa, Y., Hu, B., Orofeo, C. M., Tsuji, M., Ikeda, K.-i., Mizuno, S., Hibino, H. & Ago, H. [Domain Structure and Boundary in Single-Layer Graphene Grown on Cu\(111\) and Cu\(100\) Films](#). *The Journal of Physical Chemistry Letters* **3**, 2 (2012).
50. Hu, B., Ago, H., Ito, Y., Kawahara, K., Tsuji, M., Magome, E., Sumitani, K., Mizuta, N., Ikeda, K.-i. & Mizuno, S. [Epitaxial growth of large-area single-layer graphene over Cu\(111\)/sapphire by atmospheric pressure CVD](#). *Carbon* **50**, 1 (2012).
51. Ago, H., Kawahara, K., Ogawa, Y., Tanoue, S., Bissett, M. A., Tsuji, M., Sakaguchi, H., Koch, R. J., Fromm, F., Seyller, T., Komatsu, K. & Tsukagoshi, K. [Epitaxial Growth and Electronic Properties of Large Hexagonal Graphene Domains on Cu\(111\) Thin Film](#). *Applied Physics Express* **6**, 7 (2013).
52. Ji, H. G., Lin, Y.-C., Nagashio, K., Maruyama, M., Solís-Fernández, P., Sukma Aji, A., Panchal, V., Okada, S., Suenaga, K. & Ago, H. [Hydrogen-Assisted Epitaxial Growth of Monolayer Tungsten Disulfide and Seamless Grain Stitching](#). *Chemistry of Materials* **30**, 2 (2018).
53. Ji, H. G., Solís-Fernández, P., Erkiñç, U. & Ago, H. [Stacking Orientation-Dependent Photoluminescence Pathways in Artificially Stacked Bilayer WS<sub>2</sub> Nanosheets Grown by Chemical Vapor Deposition: Implications for Spintronics and Valleytronics](#). *ACS Applied Nano Materials* (2021).
54. Ago, H., Fukamachi, S., Endo, H., Solís-Fernández, P., Mohamad Yunus, R., Uchida, Y., Panchal, V., Kazakova, O. & Tsuji, M. [Visualization of Grain Structure and Boundaries of Polycrystalline Graphene and Two-Dimensional Materials by Epitaxial Growth of Transition Metal Dichalcogenides](#). *ACS Nano* **10**, 3 (2016).

55. Rossi, A., Büch, H., Di Rienzo, C., Miseikis, V., Convertino, D., Al-Temimy, A., Voliani, V., Gemmi, M., Piazza, V. & Coletti, C. Scalable synthesis of WS<sub>2</sub> on graphene and h-BN: an all-2D platform for light-matter transduction. *2D Materials* **3**, 3 (2016).
56. Forti, S., Rossi, A., Büch, H., Cavallucci, T., Bisio, F., Sala, A., Montes, T. O., Locatelli, A., Magnozzi, M., Canepa, M., Müller, K., Link, S., Starke, U., Tozzini, V. & Coletti, C. Electronic properties of single-layer tungsten disulfide on epitaxial graphene on silicon carbide. *Nanoscale* **9**, 42 (2017).
57. Rossi, A., Spirito, D., Bianco, F., Forti, S., Fabbri, F., Büch, H., Tredicucci, A., Krahne, R. & Coletti, C. Patterned tungsten disulfide/graphene heterostructures for efficient multifunctional optoelectronic devices. *Nanoscale* (2018).
58. Suenaga, K. K., Ji, H. G., Lin, Y.-C., Vincent, T., Maruyama, M., Aji, A. S., Shiratsuchi, Y., Ding, D., Kawahara, K., Okada, S., Panchal, V., Kazakova, O., Hibino, H., Suenaga, K. K. & Ago, H. Surface-Mediated Aligned Growth of Monolayer MoS<sub>2</sub> and In-Plane Heterostructures with Graphene on Sapphire. *ACS Nano* **12**, 10 (2018).
59. Cui, X., Lee, G.-H., Kim, Y. D., Arefe, G., Huang, P. Y., Lee, C.-H., Chenet, D. A., Zhang, X., Wang, L., Ye, F., Pizzocchero, F., Jessen, B. S., Watanabe, K., Taniguchi, T., Muller, D. A., Low, T., Kim, P. & Hone, J. Multi-terminal transport measurements of MoS<sub>2</sub> using a van der Waals heterostructure device platform. *Nature Nanotechnology* **10**, 6 (2015).
60. Chiu, M. H., Zhang, C., Shiu, H. W., Chuu, C. P., Chen, C. H., Chang, C. Y. S., Chen, C. H., Chou, M. Y., Shih, C. K. & Li, L. J. Determination of band alignment in the single-layer MoS<sub>2</sub>/WSe<sub>2</sub> heterojunction. *Nature Communications* **6**, May (2015).
61. Hill, H. M., Rigosi, A. F., Rim, K. T., Flynn, G. W. & Heinz, T. F. Band alignment in MoS<sub>2</sub>/WS<sub>2</sub> transition metal dichalcogenide heterostructures probed by scanning tunneling microscopy and spectroscopy. *Nano Letters* **16**, 8 (2016).
62. Wilson, N. R., Nguyen, P. V., Seyler, K., Rivera, P., Marsden, A. J., Laker, Z. P. L., Constantinescu, G. C., Kandyba, V., Barinov, A., Hine, N. D. M., Xu, X. & Cobden, D. H. Determination of band offsets, hybridization, and exciton binding in 2D semiconductor heterostructures. *Science Advances* **3**, 2 (2017).
63. Zhang, C., Chuu, C.-P., Ren, X., Li, M.-Y., Li, L.-J., Jin, C., Chou, M.-Y. & Shih, C.-K. Interlayer couplings, Moiré patterns, and 2D electronic superlattices in MoS<sub>2</sub>/WSe<sub>2</sub> hetero-bilayers. *Science advances* **3**, 1 (2017).
64. Dai, S., Ma, Q., Liu, M. K., Andersen, T., Fei, Z., Goldflam, M. D., Wagner, M., Watanabe, K., Taniguchi, T., Thiemens, M., Keilmann, F., Janssen, G. C., Zhu, S. E., Jarillo-Herrero, P., Fogler, M. M. & Basov, D. N. Graphene on hexagonal boron ni-

- tride as a tunable hyperbolic metamaterial. *Nature Nanotechnology* **10**, 8 (2015).
65. Dean, C. R., Wang, L., Maher, P., Forsythe, C., Ghahari, F., Gao, Y., Katoch, J., Ishigami, M., Moon, P., Koshino, M., Taniguchi, T., Watanabe, K., Shepard, K. L., Hone, J. & Kim, P. [Hofstadter's butterfly and the fractal quantum Hall effect in moiré superlattices](#). *Nature* **497**, 7451 (2013).
  66. Wang, Z., Wang, Y. B., Yin, J., Tóvári, E., Yang, Y., Lin, L., Holwill, M., Birkbeck, J., Perello, D. J., Xu, S., Zultak, J., Gorbachev, R. V., Kretinin, A. V., Taniguchi, T., Watanabe, K., Morozov, S. V., Anđelković, M., Milovanović, S. P., Covaci, L., Peeters, F. M., Mishchenko, A., Geim, A. K., Novoselov, K. S., Fal'ko, V. I., Knothe, A. & Woods, C. R. [Composite super-moiré lattices in double-aligned graphene heterostructures](#). *Science Advances* **5**, 12 (2019).
  67. Woessner, A., Alonso-González, P., Lundeberg, M. B., Gao, Y., Barrios-Vargas, J. E., Navickaite, G., Ma, Q., Janner, D., Watanabe, K., Cummings, A. W., Taniguchi, T., Pruneri, V., Roche, S., Jarillo-Herrero, P., Hone, J., Hillenbrand, R. & Koppen, F. H. L. [Near-field photocurrent nanoscopy on bare and encapsulated graphene](#). *Nature Communications* **7**, 1 (2016).
  68. Yamoah, M. A., Yang, W., Pop, E. & Goldhaber-Gordon, D. [High-Velocity Saturation in Graphene Encapsulated by Hexagonal Boron Nitride](#). *ACS Nano* **11**, 10 (2017).
  69. Wang, L., Meric, I., Huang, P. Y., Gao, Q., Gao, Y., Tran, H., Taniguchi, T., Watanabe, K., Campos, L. M., Muller, D. A., Guo, J., Kim, P., Hone, J., Shepard, K. L. & Dean, C. R. [One-Dimensional Electrical Contact to a Two-Dimensional Material](#). *Science* **342**, 6158 (2013).
  70. Khestanova, E., Guinea, F., Fumagalli, L., Geim, A. K. & Grigorieva, I. V. [Universal shape and pressure inside bubbles appearing in van der Waals heterostructures](#). *Nature Communications* **7**, 1 (2016).
  71. Rosenberger, M. R., Chuang, H.-J., McCreary, K. M., Hanbicki, A. T., Sivaram, S. V. & Jonker, B. T. [Nano-"Squeegee" for the Creation of Clean 2D Material Interfaces](#). *ACS Applied Materials & Interfaces* **10**, 12 (2018).
  72. Gasparutti, I., Song, S. H., Neumann, M., Wei, X., Watanabe, K., Taniguchi, T. & Lee, Y. H. [How Clean Is Clean? Recipes for van der Waals Heterostructure Cleanliness Assessment](#). *ACS Applied Materials & Interfaces* **12**, 6 (2020).
  73. Tyurnina, A. V., Bandurin, D. A., Khestanova, E., Kravets, V. G., Koperski, M., Guinea, F., Grigorenko, A. N., Geim, A. K. & Grigorieva, I. V. [Strained Bubbles in van der Waals Heterostructures as Local Emitters of Photoluminescence with Adjustable Wavelength](#). *ACS Photonics* **6**, 2 (2019).

74. Frisenda, R., Navarro-Moratalla, E., Gant, P., Pérez De Lara, D., Jarillo-Herrero, P., Gorbachev, R. V. & Castellanos-Gomez, A. Recent progress in the assembly of nanodevices and van der Waals heterostructures by deterministic placement of 2D materials. *Chemical Society Reviews* **47**, 1 (2018).
75. Kim, K., Yankowitz, M., Fallahazad, B., Kang, S., Movva, H. C. P., Huang, S., Larentis, S., Corbet, C. M., Taniguchi, T., Watanabe, K., Banerjee, S. K., LeRoy, B. J. & Tutuc, E. van der Waals Heterostructures with High Accuracy Rotational Alignment. *Nano Letters* **16**, 3 (2016).
76. Binnig, G. & Rohrer, H. Scanning tunneling microscopy. *Surface Science* **126**, 1–3 (1983).
77. Binnig, G., Quate, C. F. & Gerber, C. Atomic Force Microscope. *Physical Review Letters* **56**, 9 (1986).
78. Zurich Instruments. Principles of lock-in detection and the state of the art (white paper) <https://www.zhinst.com/europe/en/resources/principles-of-lock-in-detection> (5th Jan. 2022).
79. Keilmann, F. & Hillenbrand, R. Near-field microscopy by elastic light scattering from a tip. *Philosophical Transactions of the Royal Society of London. Series A: Mathematical, Physical and Engineering Sciences* **362**, 1817 (2004).
80. Cvitkovic, A., Ocelic, N. & Hillenbrand, R. Analytical model for quantitative prediction of material contrasts in scattering-type near-field optical microscopy. *Optics Express* **15**, 14 (2007).
81. Hauer, B., Engelhardt, A. P. & Taubner, T. Quasi-analytical model for scattering infrared near-field microscopy on layered systems. *Optics Express* **20**, 12 (2012).
82. Mester, L., Govyadinov, A. A., Chen, S., Goikoetxea, M. & Hillenbrand, R. Subsurface chemical nanoidentification by nano-FTIR spectroscopy. *Nature Communications* **11**, 1 (2020).
83. Aubert, S., Bruyant, A., Blaize, S., Bachelot, R., Lerondel, G., Hudlet, S. & Royer, P. Analysis of the interferometric effect of the background light in apertureless scanning near-field optical microscopy. *Journal of the Optical Society of America B* **20**, 10 (2003).
84. Ocelic, N., Huber, A. & Hillenbrand, R. Pseudoheterodyne detection for background-free near-field spectroscopy. *Applied Physics Letters* **89**, 10 (2006).
85. Dazzi, A., Prater, C. B., Hu, Q., Chase, D. B., Rabolt, J. F. & Marcott, C. AFM-IR: Combining Atomic Force Microscopy and Infrared Spectroscopy for Nanoscale Chemical Characterization. *Applied Spectroscopy* **66**, 12 (2012).
86. Dazzi, A. & Prater, C. B. AFM-IR: Technology and Applications in Nanoscale Infrared Spectroscopy and Chemical Imaging. *Chemical Reviews* **117**, 7 (2017).

87. Rosenberger, M. R., Wang, M. C., Xie, X., Rogers, J. A., Nam, S. & King, W. P. [Measuring individual carbon nanotubes and single graphene sheets using atomic force microscope infrared spectroscopy](#). *Nanotechnology* **28**, 35 (2017).
88. Schwartz, J. J., Chuang, H.-J., Rosenberger, M. R., Sivaram, S. V., McCreary, K. M., Jonker, B. T. & Centrone, A. [Chemical Identification of Interlayer Contaminants within van der Waals Heterostructures](#). *ACS Applied Materials & Interfaces* **11**, 28 (2019).
89. Woods, C. R., Britnell, L., Eckmann, A., Ma, R. S., Lu, J. C., Guo, H. M., Lin, X., Yu, G. L., Cao, Y., Gorbachev, R. V., Kretinin, A. V., Park, J., Ponomarenko, L. A., Katsnelson, M. I., Gornostyrev, Y. N., Watanabe, K., Taniguchi, T., Casiraghi, C., Gao, H.-J., Geim, A. K. & Novoselov, K. S. [Commensurate-incommensurate transition in graphene on hexagonal boron nitride](#). *Nature Physics* **10**, 6 (2014).
90. Panchal, V., Pearce, R., Yakimova, R., Tzalenchuk, A. & Kazakova, O. [Standardization of surface potential measurements of graphene domains](#). *Scientific Reports* **3**, 1 (2013).
91. Son, Y., Wang, Q. H., Paulson, J. A., Shih, C.-J., Rajan, A. G., Tvrđy, K., Kim, S., Alfeeli, B., Braatz, R. D. & Strano, M. S. [Layer Number Dependence of MoS<sub>2</sub> Photoconductivity Using Photocurrent Spectral Atomic Force Microscopic Imaging](#). *ACS Nano* **9**, 3 (2015).
92. Ferrari, A. C. & Basko, D. M. [Raman spectroscopy as a versatile tool for studying the properties of graphene](#). *Nature Nanotechnology* **8**, 4 (2013).
93. Jorio, A., Saito, R., Dresselhaus, G. & Dresselhaus, M. S. *Raman Spectroscopy in Graphene Related Systems* ISBN: 9783527632695 (Wiley-VCH Verlag GmbH & Co. KGaA, 2011).
94. Vincent, T., Panchal, V., Booth, T., Power, S. R., Jauho, A.-p., Antonov, V. & Kazakova, O. [Probing the nanoscale origin of strain and doping in graphene-hBN heterostructures](#). *2D Materials* **6**, 1 (2018).
95. Baffou, G. [Anti-Stokes Thermometry in Nanoplasmonics](#). *ACS Nano* **15**, 4 (2021).
96. Mueller, T. & Malic, E. [Exciton physics and device application of two-dimensional transition metal dichalcogenide semiconductors](#). *npj 2D Materials and Applications* **2**, 1 (2018).
97. Miranda, H. *Phonon website* <https://henriquemiranda.github.io/phononwebsite/> (24th Dec. 2021).
98. Ferrari, A. C., Meyer, J. C., Scardaci, V., Casiraghi, C., Lazzeri, M., Mauri, F., Piscanec, S., Jiang, D., Novoselov, K. S., Roth, S. & Geim, A. K. [Raman spectrum of graphene and graphene layers](#). *Physical Review Letters* **97**, 18 (2006).

99. Hao, Y., Wang, Y., Wang, L., Ni, Z., Wang, Z., Wang, R., Koo, C. K., Shen, Z. & Thong, J. T. L. [Probing Layer Number and Stacking Order of Few-Layer Graphene by Raman Spectroscopy](#). *Small* **6**, 2 (2010).
100. Wang, Y. Y., Ni, Z. H., Yu, T., Shen, Z. X., Wang, H. M., Wu, Y. H., Chen, W. & Wee, A. T. S. [Raman studies of monolayer graphene: The substrate effect](#). *Journal of Physical Chemistry C* **112**, 29 (2008).
101. Banszerus, L., Janssen, H., Otto, M., Epping, A., Taniguchi, T., Watanabe, K., Beschoten, B., Neumaier, D. & Stampfer, C. [Identifying suitable substrates for high-quality graphene-based heterostructures](#). *2D Materials* **4**, 2 (2017).
102. Havener, R. W., Zhuang, H., Brown, L., Hennig, R. G. & Park, J. [Angle-Resolved Raman Imaging of Interlayer Rotations and Interactions in Twisted Bilayer Graphene](#). *Nano Letters* **12**, 6 (2012).
103. Kim, K., Coh, S., Tan, L. Z., Regan, W., Yuk, J. M., Chatterjee, E., Crommie, M. F., Cohen, M. L., Louie, S. G. & Zettl, A. [Raman Spectroscopy Study of Rotated Double-Layer Graphene: Misorientation-Angle Dependence of Electronic Structure](#). *Physical Review Letters* **108**, 24 (2012).
104. Cong, C. & Yu, T. [Evolution of Raman G and G' \(2D\) modes in folded graphene layers](#). *Physical Review B - Condensed Matter and Materials Physics* **89**, 23 (2014).
105. Beechem, T. E., Ohta, T., Diaconescu, B. & Robinson, J. T. [Rotational Disorder in Twisted Bilayer Graphene](#). *ACS Nano* **8**, 2 (2014).
106. Mohiuddin, T. M. G., Lombardo, A., Nair, R. R., Bonetti, A., Savini, G., Jalil, R., Bonini, N., Basko, D. M., Galiotis, C., Marzari, N., Novoselov, K. S., Geim, A. K. & Ferrari, A. C. [Uniaxial strain in graphene by Raman spectroscopy: G peak splitting, Grüneisen parameters, and sample orientation](#). *Physical Review B - Condensed Matter and Materials Physics* **79**, 20 (2009).
107. Ding, F., Ji, H., Chen, Y., Herklotz, A., Dörr, K., Mei, Y., Rastelli, A. & Schmidt, O. G. [Stretchable graphene: A close look at fundamental parameters through biaxial straining](#). *Nano Letters* **10**, 9 (2010).
108. Mueller, N. S., Heeg, S., Alvarez, M. P., Kusch, P., Wasserroth, S., Clark, N., Schedin, F., Parthenios, J., Papagelis, K., Galiotis, C., Kalbáč, M., Vijayaraghavan, A., Huebner, U., Gorbachev, R., Frank, O. & Reich, S. [Evaluating arbitrary strain configurations and doping in graphene with Raman spectroscopy](#). *2D Materials* **5**, 1 (2017).
109. Huang, M., Yan, H., Chen, C., Song, D., Heinz, T. F. & Hone, J. [Phonon softening and crystallographic orientation of strained graphene studied by Raman spectroscopy](#). *Proceedings of the National Academy of Sciences* **106**, 18 (2009).

110. Huang, M., Yan, H., Heinz, T. F. & Hone, J. [Probing strain-induced electronic structure change in graphene by Raman spectroscopy](#). *Nano Letters* **10**, 10 (2010).
111. Mohr, M., Maultzsch, J. & Thomsen, C. [Splitting of the Raman 2D band of graphene subjected to strain](#). *Physical Review B - Condensed Matter and Materials Physics* **82**, 20 (2010).
112. Frank, O., Mohr, M., Maultzsch, J., Thomsen, C., Riaz, I., Jalil, R., Novoselov, K. S., Tsoukleri, G., Parthenios, J., Papagelis, K., Kavan, L. & Galiotis, C. [Raman 2D-band splitting in graphene: Theory and experiment](#). *ACS Nano* **5**, 3 (2011).
113. Mogg, L., Zhang, S., Hao, G.-P., Gopinadhan, K., Barry, D., Liu, B. L., Cheng, H. M., Geim, A. K. & Lozada-Hidalgo, M. [Perfect proton selectivity in ion transport through two-dimensional crystals](#). *Nature Communications* **10**, 1 (2019).
114. Froehlicher, G. & Berciaud, S. [Raman spectroscopy of electrochemically gated graphene transistors: Geometrical capacitance, electron-phonon, electron-electron, and electron-defect scattering](#). *Physical Review B - Condensed Matter and Materials Physics* **91**, 20 (2015).
115. Lazzeri, M. & Mauri, F. [Nonadiabatic Kohn anomaly in a doped graphene monolayer](#). *Physical Review Letters* **97**, 26 (2006).
116. Pisana, S., Lazzeri, M., Casiraghi, C., Novoselov, K. S., Geim, A. K., Ferrari, A. C. & Mauri, F. [Breakdown of the adiabatic Born-Oppenheimer approximation in graphene](#). *Nature Materials* **6**, 3 (2007).
117. Yan, J., Zhang, Y., Kim, P. & Pinczuk, A. [Electric Field Effect Tuning of Electron-Phonon Coupling in Graphene](#). *Physical Review Letters* **98**, 16 (2007).
118. Das, A., Pisana, S., Chakraborty, B., Piscanec, S., Saha, S. K., Waghmare, U. V., Novoselov, K. S., Krishnamurthy, H. R., Geim, A. K., Ferrari, A. C. & Sood, A. K. [Monitoring dopants by Raman scattering in an electrochemically top-gated graphene transistor](#). *Nature Nanotechnology* **3**, 4 (2008).
119. Couto, N. J. G., Costanzo, D., Engels, S., Ki, D. K., Watanabe, K., Taniguchi, T., Stampfer, C., Guinea, F. & Morpurgo, A. F. [Random strain fluctuations as dominant disorder source for high-quality on-substrate graphene devices](#). *Physical Review X* **4**, 4 (2014).
120. Neumann, C., Reichardt, S., Venezuela, P., Drögeler, M., Banzerus, L., Schmitz, M., Watanabe, K., Taniguchi, T., Mauri, F., Beschoten, B., Rotkin, S. V. & Stampfer, C. [Raman spectroscopy as probe of nanometre-scale strain variations in graphene](#). *Nature Communications* **6**, May (2015).

121. Ahn, G., Kim, H. R., Ko, T. Y., Choi, K., Watanabe, K., Taniguchi, T., Hong, B. H. & Ryu, S. [Optical probing of the electronic interaction between graphene and hexagonal boron nitride.](#) *ACS Nano* **7**, 2 (2013).
122. Bao, W., Miao, F., Chen, Z., Zhang, H., Jang, W., Dames, C. & Lau, C. N. [Controlled ripple texturing of suspended graphene and ultrathin graphite membranes.](#) *Nature Nanotechnology* **4**, 9 (2009).
123. Fei, Z., Foley, J. J., Gannett, W., Liu, M. K., Dai, S., Ni, G. X., Zettl, A., Fogler, M. M., Wiederrecht, G. P., Gray, S. K. & Basov, D. N. [Ultraconfined Plasmonic Hotspots Inside Graphene Nanobubbles.](#) *Nano Letters* **16**, 12 (2016).
124. Si, C., Sun, Z. & Liu, F. [Strain engineering of graphene: a review.](#) *Nanoscale* **8**, 6 (2016).
125. Schneider, M., Faria, D., Viola Kusminskiy, S. & Sandler, N. [Local sublattice symmetry breaking for graphene with a centrosymmetric deformation.](#) *Physical Review B - Condensed Matter and Materials Physics* **91**, 16 (2015).
126. Settnes, M., Power, S. R. & Jauho, A. P. [Pseudomagnetic fields and triaxial strain in graphene.](#) *Physical Review B* **93**, 3 (2016).
127. Qi, Z., Bahamon, D. A., Pereira, V. M., Park, H. S., Campbell, D. K. & Neto, A. H. C. [Resonant Tunneling in Graphene Pseudomagnetic Quantum Dots.](#) *Nano Letters* **13**, 6 (2013).
128. Lee, J. E., Ahn, G., Shim, J., Lee, Y. S. & Ryu, S. [Optical separation of mechanical strain from charge doping in graphene.](#) *Nature Communications* **3**, 1 (2012).
129. De Sanctis, A., Mehew, J. D., Alkhalifa, S., Withers, F., Craciun, M. F. & Russo, S. [Strain-Engineering of Twist-Angle in Graphene/hBN Superlattice Devices.](#) *Nano Letters* **18**, 12 (2018).
130. Vincent, T., Hamer, M., Grigorieva, I., Antonov, V., Tzalenchuk, A. & Kazakova, O. [Strongly Absorbing Nanoscale Infrared Domains within Strained Bubbles at hBN–Graphene Interfaces.](#) *ACS Applied Materials & Interfaces* **12**, 51 (2020).
131. Brown, K., Vincent, T., Castanon, E. G., Rus, F. S., Melios, C., Kazakova, O. & Giusca, C. E. [Contactless probing of graphene charge density variation in a controlled humidity environment.](#) *Carbon* **163** (2020).
132. Ali, M. M., Mitchell, J. J., Burwell, G., Rejnhard, K., Jenkins, C. A., Daghigh Ahmadi, E., Sharma, S. & Guy, O. J. [Application of Molecular Vapour Deposited Al<sub>2</sub>O<sub>3</sub> for Graphene-Based Biosensor Passivation and Improvements in Graphene Device Homogeneity.](#) *Nanomaterials* **11**, 8 (2021).
133. Goodwin, D. M., Walters, F., Ali, M. M., Daghigh Ahmadi, E. & Guy, O. J. [Graphene bioelectronic nose for the detection of odorants with human olfactory receptor 2ag1.](#) *Chemosensors* **9**, 7 (2021).

134. Ryu, S., Liu, L., Berciaud, S., Yu, Y.-J., Liu, H., Kim, P., Flynn, G. W. & Brus, L. E. [Atmospheric Oxygen Binding and Hole Doping in Deformed Graphene on a SiO<sub>2</sub> Substrate](#). *Nano Letters* **10**, 12 (2010).
135. Metzger, C., Rémi, S., Liu, M., Kusminskiy, S. V., Castro Neto, A. H., Swan, A. K. & Goldberg, B. B. [Biaxial strain in graphene adhered to shallow depressions](#). *Nano Letters* **10**, 1 (2010).
136. Zabel, J., Nair, R. R., Ott, A., Georgiou, T., Geim, A. K., Novoselov, K. S. & Casiraghi, C. [Raman spectroscopy of graphene and bilayer under biaxial strain: Bubbles and balloons](#). *Nano Letters* **12**, 2 (2012).
137. Forster, F., Molina-Sanchez, A., Engels, S., Epping, A., Watanabe, K., Taniguchi, T., Wirtz, L. & Stampfer, C. [Dielectric screening of the Kohn anomaly of graphene on hexagonal boron nitride](#). *Physical Review B - Condensed Matter and Materials Physics* **88**, 8 (2013).
138. Gorbachev, R. V., Riaz, I., Nair, R. R., Jalil, R., Britnell, L., Belle, B. D., Hill, E. W., Novoselov, K. S., Watanabe, K., Taniguchi, T., Geim, A. K. & Blake, P. [Hunting for Monolayer Boron Nitride: Optical and Raman Signatures](#). *Small* **7**, 4 (2011).
139. Pizzocchero, F., Gammelgaard, L., Jessen, B. S., Caridad, J. M., Wang, L., Hone, J., Bøggild, P. & Booth, T. J. [The hot pick-up technique for batch assembly of van der Waals heterostructures](#). *Nature Communications* **7**, May (2016).
140. Yankowitz, M., Ma, Q., Jarillo-Herrero, P. & LeRoy, B. J. [van der Waals heterostructures combining graphene and hexagonal boron nitride](#). *Nature Reviews Physics* **1**, 2 (2019).
141. Moldovan, D., Ramezani Masir, M. & Peeters, F. M. [Electronic states in a graphene flake strained by a Gaussian bump](#). *Physical Review B* **88**, 3 (2013).
142. Carrillo-Bastos, R., Faria, D., Latgé, A., Mireles, F. & Sandler, N. [Gaussian deformations in graphene ribbons: Flowers and confinement](#). *Physical Review B* **90**, 4 (2014).
143. Settnes, M., Power, S. R., Lin, J., Petersen, D. H. & Jauho, A.-P. [Patched Green's function techniques for two-dimensional systems: Electronic behavior of bubbles and perforations in graphene](#). *Physical Review B* **91**, 12 (2015).
144. Kim, E.-A. & Castro Neto, A. H. [Graphene as an electronic membrane](#). *EPL (Europhysics Letters)* **84**, 5 (2008).
145. Crommie, M. F., Lutz, C. P. & Eigler, D. M. [Confinement of Electrons to Quantum Corrals on a Metal Surface](#). *Science* **262**, 5131 (1993).
146. Jolie, W., Craes, F., Petrović, M., Atodiresei, N., Caciuc, V., Blügel, S., Kralj, M., Michely, T. & Busse, C. [Confinement of Dirac electrons in graphene quantum dots](#). *Physical Review B* **89**, 15 (2014).

147. Huang, Y., Wang, X., Zhang, X., Chen, X., Li, B., Wang, B., Huang, M., Zhu, C., Zhang, X., Bacsá, W. S., Ding, F. & Ruoff, R. S. [Raman Spectral Band Oscillations in Large Graphene Bubbles](#). *Physical Review Letters* **120**, 18 (2018).
148. Wu, Q., Wu, Y., Hao, Y., Geng, J., Charlton, M., Chen, S., Ren, Y., Ji, H., Li, H., Boukhvalov, D. W., Piner, R. D., Bielawski, C. W. & Ruoff, R. S. [Selective surface functionalization at regions of high local curvature in graphene](#). *Chem. Commun.* **49**, 7 (2013).
149. Yankowitz, M., Watanabe, K., Taniguchi, T., San-Jose, P. & LeRoy, B. J. [Pressure-induced commensurate stacking of graphene on boron nitride](#). *Nature Communications* **7** (2016).
150. Zheng, F., Sasaki, K.-i., Saito, R., Duan, W. & Gu, B.-L. [Edge States of Zigzag Boron Nitride Nanoribbons](#). *Journal of the Physical Society of Japan* **78**, 7 (2009).
151. Basov, D. N., Fogler, M. M. & García De Abajo, F. J. [Polaritons in van der Waals materials](#). *Science* **354**, 6309 (2016).
152. Fei, Z., Rodin, A. S., Andreev, G. O., Bao, W., McLeod, A. S., Wagner, M., Zhang, L. M., Zhao, Z., Thiemens, M., Dominguez, G., Fogler, M. M., Castro Neto, A. H., Lau, C. N., Keilmann, F. & Basov, D. N. [Gate-tuning of graphene plasmons revealed by infrared nano-imaging](#). *Nature* **486**, 7405 (2012).
153. Grigorenko, A. N., Polini, M. & Novoselov, K. S. [Graphene plasmonics](#). *Nature Photonics* **6**, 11 (2012).
154. Dai, S., Fei, Z., Ma, Q., Rodin, A. S., Wagner, M., McLeod, A. S., Liu, M. K., Gannett, W., Regan, W., Watanabe, K., Taniguchi, T., Thiemens, M., Dominguez, G., Neto, A. H. C., Zettl, A., Keilmann, F., Jarillo-Herrero, P., Fogler, M. M. & Basov, D. N. [Tunable Phonon Polaritons in Atomically Thin van der Waals Crystals of Boron Nitride](#). *Science* **343**, 6175 (2014).
155. Li, P., Lewin, M., Kretinin, A. V., Caldwell, J. D., Novoselov, K. S., Taniguchi, T., Watanabe, K., Gaussmann, F. & Taubner, T. [Hyperbolic phonon-polaritons in boron nitride for near-field optical imaging and focusing](#). *Nature Communications* **6**, 1 (2015).
156. Ni, G. X., Wang, H., Wu, J. S., Fei, Z., Goldflam, M. D., Keilmann, F., Özyilmaz, B., Castro Neto, A. H., Xie, X. M., Fogler, M. M. & Basov, D. N. [Plasmons in graphene moiré superlattices](#). *Nature Materials* **14**, 12 (2015).
157. Woessner, A., Parret, R., Davydovskaya, D., Gao, Y., Wu, J.-S., Lundberg, M. B., Nanot, S., Alonso-González, P., Watanabe, K., Taniguchi, T., Hillenbrand, R., Fogler, M. M., Hone, J. & Koppens, F. H. L. [Electrical detection of hyperbolic phonon-polaritons in heterostructures of graphene and boron nitride](#). *npj 2D Materials and Applications* **1**, 1 (2017).

158. Wang, L., Chen, X. & Lu, W. [Intrinsic photo-conductance triggered by the plasmonic effect in graphene for terahertz detection](#). *Nanotechnology* **27**, 3 (2016).
159. Lundeberg, M. B., Gao, Y., Woessner, A., Tan, C., Alonso-González, P., Watanabe, K., Taniguchi, T., Hone, J., Hillenbrand, R. & Koppens, F. H. L. [Thermoelectric detection and imaging of propagating graphene plasmons](#). *Nature Materials* **16**, 2 (2017).
160. Lyu, B., Li, H., Jiang, L., Shan, W., Hu, C., Deng, A., Ying, Z., Wang, L., Zhang, Y., Bechtel, H. A., Martin, M. C., Taniguchi, T., Watanabe, K., Luo, W., Wang, F. & Shi, Z. [Phonon Polariton-assisted Infrared Nanoimaging of Local Strain in Hexagonal Boron Nitride](#). *Nano Letters* **19**, 3 (2019).
161. Slipchenko, T. M., Nesterov, M. L., Hillenbrand, R., Nikitin, A. Y. & Martín-Moreno, L. [Graphene Plasmon Reflection by Corrugations](#). *ACS Photonics* **4**, 12 (2017).
162. Budrikis, Z., Sellerio, A. L., Bertalan, Z. & Zapperi, S. [Wrinkle motifs in thin films](#). *Scientific Reports* **5**, 1 (2015).
163. Freitag, N. M., Reisch, T., Chizhova, L. A., Nemes-Incze, P., Holl, C., Woods, C. R., Gorbachev, R. V., Cao, Y., Geim, A. K., Novoselov, K. S., Burgdörfer, J., Libisch, F. & Morgenstern, M. [Large tunable valley splitting in edge-free graphene quantum dots on boron nitride](#). *Nature Nanotechnology* **13**, 5 (2018).
164. Li, S. Y., Su, Y., Ren, Y. N. & He, L. [Valley Polarization and Inversion in Strained Graphene via Pseudo-Landau Levels, Valley Splitting of Real Landau Levels, and Confined States](#). *Physical Review Letters* **124**, 10 (2020).
165. Jiang, Y., Mao, J., Duan, J., Lai, X., Watanabe, K., Taniguchi, T. & Andrei, E. Y. [Visualizing Strain-Induced Pseudomagnetic Fields in Graphene through an hBN Magnifying Glass](#). *Nano Letters* **17**, 5 (2017).
166. Zhang, Y., Heiranian, M., Janicek, B., Budrikis, Z., Zapperi, S., Huang, P. Y., Johnson, H. T., Aluru, N. R., Lyding, J. W. & Mason, N. [Strain Modulation of Graphene by Nanoscale Substrate Curvatures: A Molecular View](#). *Nano Letters* **18**, 3 (2018).
167. Zhang, Y., Kim, Y., Gilbert, M. J. & Mason, N. [Magnetotransport in a strain superlattice of graphene](#). *Applied Physics Letters* **115**, 14 (2019).
168. Milovanović, S. P., Covaci, L. & Peeters, F. M. [Strain fields in graphene induced by nanopillar mesh](#). *Journal of Applied Physics* **125**, 8 (2019).
169. Mao, J., Milovanović, S. P., Anđelković, M., Lai, X., Cao, Y., Watanabe, K., Taniguchi, T., Covaci, L., Peeters, F. M., Geim, A. K., Jiang, Y. & Andrei, E. Y. [Evidence of flat bands and correlated states in buckled graphene superlattices](#). *Nature* **584**, 7820 (2020).

170. Mihai, L. A. & Goriely, A. [How to characterize a nonlinear elastic material? A review on nonlinear constitutive parameters in isotropic finite elasticity](#). *Proceedings of the Royal Society A: Mathematical, Physical and Engineering Sciences* **473**, 2207 (2017).
171. Dempster, A. P., Laird, N. M. & Rubin, D. B. [Maximum Likelihood from Incomplete Data Via the EM Algorithm](#). *Journal of the Royal Statistical Society: Series B (Methodological)* **39**, 1 (1977).
172. Huth, F., Govyadinov, A., Amarie, S., Nuansing, W., Keilmann, F. & Hillenbrand, R. [Nano-FTIR Absorption Spectroscopy of Molecular Fingerprints at 20 nm Spatial Resolution](#). *Nano Letters* **12**, 8 (2012).
173. Govyadinov, A. A., Amenabar, I., Huth, F., Carney, P. S. & Hillenbrand, R. [Quantitative Measurement of Local Infrared Absorption and Dielectric Function with Tip-Enhanced Near-Field Microscopy](#). *The Journal of Physical Chemistry Letters* **4**, 9 (2013).
174. Mastel, S., Govyadinov, A. A., de Oliveira, T. V. A. G., Amenabar, I. & Hillenbrand, R. [Nanoscale-resolved chemical identification of thin organic films using infrared near-field spectroscopy and standard Fourier transform infrared references](#). *Applied Physics Letters* **106**, 2 (2015).
175. Suzuura, H. & Ando, T. [Phonons and electron-phonon scattering in carbon nanotubes](#). *Physical Review B* **65**, 23 (2002).
176. Joung, D., Nemilentsau, A., Agarwal, K., Dai, C., Liu, C., Su, Q., Li, J., Low, T., Koester, S. J. & Cho, J.-H. [Self-Assembled Three-Dimensional Graphene-Based Polyhedrons Inducing Volumetric Light Confinement](#). *Nano Letters* **17**, 3 (2017).
177. Xiong, L., Forsythe, C., Jung, M., McLeod, A. S., Sunku, S. S., Shao, Y. M., Ni, G. X., Sternbach, A. J., Liu, S., Edgar, J. H., Mele, E. J., Fogler, M. M., Shvets, G., Dean, C. R. & Basov, D. N. [Photonic crystal for graphene plasmons](#). *Nature Communications* **10**, 1 (2019).
178. Yan, H., Li, X., Chandra, B., Tulevski, G., Wu, Y., Freitag, M., Zhu, W., Avouris, P. & Xia, F. [Tunable infrared plasmonic devices using graphene/insulator stacks](#). *Nature Nanotechnology* **7**, 5 (2012).
179. Kim, S., Jang, M. S., Brar, V. W., Mauser, K. W., Kim, L. & Atwater, H. A. [Electronically Tunable Perfect Absorption in Graphene](#). *Nano Letters* **18**, 2 (2018).
180. Androulidakis, C., Koukaras, E. N., Parthenios, J., Kalosakas, G., Papagelis, K. & Galiotis, C. [Graphene flakes under controlled biaxial deformation](#). *Scientific Reports* **5** (2015).

181. Hu, H., Yu, R., Teng, H., Hu, D., Chen, N., Qu, Y., Yang, X., Chen, X., McLeod, A. S., Alonso-González, P., Guo, X., Li, C., Yao, Z., Li, Z., Chen, J., Sun, Z., Liu, M., García de Abajo, F. J. & Dai, Q. [Active control of micrometer plasmon propagation in suspended graphene](#). *Nature Communications* **13**, 1 (2022).
182. Mudd, G. W., Svatek, S. A., Hague, L., Makarovskiy, O., Kudrynskiy, Z. R., Mellor, C. J., Beton, P. H., Eaves, L., Novoselov, K. S., Kovalyuk, Z. D., Vdovin, E. E., Marsden, A. J., Wilson, N. R. & Patané, A. [High Broad-Band Photoresponsivity of Mechanically Formed InSe-Graphene van der Waals Heterostructures](#). *Advanced Materials* **27**, 25 (2015).
183. Tamalampudi, S. R., Lu, Y. Y., Kumar U., R., Sankar, R., Liao, C. D., Moorthy B., K., Cheng, C. H., Chou, F. C. & Chen, Y. T. [High performance and bendable few-layered InSe photodetectors with broad spectral response](#). *Nano Letters* **14**, 5 (2014).
184. Feng, W., Zheng, W., Cao, W. & Hu, P. [Back Gated Multilayer InSe Transistors with Enhanced Carrier Mobilities via the Suppression of Carrier Scattering from a Dielectric Interface](#). *Advanced Materials* **26**, 38 (2014).
185. Li, Y., Wang, T., Wu, M., Cao, T., Chen, Y., Sankar, R., Ulaganathan, R. K., Chou, F., Wetzels, C., Xu, C.-Y. Y., Louie, S. G. & Shi, S.-F. F. [Ultrasensitive tunability of the direct bandgap of 2D InSe flakes via strain engineering](#). *2D Materials* **5**, 2 (2018).
186. Wang, Q., Han, L., Wu, L., Zhang, T., Li, S. & Lu, P. [Strain Effect on Thermoelectric Performance of InSe Monolayer](#). *Nano-scale Research Letters* **14**, 1 (2019).
187. Zeng, Z., Li, S., Tadano, T. & Chen, Y. [Anharmonic lattice dynamics and thermal transport of monolayer InSe under equibiaxial tensile strains](#). *Journal of Physics Condensed Matter* **32**, 47 (2020).
188. Botcha, V. D., Zhang, M., Li, K., Gu, H., Huang, Z., Cai, J., Lu, Y., Yu, W. & Liu, X. [High-K substrate effect on thermal properties of 2D InSe few layer](#). *Journal of Alloys and Compounds* **735** (2018).
189. Li, K., Hong, Y., Li, Z. & Liu, X. [Thermal property engineering of InSe layer by a thin Al<sub>2</sub>O<sub>3</sub> stress liner](#). *Applied Physics Letters* **113**, 2 (2018).
190. Song, C., Fan, F., Xuan, N., Huang, S., Wang, C., Zhang, G., Wang, F., Xing, Q., Lei, Y., Sun, Z., Wu, H. & Yan, H. [Drastic enhancement of the Raman intensity in few-layer InSe by uniaxial strain](#). *Physical Review B* **99**, 19 (2019).
191. Mazumder, D., Xie, J., Kudrynskiy, Z. R., Wang, X., Makarovskiy, O., Bhuiyan, M. A., Kim, H., Chang, T., Huffaker, D. L., Kovalyuk, Z. D., Zhang, L. & Patané, A. [Enhanced Optical Emission from 2D InSe Bent onto Si-Pillars](#). *Advanced Optical Materials* **8**, 18 (2020).

192. Zheng, T., Wu, Z. T., Nan, H. Y., Yu, Y. F., Zafar, A., Yan, Z. Z., Lu, J. P. & Ni, Z. H. [Layer-number dependent and structural defect related optical properties of InSe](#). *RSC Advances* **7**, 87 (2017).
193. Sánchez-Royo, J. F., Muñoz-Matutano, G., Brotons-Gisbert, M., Martínez-Pastor, J. P., Segura, A., Cantarero, A., Mata, R., Canet-Ferrer, J., Tobias, G., Canadell, E., Marqués-Hueso, J. & Gerardot, B. D. [Electronic structure, optical properties, and lattice dynamics in atomically thin indium selenide flakes](#). *Nano Research* **7**, 10 (2014).
194. Balakrishnan, N., Kudrynskiy, Z. R., Smith, E. F., Fay, M. W., Makarovskiy, O., Kovalyuk, Z. D., Eaves, L., Beton, P. H. & Patané, A. [Engineering p-n junctions and bandgap tuning of InSe nanolayers by controlled oxidation](#). *2D Materials* **4**, 2 (2017).
195. Padhi, B., Setty, C. & Phillips, P. W. [Doped Twisted Bilayer Graphene near Magic Angles: Proximity to Wigner Crystallization, Not Mott Insulation](#). *Nano Letters* **18**, 10 (2018).
196. Jiang, Y., Lai, X., Watanabe, K., Taniguchi, T., Haule, K., Mao, J. & Andrei, E. Y. [Charge order and broken rotational symmetry in magic-angle twisted bilayer graphene](#). *Nature* **573**, 7772 (2019).
197. Kerelsky, A., McGilly, L. J., Kennes, D. M., Xian, L., Yankowitz, M., Chen, S., Watanabe, K., Taniguchi, T., Hone, J., Dean, C., Rubio, A. & Pasupathy, A. N. [Maximized electron interactions at the magic angle in twisted bilayer graphene](#). *Nature* **572**, 7767 (2019).
198. Lu, X., Stepanov, P., Yang, W., Xie, M., Aamir, M. A., Das, I., Urgell, C., Watanabe, K., Taniguchi, T., Zhang, G., Bachtold, A., MacDonald, A. H. & Efetov, D. K. [Superconductors, orbital magnets and correlated states in magic-angle bilayer graphene](#). *Nature* **574**, 7780 (2019).
199. Xie, Y., Lian, B., Jäck, B., Liu, X., Chiu, C.-L., Watanabe, K., Taniguchi, T., Bernevig, B. A. & Yazdani, A. [Spectroscopic signatures of many-body correlations in magic-angle twisted bilayer graphene](#). *Nature* **572**, 7767 (2019).
200. Arora, H. S., Polski, R., Zhang, Y., Thomson, A., Choi, Y., Kim, H., Lin, Z., Wilson, I. Z., Xu, X., Chu, J.-H., Watanabe, K., Taniguchi, T., Alicea, J. & Nadj-Perge, S. [Superconductivity in metallic twisted bilayer graphene stabilized by WSe<sub>2</sub>](#). *Nature* **583**, 7816 (2020).
201. Stepanov, P., Das, I., Lu, X., Fahimniya, A., Watanabe, K., Taniguchi, T., Koppens, F. H. L., Lischner, J., Levitov, L. & Efetov, D. K. [Untying the insulating and superconducting orders in magic-angle graphene](#). *Nature* **583**, 7816 (2020).

202. Yin, J., Wang, H., Peng, H., Tan, Z., Liao, L., Lin, L., Sun, X., Koh, A. L., Chen, Y., Peng, H. & Liu, Z. [Selectively enhanced photocurrent generation in twisted bilayer graphene with van Hove singularity](#). *Nature Communications* **7**, 1 (2016).
203. Jin, C., Regan, E. C., Yan, A., Iqbal Bakti Utama, M., Wang, D., Zhao, S., Qin, Y., Yang, S., Zheng, Z., Shi, S., Watanabe, K., Taniguchi, T., Tongay, S., Zettl, A. & Wang, F. [Observation of moiré excitons in WSe<sub>2</sub>/WS<sub>2</sub> heterostructure superlattices](#). *Nature* **567**, 7746 (2019).
204. Shimazaki, Y., Schwartz, I., Watanabe, K., Taniguchi, T., Kroner, M. & Imamoğlu, A. [Strongly correlated electrons and hybrid excitons in a moiré heterostructure](#). *Nature* **580**, 7804 (2020).
205. Wang, L., Shih, E.-M. M., Ghiotto, A., Xian, L., Rhodes, D. A., Tan, C., Claassen, M., Kennes, D. M., Bai, Y., Kim, B., Watanabe, K., Taniguchi, T., Zhu, X., Hone, J., Rubio, A., Pasupathy, A. N. & Dean, C. R. [Correlated electronic phases in twisted bilayer transition metal dichalcogenides](#). *Nature Materials* **19**, 8 (2020).
206. Zhang, Z., Wang, Y., Watanabe, K., Taniguchi, T., Ueno, K., Tutuc, E. & LeRoy, B. J. [Flat bands in twisted bilayer transition metal dichalcogenides](#). *Nature Physics* **16**, 11 (2020).
207. Sheremetyeva, N., Lamparski, M., Daniels, C., Van Troeye, B. & Meunier, V. [Machine-learning models for Raman spectra analysis of twisted bilayer graphene](#). *Carbon* **169** (2020).
208. De Maesschalck, R., Jouan-Rimbaud, D. & Massart, D. [The Mahalanobis distance](#). *Chemometrics and Intelligent Laboratory Systems* **50**, 1 (2000).
209. McGrory, C. A. & Titterton, D. M. [Variational approximations in Bayesian model selection for finite mixture distributions](#). *Computational Statistics and Data Analysis* **51**, 11 (2007).